OPTICAL AND STRUCTURAL PROPERTIES OF Er-DOPED GaN/InGaN MATERIALS AND DEVICES SYNTHESIZED BY METAL ORGANIC CHEMICAL VAPOR DEPOSITION

by

CRISTOFER RUSSELL UGOLINI

B.A., Bethany College, 2003

AN ABSTRACT OF A DISSERTATION

submitted in partial fulfillment of the requirements for the degree

DOCTOR OF PHILOSOPHY

Department of Physics
College of Arts and Sciences

KANSAS STATE UNIVERSITY
Manhattan, Kansas

2008

Abstract

The optical and structural properties of Er-doped GaN/InGaN materials and devices synthesized by metal organic chemical vapor deposition (MOCVD) were investigated. Er-doped GaN via MOCVD emits a strong photoluminescence (PL) emission at 1.54 μm using both above and below-bandgap excitation. In contrast to other growth methods, MOCVD-grown Er-doped GaN epilayers exhibit virtually no visible emission lines. A small thermal quenching effect, with only a 20% decrease in the integrated intensity of the 1.54 μm PL emission, occurred between 10 and 300 K. The dominant bandedge emission of Er-doped GaN at 3.23 eV was observed at room temperature, which is red-shifted by 0.19 eV from the bandedge emission of undoped GaN. An activation energy of 191 meV was obtained from the thermal quenching of the integrated intensity of the 1.54 μm emission line.

It was observed that surface morphology and 1.54 μm PL emission intensity was strongly dependent upon the Er/NH_3 flow rate ratio and the growth temperature. XRD measurements showed that the crystalline ordering of the (002) plane was relatively unperturbed for the changing growth environment. Least-squares fitting of 1.54 μm PL measurements from Er-doped GaN of different growth temperatures was utilized to determine a formation energy of 1.82 ± 0.1 eV for the Er-emitting centers.

The crystalline quality and surface morphology of Er-doped $In_{0.05}Ga_{0.95}N$ was nearly identical to that of Er-doped GaN, yet the PL intensity of the 1.54 μm emission from Er-doped $In_{0.05}Ga_{0.95}N$ was 16 x smaller than that of Er-doped GaN. The drop in PL intensity is attributed to the much lower growth temperature in conjunction with the high formation energy of the Er-emitting centers. Er-doped InGaN grown at fixed growth temperature with different growth pressures, NH_3 flow rates, and Ga flow rates was also investigated, and showed that increased In fractions also resulted in a smaller 1.54 μm PL intensity.

Er-doped InGaN p-i-n diodes were synthesized and tested. The electroluminescence (EL) spectra under forward bias shows strong Er based emission in the infrared and visible region. The different emission lines from EL spectra in contrast to PL spectra implies different excitation methods for the Er based emission in the p-i-n diode than in the PL excited epilayer.

OPTICAL AND STRUCTURAL PROPERTIES OF Er-DOPED GaN/InGaN MATERIALS AND DEVICES SYNTHESIZED BY METAL ORGANIC CHEMICAL VAPOR DEPOSITION

by

CRISTOFER RUSSELL UGOLINI

B.A., Bethany College, 2003

A DISSERTATION

submitted in partial fulfillment of the requirements for the degree

DOCTOR OF PHILOSOPHY

Department of Physics
College of Arts and Sciences

KANSAS STATE UNIVERSITY
Manhattan, Kansas

2008

Approved by:

Major Professor
Hongxing Jiang

Copyright

Abstract

The optical and structural properties of Er-doped GaN/InGaN materials and devices synthesized by metal organic chemical vapor deposition (MOCVD) were investigated. Er-doped GaN via MOCVD emits a strong photoluminescence (PL) emission at 1.54 μm using both above and below-bandgap excitation. In contrast to other growth methods, MOCVD-grown Er-doped GaN epilayers exhibit virtually no visible emission lines. A small thermal quenching effect, with only a 20% decrease in the integrated intensity of the 1.54 μm PL emission, occurred between 10 and 300 K. The dominant bandedge emission of Er-doped GaN at 3.23 eV was observed at room temperature, which is red-shifted by 0.19 eV from the bandedge emission of undoped GaN. An activation energy of 191 meV was obtained from the thermal quenching of the integrated intensity of the 1.54 μm emission line.

It was observed that surface morphology and 1.54 μm PL emission intensity was strongly dependent upon the Er/NH_3 flow rate ratio and the growth temperature. XRD measurements showed that the crystalline ordering of the (002) plane was relatively unperturbed for the changing growth environment. Least-squares fitting of 1.54 μm PL measurements from Er-doped GaN of different growth temperatures was utilized to determine a formation energy of 1.82 ± 0.1 eV for the Er-emitting centers.

The crystalline quality and surface morphology of Er-doped $In_{0.05}Ga_{0.95}N$ was nearly identical to that of Er-doped GaN, yet the PL intensity of the 1.54 μm emission from Er-doped $In_{0.05}Ga_{0.95}N$ was 16 x smaller than that of Er-doped GaN. The drop in PL intensity is attributed to the much lower growth temperature in conjunction with the high formation energy of the Er-emitting centers. Er-doped InGaN grown at fixed growth temperature with different growth pressures, NH_3 flow rates, and Ga flow rates was also investigated, and showed that increased In fractions also resulted in a smaller 1.54 μm PL intensity.

Er-doped InGaN p-i-n diodes were synthesized and tested. The electroluminescence (EL) spectra under forward bias shows strong Er based emission for the infrared and visible region. The different emission lines from EL spectra in contrast to PL spectra implies different excitation methods for the Er based emission in the p-i-n diode than in the PL excited epilayer..

Table of Contents

List of Figures

Acknowledgements

My degree would not be possible without the constant hand of God and his son Jesus carrying me along the way. All glory and honor to them for this accomplishment.

A special thank you to my parents for raising me to be the man I am today. Their lives are proof that "in all things, God works for the good of those who love him and are called according to his purpose", Romans 8:28.

I would like to acknowledge Dr. Brian Adrian. A man who showed great patience and helped a young, immature man with a passion for science learn to think like a physicist.

I would like to thank my advisors Dr. Hongxing Jiang and Dr. Jingyu Lin for allowing me the opportunity to work in such an extravagant and competitive laboratory, and to pursue the area of physics I find most fascinating.

Thank you to Chris Sorensen for teaching me to think like a Ph. D.

A special thanks goes to Dr. Li Jing for teaching me everything a person could learn about III-nitride materials growth and characterization.

To Missy and TJ, for providing me with support and love throughout my life.

To Ryan Moore, for always being the "best man" in my life.

To Spencer Stelljes, Nathan Keith, Kevin Knabe, Andrew Jones, Karl Tillman, Shawn Moore, Chris Moore, Ben Deaver, Paxton Lemoine, and Matt Berg, for providing essential support and friendship.

To my church family, thank you for your prayers and support.

I would like to acknowledge my past and present colleagues, Dr. Zhaoyang Fan, Professor Jin, Dr. Kyoung-Kim, Dr. Ki-bum Nam, Dr. Jagat Shakya, Dr. Mim Nakarmi, Dr. Neeraj Nepal, Dr. Talal Al Tahtamouni, Neelam Khan, Bed Pantha, Rajendra Dahal, Ashok Sedhain, and Weiping Zhao for their efforts, conversation, and influence. Thank you to my committee member as well for their help in making my passion a reality.

And lastly, and most importantly, to my wife Crystal, who is the reason I have made it this far today. Thank you for your patience, sacrifice, support, and for showing me the true measure of God's love.

Dedication

To God who gave me the strength to persevere and the intelligence to understand, to my parents for their love and guidance, to my family and friends for their continual support, and to my wife for her unwavering love, commitment, support, and sacrifice.

CHAPTER 1 - Introduction and Motivation

1.1 Semiconductor evolution

Semiconductor materials and their subsequent devices are a mainstay of our modern world. Since the discovery of the p-n junction in 1940 by Russell Ohl, many semiconductor materials have been fabricated and analyzed in hopes of applying these semiconductors to the creation of new device technologies [1,2]. Over the years, the academic and commercial semiconductor industry has seen the development of three distinctly different generations of semiconductor materials and devices. The first generation belongs to single-element semiconductors like Si and Ge, with applications in IR detection systems, modern-day transistors, and integrated logic circuits [2]. The second generation saw the dawn of certain compound semiconductors like InP and GaAs. With these materials came the creation of efficient light emitting diodes (LEDs) and laser diodes (LDs) operating in the red to IR region, and other related IR devices [2]. But, in the last two decades, due to the dramatic advancement of materials growth method purity and precision, the third generation of semiconductors like GaN, SiC, and ZnO has emerged. Of these semiconductors, GaN and its alloy with In and Al are of particular interest for many applications.

III-nitride materials (AlN, GaN, and InN) are direct bandgap semiconductors that have a bandgap energy of 0.7 eV for InN, 3.42 eV for GaN, and 6.2 eV for AlN. Depicted in Fig. 1.1 is a comparison of the bandgap energy of the III-nitride spectrum as a function of in-plane lattice constant in comparison to other compound semiconductor materials [3,4]. With such a large bandgap energy range and direct bandgap nature, these materials are ideal for optoelectronic devices operating from the infrared (IR) to deep ultra-violet (DUV) spectrum through tertiary and quaternary alloying. III-nitrides also have a very large bonding energy, allowing them to survive in harsher environments than their II-VI counterparts [5]. III-nitrides have a large thermal conductivity, allowing for efficient heat transfer between active devices and the heat sink employed when operating in high-current/high temperature regimes. Due to these properties and the ability to generate high quality n-type and p-type materials, realization of commercially ready blue/green/UV LEDs and LDs has been realized [6,7].

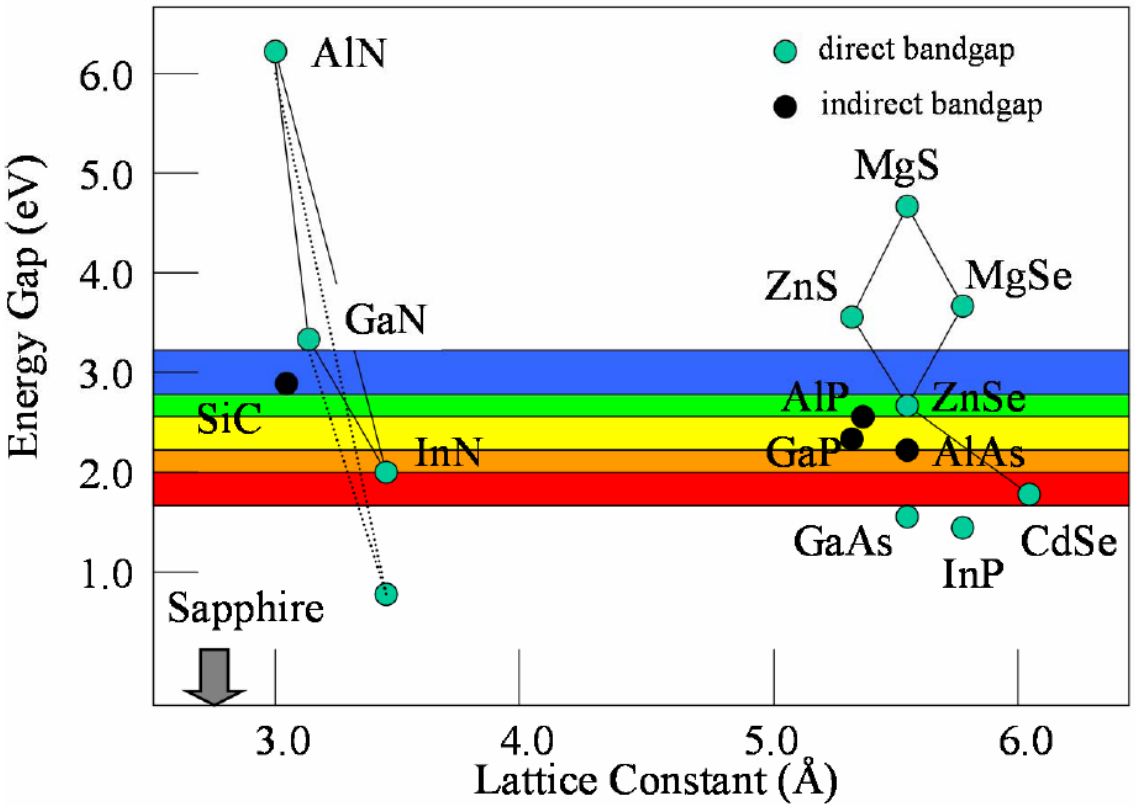

Figure 1-1 A comparison of the bandgap energy of III-nitrides and other compound semiconductors as a function of in-plane lattice constant [3]. The second bubble for InN is a result of new data showing that InN has a bandgap energy of 0.7 eV [4].

1.2 Brief History of III-N materials and devices

A review of the history of the development of GaN and its properties is essential in order to understand the complexity of the methods required for high quality GaN growth. In 1932, the first reported synthesis of GaN occurred by passing NH_3 over a hot GaN melt [8]. This method was used to create GaN needles and platelets which were then used characterize the optical and structural properties of the GaN system [9,10]. But, very few other reports on GaN materials occurred until after the 1970's due to the primitive materials growth methods available at that time. But, interest in GaN materials was renewed with the development of more sophisticated and pure epitaxial growth methods, and the availability of more appropriate growth substrates like sapphire. In 1969, the first GaN epilayer was grown on sapphire[11]. But, even then, GaN was far from being considered of high-quality since background electron concentrations ranging from 10^{18} to 10^{20} cm^{-3} were unavoidable. With inherent *n*-type conductivity, the achievement of *p*-type conductivity was not possible. Elements such as Mg, Be, Zn and Cd were incorporated into GaN in hopes of creating p-type conductivity, but with no success [12-16]. The first light-emitting diode (LED) based on GaN was produced by a Zn-doped metal-insulator-semiconductor structure, but suffered from a very low efficiency [17].

It appeared as if the full electrical and optical potential of GaN would never be realized due to the lacking growth techniques and inherent material limitations. Not until the modern growth techniques of molecular beam epitaxy (MBE) and metal-organic chemical vapor deposition (MOCVD) were developed was it that more progress took place for the GaN community. Through trial and error, appropriate low-temperature GaN or AlN buffer layer recipes between the epilayer and substrate were implemented, reducing the background electron levels to 10^{17} cm^{-3} or below at room temperature [18-21]. But, the ability to achieve p-type conductivity was still out of reach. In a twist of fate, the accidental discovery of post-growth annealing of Mg-doped GaN by electron-beam irradiation resulted in the first p-type conductivity in GaN [22].

Although the mechanism responsible for the sudden appearance of p-type conduction was not understood, this result marked the most important step for GaN's application to the commercial market. Nakamura et. al [23]. later showed that p-type conductivity from Mg-doped

GaN was only possible by annealing away the hydrogen atoms that passivated the Mg acceptors. Through the post-growth thermal annealing of Mg-doped GaN in a N_2 ambient, he was able to change the resistivity of the material from 10^6 to 2 Ω cm [23]. With the last piece in place, commercialization of GaN devices was possible. The first GaN based p-n junction LED was reported in 1994 [24], and to date, high brightness nitride-based LEDs are commonplace. Fig. 1-2 portrays some of the commercial LED devices available from flagship LED companies like CREE and LumiLEDs, and other commonplace technologies that have benefited from III-nitride commercialization.

Currently, GaN/InGaN based LEDs and LDs are based upon the electronic properties of n-type and p-type layers built into the device. When a quantum well (QW) layer (a layer with bandgap energy less than the surrounding material) is inserted between an n-type and p-type layer and a forward bias is applied, electrons from the n-layer and holes from the p-layer are injected into the QW. The electrons and holes then recombine, emitting photons of energy equal to that of the QW bandgap energy. Through the synthesis of high quality n-type and p-type GaN layers with QW's of In fractions between 5 and 25 %, researchers and commercial industries have been able to create highly efficient blue and green LEDs based upon the aforementioned semiconductor mechanism. However, GaN has emerged as a possible candidate for devices operating in the telecommunication spectrum without using this conventional mechanism. By implementing Er into GaN and exploiting the optical transitions of the 4f shell of Er, Er-doped GaN based devices may represent the next generation for the telecommunication industry [25]. In order to understand and verify Er-doped GaN's candidacy as a new age telecommunication platform, we must pause for a moment and understand the coveted optical properties of Er and the current state of telecommunication amplifiers.

1.3 Unique optical properties of Er

Er is the 12th element of the 14 lanthanides (a.k.a. rare-earth elements) that begins to fill electrons into the 4f shell. Due to the asymmetric nature of the 4f shell wavefunction and inhomogeneous nucleus screening, the 4f shell is concatenated and resides nearer to the nucleus than the filled 5s and 5p shells. The outer 5s and 5p shells of the rare-earth atom shield the inner 4f electrons from the surrounding environment, allowing the different angular momentum energy levels of the 4f shell to remain relatively unperturbed when placed into a solid host [26-28].

Figure 1-2 (Top) A portrait of several commercially-available LED devices based upon InGaN technology from flagship companies like CREE ™ and LUMILEDS ™. (Middle) Comparison of Blue-ray (GaN laser) technology with traditional DVD technology. (Bottom) Picture of a large-scale flexible HD display from Toshiba that utilizes III-nitride technology.

Starting with Lanthanum (Z = 57) and continuing until Ytterbium (Z = 70), the 4f shell of each rare-earth element has a different number of 4f electrons and therefore different quantum mechanical energy levels due to the variable **L • S** coupling. Experimentalists and theorists have verified this point, and shown the different energy levels of rare-earth elements [27,28,29].

Despite the potential application of different energy levels of different rare-earth elements, no element has been more widely investigated than Er. Fig. 1-3 shows the different energy levels of the 4f shell of Er using Russell-Saunders notation, and also shows the absorption spectra of modern silica-based fiber optics as a function of signal wavelength [27]. The radiative transition between the $^4I_{13/2}$ (first excited state) and $^4I_{15/2}$ (ground state) shown in Fig. 1-3 occurs at 1.5 μm, which also corresponds to the minima absorption of the c-band of the telecommunication spectrum. This overlap has led many researchers to synthesize optical amplifiers based upon the excitation of Er atoms [25].

Researchers have been successful in their attempts to make these amplifiers. Currently, commercially available Er-doped fiber amplifiers (EDFA) have allowed for drastic increases in telecommunication signal bandwidth and system robustness. The construction of modern day EDFA's consists of a fiber optic highly doped with Er (typically $10^{18} – 10^{19}$ cm^{-3}) in conjunction with a 1490 or 980 nm pumping laser. The 1490 or 980 nm laser creates population inversion of the Er atoms by resonant optical pumping of Er atoms into higher states. The higher states have a much longer lifetime than the $^4I_{13/2}$ allowing for significant inversion [29], and commercial EDFAs with gain values of 30 dB are common place [30].

1.4 Current status of telecommunication-wavelength optical amplifiers

With the need for ever increasing telecommunication bandwidth and system integration, new devices will be needed due to the limitations of current optical amplifier technology. Modern telecommunication communication systems use wavelength division multiplexers (WDMs) in order to take full advantage of the wide bandwidth of modern fiber optic cables. Some such devices employed for these optical networks include WDM optical demultiplexers, wavelength routers, and optical amplifiers. In order to accommodate these smaller, denser, and more integratable systems, advanced materials for small-scale application must be synthesized. As one such example, chip-scale optical amplifiers made of highly efficient materials needs to be realized. In its current state, the two technologies employed for

Energy spectrum of the Er^{3+} 4f electrons

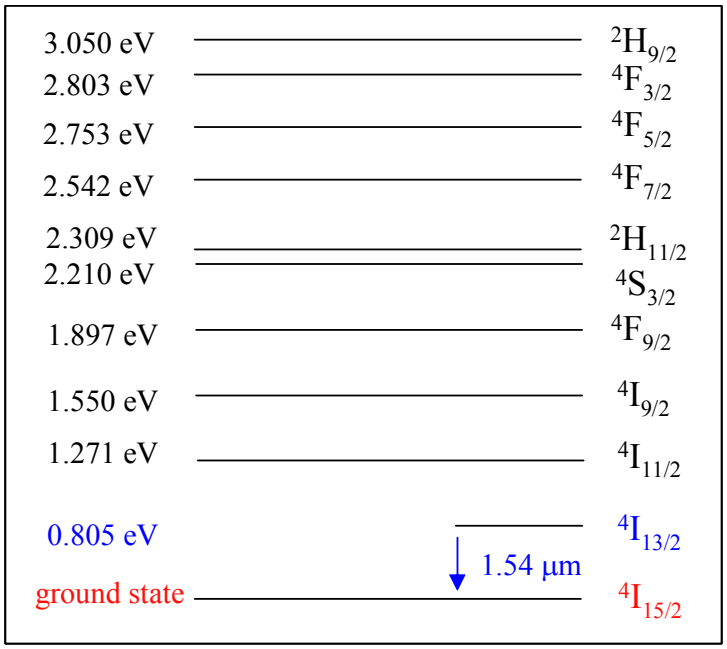

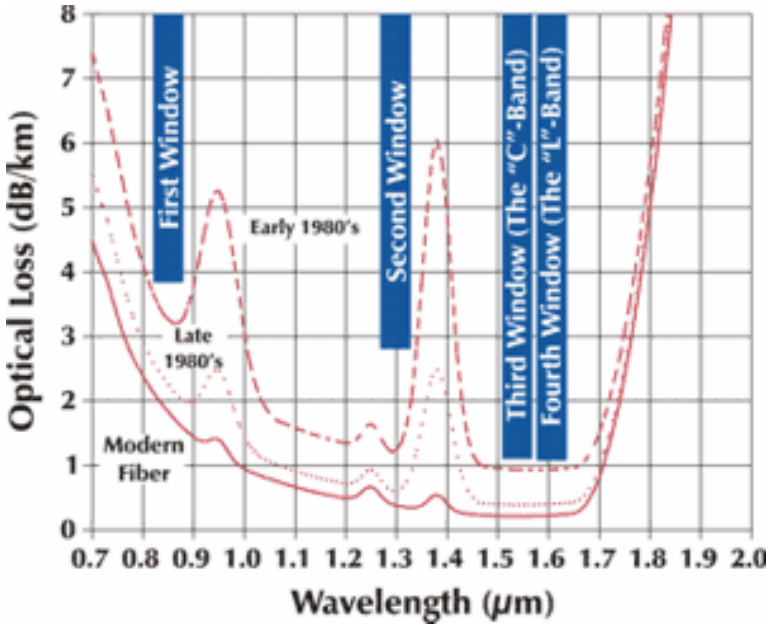

Figure 1-3 (Top left) Energy spectra of the 4f shell of Er. The numbers on the left indicate the difference in energy relative to the ground state, and the numbers on the right identify the different states in Russell-Saunders notation [28]. (Bottom right) Plot of the optical absorption of modern day fibers as a function of signal wavelength.

telecommunication amplification will not be sufficient for highly efficient, chip-scale application. With a typical fiber optic size of several meters long, the optically pumped EDFA cannot be directly integrated with other functional photonic devices of chip-scale. EDFA's also require elaborate and expensive pumping systems which economically limits their application to long-haul systems only. The other competing amplifier technology utilizes semiconductor materials for signal amplification. Semiconductor optical amplifiers (SOAs) are equivalent to fabre-perot laser cavities without the cavity mirrors required for lasing capabilities [31]. Although SOAs are available in chip-scale dimensions and utilize a current-based excitation method, the carrier recombination lifetime responsible for the signal gain is so fast that signal induced crosstalk occurs when implementing these devices with WDM technology. Fig. 1-4 portrays the advantages and disadvantages of the current device platforms utilized for telecommunication signal amplification. Thus, it is clear that new materials will be needed to remedy the limitations of the current state of optical amplifiers.

Implementing a sufficiently high concentration of Er into a semiconductor host and processing the material on a small-scale may be one such solution. In a device based on an Er-doped semiconductor, the amplification would come from the dynamically desired intra-4f Er transition, whereas the excitation method would be current-injection and the device size would benefit from the small-scale processing techniques mastered by the semiconductor industry. In order to determine which semiconductor material would be ideal for Er doping, several qualities of the host need to be prevalent in order for the host to be efficient. i) The host must allow for a large concentration (typically greater than 10^{20} cm^{-3}) without a significant perturbation to the optical, electrical, and mechanical host properties. ii) The method of Er atom excitation applied by the host semiconductor must be efficient in order to achieve population inversion at a reasonable energy expenditure.

1.5 Er-doped semiconductors

Although the wavelength of emission of the 4f shell of rare-earth elements is not affected by the solid host, the transition probability (i.e. emission intensity) is affected by the neighboring environment. Looking at the quantum mechanical theory, intra-4*f* transitions are parity forbidden by the Laporte selection rule. However, incorporating rare-earth (RE) elements into a solid with an appropriate crystal field induces a small perturbation to the 4f levels and relaxes the

Erbium Doped Fiber Amplifiers (EDFA's)

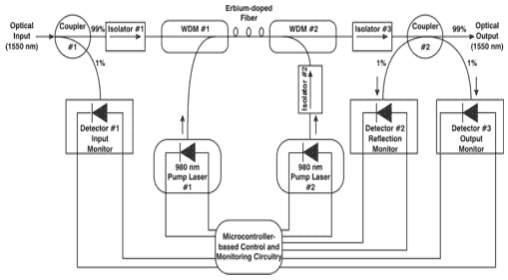

Upside	Drawback
1. High Gains - bandedge emission 2. Small scale - semiconductor scale	1. large signal distortion when used in WDM systems - fast carrier lifetime 2. high-coupling loss - large index of refraction

Semiconductor Optical Amplifiers (SOA's)

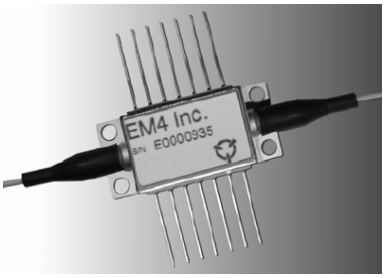

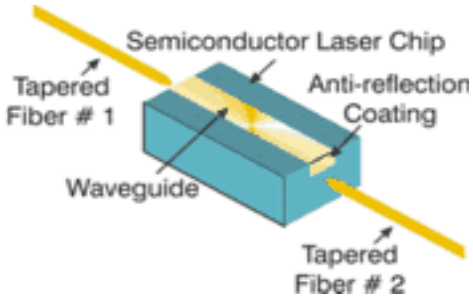

Upside	Drawback
1. High Gains - 4f shell emission 2. No signal distortion in WDM systems - slow lifetime of Er shell	1. Long Er doped fibers - low Er conc. and effic. 2. Complex laser pumps - high power required 3. Pictured EDFA is 12 cm x 20 cm x 2.5 cm

Figure 1-4 A comparison of the advantages and disadvantages for the current telecommunication amplifier platforms [30-32].

selection rule by admixing states of opposite parity. RE ions incorporated into a partially ionic solid occupying the cation site are exposed to one such uneven ligand crystal field that applies the necessary perturbation to partially relax the selection rule [33]. But, the intra-4f transitions are still not fully allowed, resulting in the experimentally observed excited state lifetimes on the order of ms [29]. With the C_{3v} symmetry of GaN and the fact that it has been shown that a majority of Er ions occupy the Ga sublattice in Er-doped GaN, the neighboring environment of GaN may be optimum for producing a large number of Er-emitting centers [34].

It has also been empirically determined that Er emission from semiconductors of smaller bandgaps has a low efficiency at room temperature due to a strong thermal quenching effect [35]. Fig. 1-5 is a plot of photoluminescence (PL) intensity of the 1.54 μm emission from different semiconductor hosts as a function of temperature. Clearly, semiconductors with smaller bandgap energies suffer from a dramatic thermal quenching of the Er-based PL emission. Although an exact understanding of this thermal quenching mechanism is not completely understood, the empirical work by Favennec et al. [35] has directed researchers to use wide bandgap semiconductors (WBGS) as hosts for Er. Due to this experimental determination, GaN is yet again an attractive host for Er based amplifiers since its bandgap is 3.42 eV.

This result did not deter many researchers from investigating semiconductors like Si, GaAs, and InP as possible hosts for Er based devices [35-45]. Fig. 1-6 is an example of some of the electroluminescence (EL) devices operating in the IR region for semiconductor materials like GaAs and InP utilizing different synthesis methods like metal organic chemical vapor deposition (MOCVD) or ion-implantation. For each device, the 1.5 μm emission from the Er atom is present, yet to date, such devices based on these host materials have a very low quantum efficiency. In addition to the thermal quenching effect found in these smaller bandgap materials, the method of material synthesis also affects the material quality. Methods such as ion-implantation are damaging to the material quality, thus resulting in a less efficient Er emission. Method of materials growth also determines the crystalline structure and Er concentration, making the choice of materials synthesis as important as the material host itself.

1.6 Current limitations of Er-doped GaN

To date, successful doping of Er into GaN has been accomplished by methods such as molecular beam epitaxy (MBE), ion implantation, metal organic molecular beam epitaxy

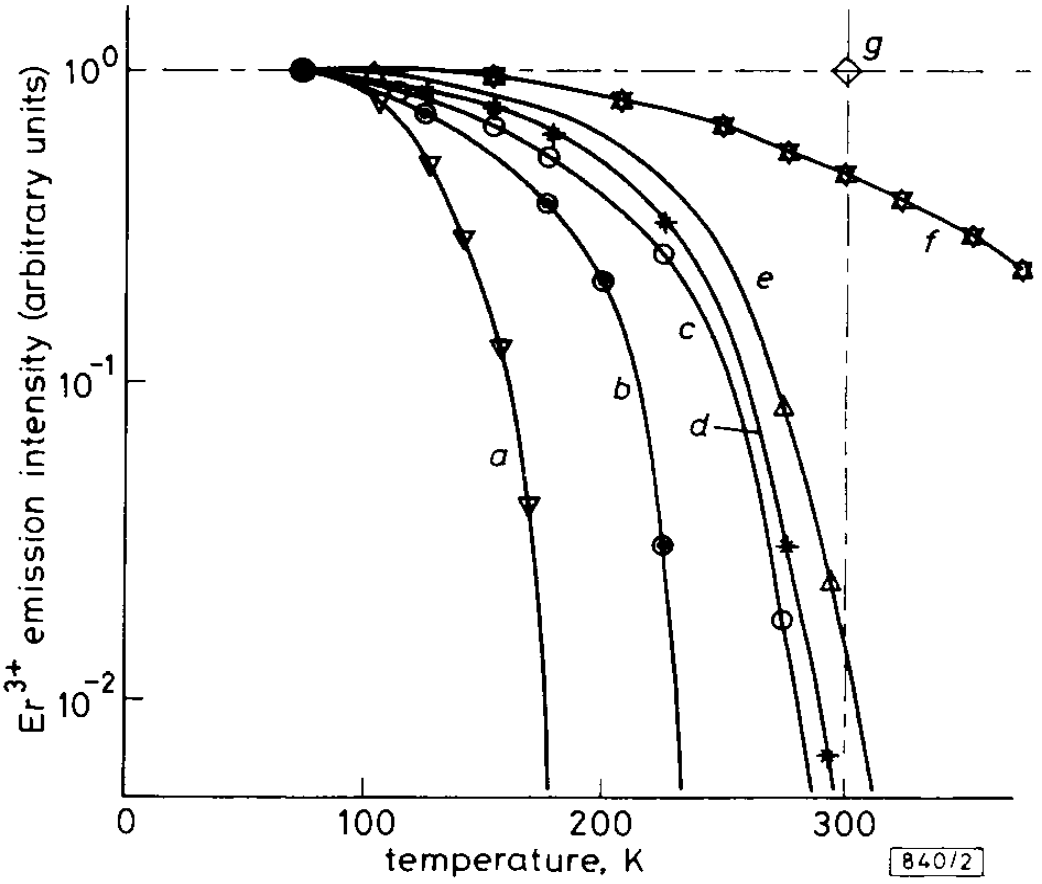

Fig. 2 *Er^{3+} emission intensity against host semiconductor temperature*

Materials are implanted with Er ions: $E = 330\,\text{keV}$, $\phi = 10^{13}$ Er^+ cm^{-2}. E_G values are given at room temperature

a $Ga_{0\cdot38}In_{0\cdot62}As_{0\cdot84}P_{0\cdot12}$ ($E_G = 0\cdot807\,\text{eV}$)
b Si ($E_G = 1\cdot12\,\text{eV}$)
c InP ($E_G = 1\cdot27\,\text{eV}$)
d GaAs ($E_G = 1\cdot43\,\text{eV}$)
e $Al_{0\cdot17}Ga_{0\cdot83}As$ ($E_G = 1\cdot67\,\text{eV}$)
f ZnTe ($E_G = 2\cdot26\,\text{eV}$)
g CdS ($E_G = 2\cdot42\,\text{eV}$)

Figure 1-5 Er based PL emission intensity as a function of ambient temperature for semiconductors of different bandgap energy [35].

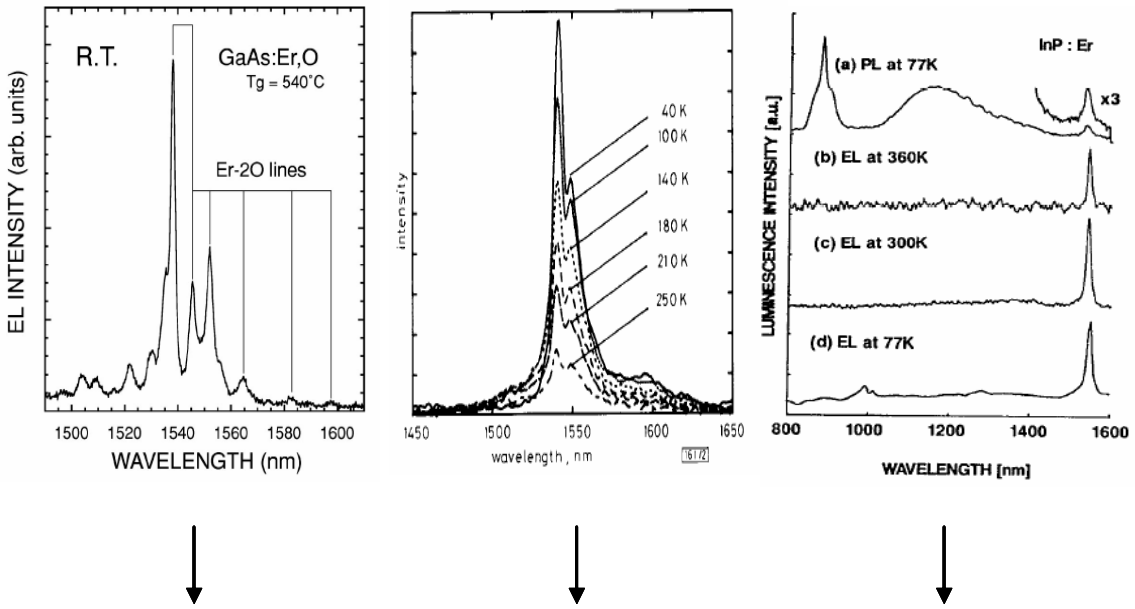

Semiconductor	Semiconductor	Semiconductor
GaAs	GaAs	InP
Synthesis Method	Synthesis Method	Synthesis Method
MOCVD	MOCVD	Ion Implantation
Device Structure	Device Structure	Device Structure
p-i-n diode	p-i-n diode	schottky diode

Figure 1-6 Comparison of Er based EL devices for different semiconductor materials and synthesis methods [38,41,45].

(MOMBE), and hydride vapor phase epitaxy (HVPE) [46-57]. GaN has proven to be an accomplished host, with reports of fabrication of light-emitting diodes (LEDs) operating in the visible and infrared region [47,52,55]. Fig. 1-7 shows the results of an Er-doped GaN Schottky diode synthesized by MBE for which a strong IR (1.54 μm transition) and VIS emission (537, 556 nm transition) is seen [52]. But, although devices based upon Er-doped GaN have been achieved, like their InP, Si, or GaAs counterpart, these devices still suffer from a low quantum efficiency at the IR wavelength, demanding a better understanding of the excitation and emission dynamics of the Er-doped GaN system. Our recent work was the first report of in-situ doping of Er into III-N materials and devices by the MOCVD method [58]. This at first seemed odd since the MOCVD synthesis method is the platform technology for commercial III-N devices [59]. However, we soon determined that the lack of reports of Er-doped GaN stems from the fact that most Er precursors acceptable for MOCVD applications suffer from a low vapor pressure or carry elements that are parasitic to III-nitride material. Thus, the goal of this work is to determine and implement solutions to make Er-doped GaN/InGaN materials and devices by MOCVD a reality, and to understand the optical and structural properties of the Er-doped GaN/InGaN materials and devices.

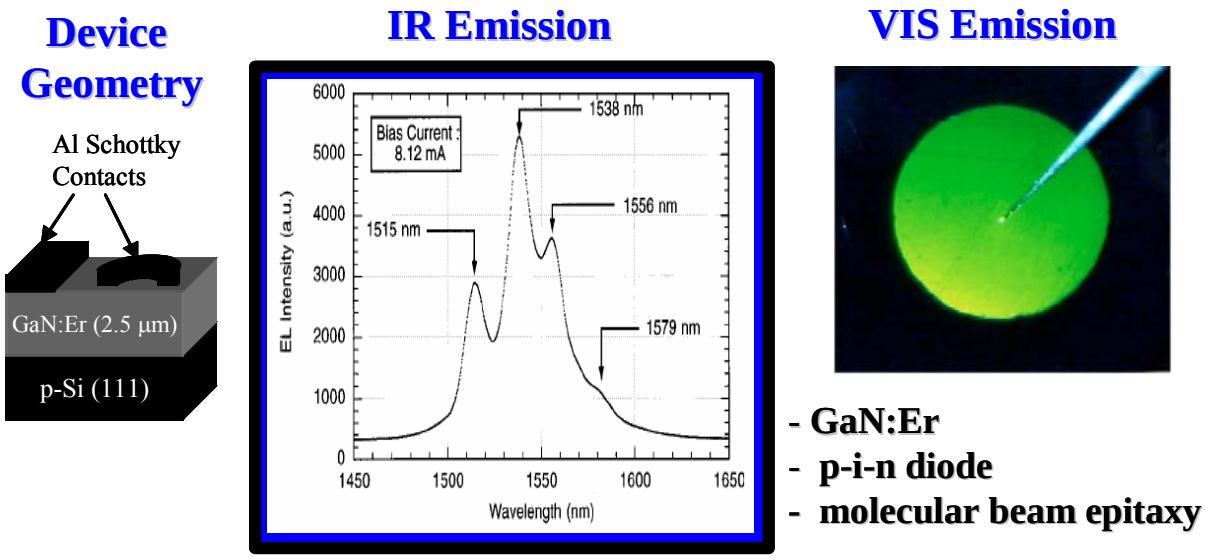

Figure 1-7 Device geometry and EL emission from an Er-doped GaN Schottky diode synthesized by MBE [52].

CHAPTER 2 - Experimental Methods

2.1 Metal Organic Chemical Vapor Deposition (MOCVD)

The Er-doped III-nitride materials and device structures that were made for this work were synthesized using a self-constructed metal organic chemical vapor deposition (MOCVD) system with specific adaptations that accommodate the Er precursor. Fig 2-1 is a picture of myself standing next to the MOCVD system (created by Dr. Jing Li) that was used to grow the Er-doped GaN/InGaN materials and devices used for this work.

MOCVD is a method for high purity materials growth in which a group-III metal organic precursor such as trimethylgallium (TMGA) or trimethylaluminum (TMAl) is transported by an inert gas (typically hydrogen or nitrogen) into a heated reaction zone containing a suitable growth substrate. In the same fashion, the group-V element (typically a hydride like NH_3) is separately transported to the heated reaction zone. The heated reaction zone is typically obtained through induction heating, and is monitored by a thermocouple and feedback system. In an ideal growth setting for MOCVD, the group-III source and the group-V source have negligible chemical interaction before encountering the reaction zone above the substrate. The two precursors pyrolize in the reaction zone due to the elevated temperatures, and the group-III atoms and group-V atoms would adsorb onto the surface, resulting in growth of the III-V epilayer. Fig. 2-2 is a pictoral representation of the chemical dynamics of the MOCVD process.

Materials grown by MOCVD are strongly affected by three aspects of the MOCVD method: i) group-III-V precursor and carrier gas selection, ii) substrate selection, and iii) MOCVD growth environment. In general, the group-III metalorganics used in the MOCVD method must not contain any elements that will drastically affect the material quality, and they must have a relatively simple chemical structure. In order to create reasonable growth rates and simplistic gas transport systems, the metalorganics chosen must also have a reasonable vapor pressure at or below room temperature. In the following sections, I discuss the nature of the volatility of the mainstay metalorganics used for III-nitride growth. The choice of the group-V precursor for MOCVD growth of III-nitride materials is also problematic. Typically, NH_3 is used as the group-V precursor because of its commercial purity and acceptable chemical

Figure 2-1 Picture of myself standing next to the home-built MOCVD machine created by Dr. Jing Li that was used for this work to synthesize Er-doped GaN/InGaN materials and devices.

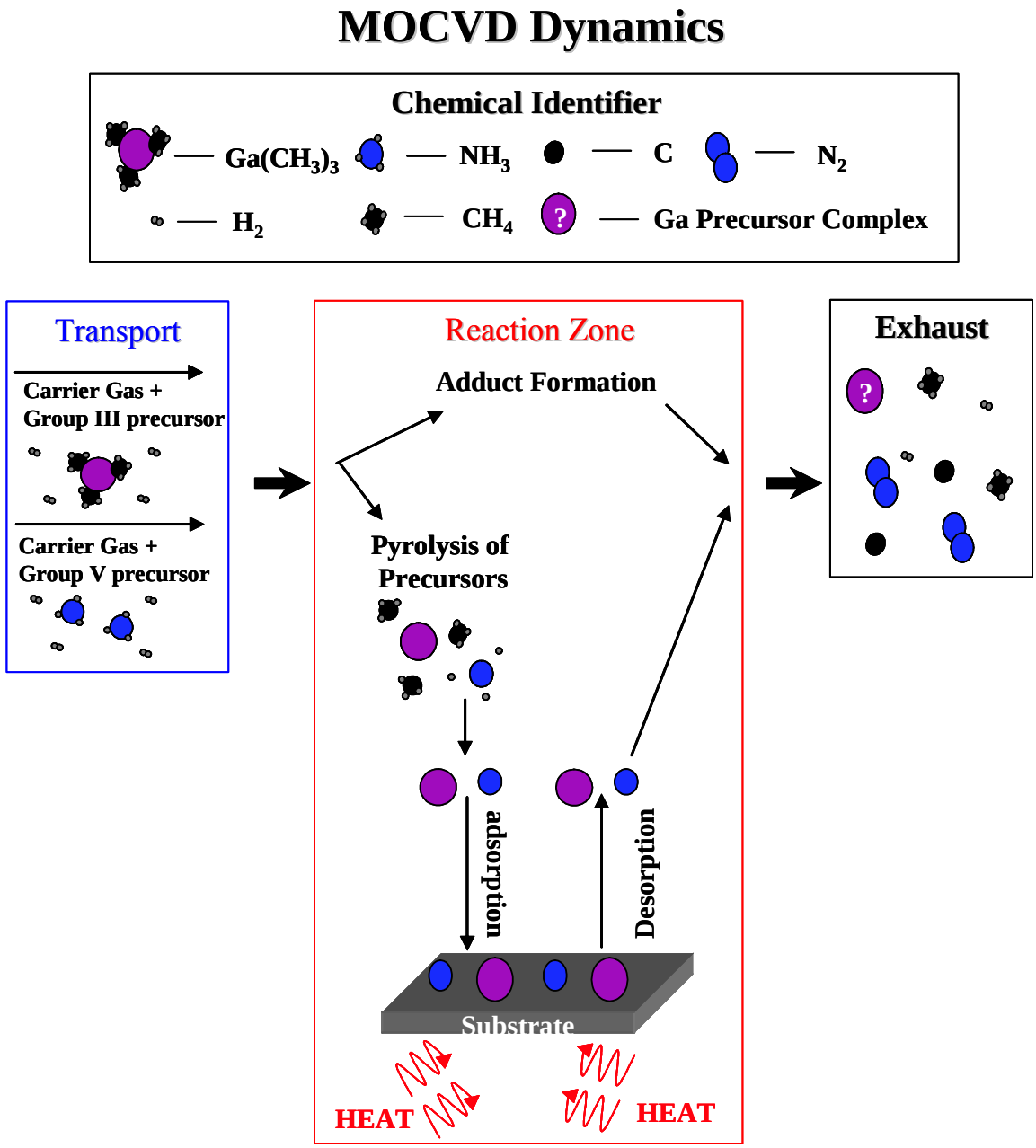

Figure 2-2 Pictoral representation of the chemical dynamics of the MOCVD process.

properties. However, NH_3 is corrosive to many materials, and hence careful selection of materials for the reactor chamber, susceptor, and substrate must be taken. NH_3 is also a very stable compound (little dissociation) at T_G typically used for III-nitride growth, thus requiring high V/III ratios.

Since MOCVD growth is not a free standing growth method, the origination of the growth must occur upon a crystalline substrate. Ideally, the substrate would have an identical crystal structure as that of the desired epilayer, would be of high crystalline quality, and could be purchased at a reasonable cost. Some companies have reported commercially available single crystal AlN and GaN substrates with a high degree of crystalline quality [60]. These substrates would be ideal since they could be tailored to match all material aspects of the MOCVD epilayer. But currently, the cost of these substrates currently prohibits them from everyday use. To date, the only commercially available substrates that are cost effective for MOCVD growth of III-nitride materials are sapphire or SiC. These substrates are not without their issues as well. The lattice matching between sapphire and SiC causes growth defects that degrade the electrical and optical properties. The difference in thermal expansion coefficients between the substrate and epilayer also induces thermal strain during heat-up and cool down, producing epilayers with cracks and other associated defects. In order to reduce both effects, MOCVD engineers have had to fabricate III-nitride materials and devices with complex structures. Despite these issues though, both SiC and sapphire have been used to produce blue and green LEDs with an acceptable device efficiency for commercial applications.

The quality of the material is also strongly dependent upon the many growth parameters in an MOCVD environment such as growth pressure (P_G), growth temperature (T_g), V/III ratio, and the epilayer design. These parameters help to dictate the growth kinetics, crystalline ordering, and material composition. MOCVD growth can occur in two growth regimes: diffusion-controlled or kinetically controlled. Kinetically controlled growth occurs when the growth rate of the epilayer is limited by the surface kinetics (T_G), rather than the precursor flow rate of the group-III and group-V elements. This mode of growth is usually not desired because small variations in the growth temperature result in dramatically varied material uniformity and quality. The desired diffusion-controlled growth is obtained when the growth rate is determined by the precursor flow rate, and T_G is high enough to accommodate a more uniform surface and

material quality. More information and explanation of MOCVD growth dynamics can be found in reference [61].

The MOCVD system used in this work is divided into 3 main components, **i)** the gas storage and transport system, **ii)** adaptations required for Er doping, and **iii)** the growth chamber/exhaust system, and the computer control and monitoring system.

2.1.1 Gas Storage and Transport System

The high purity metalorganics used for this study were obtained from Epichem Inc. and Strem Chemical Inc. and stored in stainless steel bubblers. Trimethylgallium (TMGa) and trimethylindium (TMIn) were used for the Ga, In, and Al sources, respectively. Silane (SiH_4), obtained from BOC Edwards (20 ppm in 6 grades H_2), was used to supply Si as an n-type dopant, while, bicyclopentadienylmagnesium (Cp_2Mg), was obtained from Epichem and used to supply Mg as the p-type dopant. Tri-isopropylcyclopentadienylerbium (TRIPEr) was obtained from Strem Chemical Inc. and was used to supply Er. Blue Ammonia (99.99994%),obtained from Airgas Inc., was passed through an Aeronex purifier and used as the N source. Ultra-high purity grade Hydrogen (99.999%) was passed through a palladium and Aeronex purifier to be used as the transport gas. High-purity liquid nitrogen was passed through an Aeronex gas purifier to be used as an alternative transport gas. Admixtures of H_2 and N_2 for the self-constructed MOCVD were also possible.

All MO bubblers were placed in Polystat recirculating refrigeration units to maintain the sources at constant temperature (vapor pressure). Gas protocol stations were employed for all other gases to maintain gas pressure. Computer-controlled Swagelok BN and HB series pneumatic valves in conjunction with MKS mass flow controllers (MFC's) were employed to control precursor flow rate ratios and gas directions, while Swagelok VCR gasket seals were used to maintain a leak free system. Fig. 2-3 is a diagram of the valve and MFC configuration for the MOCVD system.

2.1.2 Adaptations required to MOCVD for Er incorporation

As detailed in the introduction to this work, MOCVD growth of Er-doped III-nitride materials has not been accomplished to date due to the lack of suitable Er precursors. MO precursors such as TMGa provide a vapor pressure of ~ 80 torrs at 3 C [62]. Using conventional flow rates and system pressures employed in modern MOCVD systems, Ga flow rate rates on the

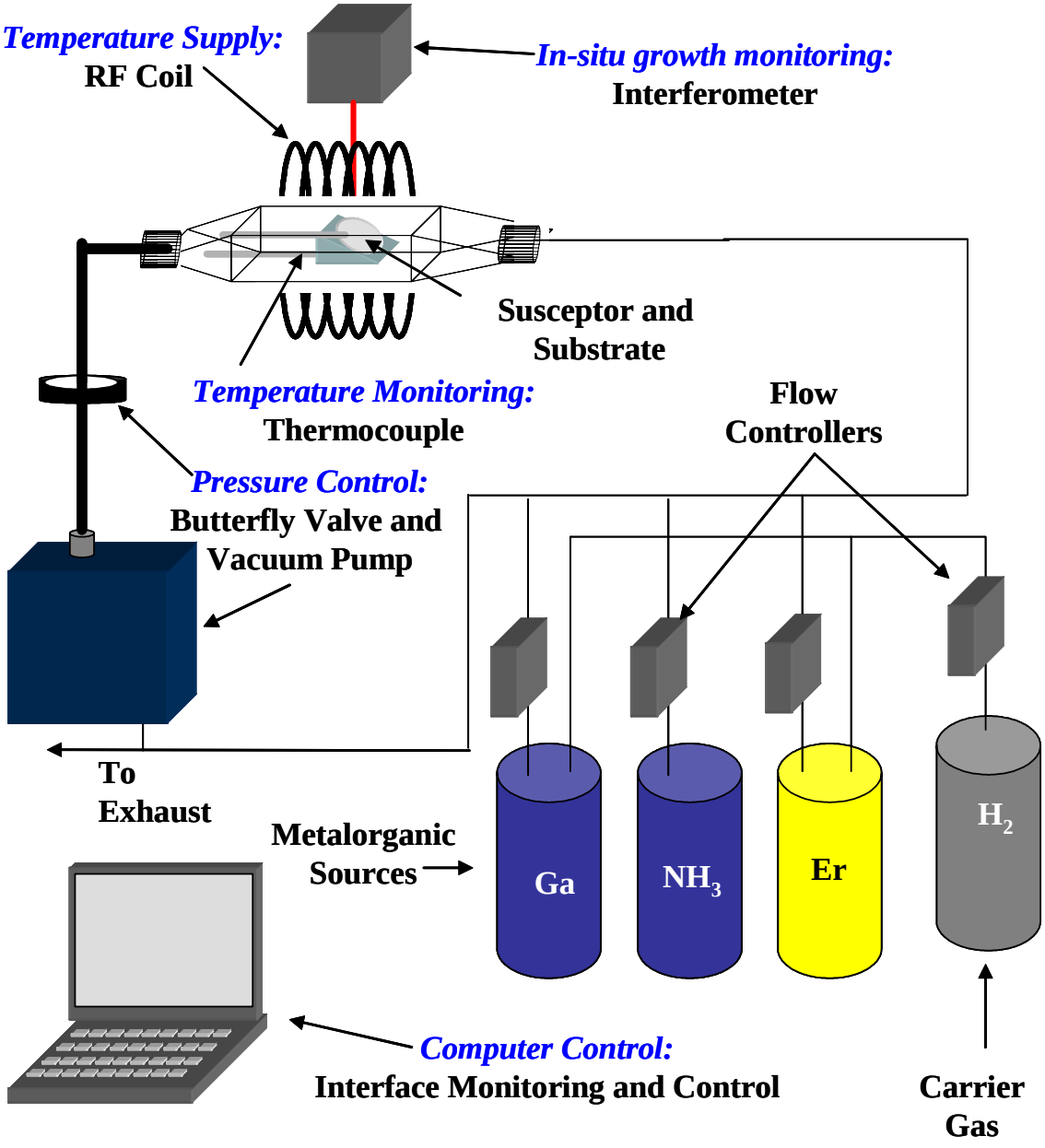

Figure 2-3 Schematic diagram showing the components utilized in the home-built MOCVD system used for this work.

order of μmol/min are easily achieved, allowing reasonable growth rates (1 – 3 μm/hr). Current MOCVD systems also use trimethylindium (TMIn) and trimethylaluminum (TMAl) for growth of AlGaN and InGaN alloys. In each case, the MO precursors have a reasonable vapor pressure at or below room temperature. Thus, each precursor can be utilized in inexpensive bubbler systems, without the need for heated doping lines that prevent precursor condensation. Besides their acceptable volatility at or below room temperatures, these precursors are also liquid at traditional bubbler temperatures, which allows for a more controllable doping process than a precursor in the solid phase. TMGa, TMAl, and TMIn have a relatively simple chemical structure, pyrolize at temperatures below typical GaN growth temperatures, and do not contain harshly parasitic elements to the III-N system. Due to these desirable properties, these sources are now widely available on the commercial level and have allowed III-N technology to mature drastically since its onset.

However, Er precursors have not had such commercial maturity, and the current state of Er sources is lackluster to say the least. Due to the large atomic mass of Er, most Er compounds have an extremely low vapor pressure at room temperature. This makes it virtually impossible to attain high Er doping concentrations (n_{Er}). Some attempts at increased volatility for the Er precursors have led chemical engineers to attach O or S chains to the Er compound. But, due to the parasitic effect of O and S on the optical and electrical properties of III-N materials, these precursors are not viable alternatives. Currently, the most applicable Er precursor for MOCVD growth of III-N materials as determined by the authors is trisopropylcyclopentadienylerbium (TRIPEr). TRIPEr melts around 65 C, and contains no O or S.

Although this precursor still has a relatively low vapor pressure at room temperature, the authors overcame this obstacle by immersing the source in a silicone oil bath at temperatures between 65 - 140 C. Higher temperatures were not possible due to the fact that heated silicone oil produces formaldehyde (carcinogenic) in the presence of air at temperatures exceeding 150 C. A majority of the Er doping for this work was done at a bubbler temperature of 100 C for which the vapor pressure of the source was 28 millitorrs [63]. Fig. 2-4 also shows the experimental vapor pressures of commonly used MOCVD precursors for GaN growth according to the Clausius-Clapeyron relation [62]. Since acceptable Mg concentration of 10^{20} cm^{-3} are achieved

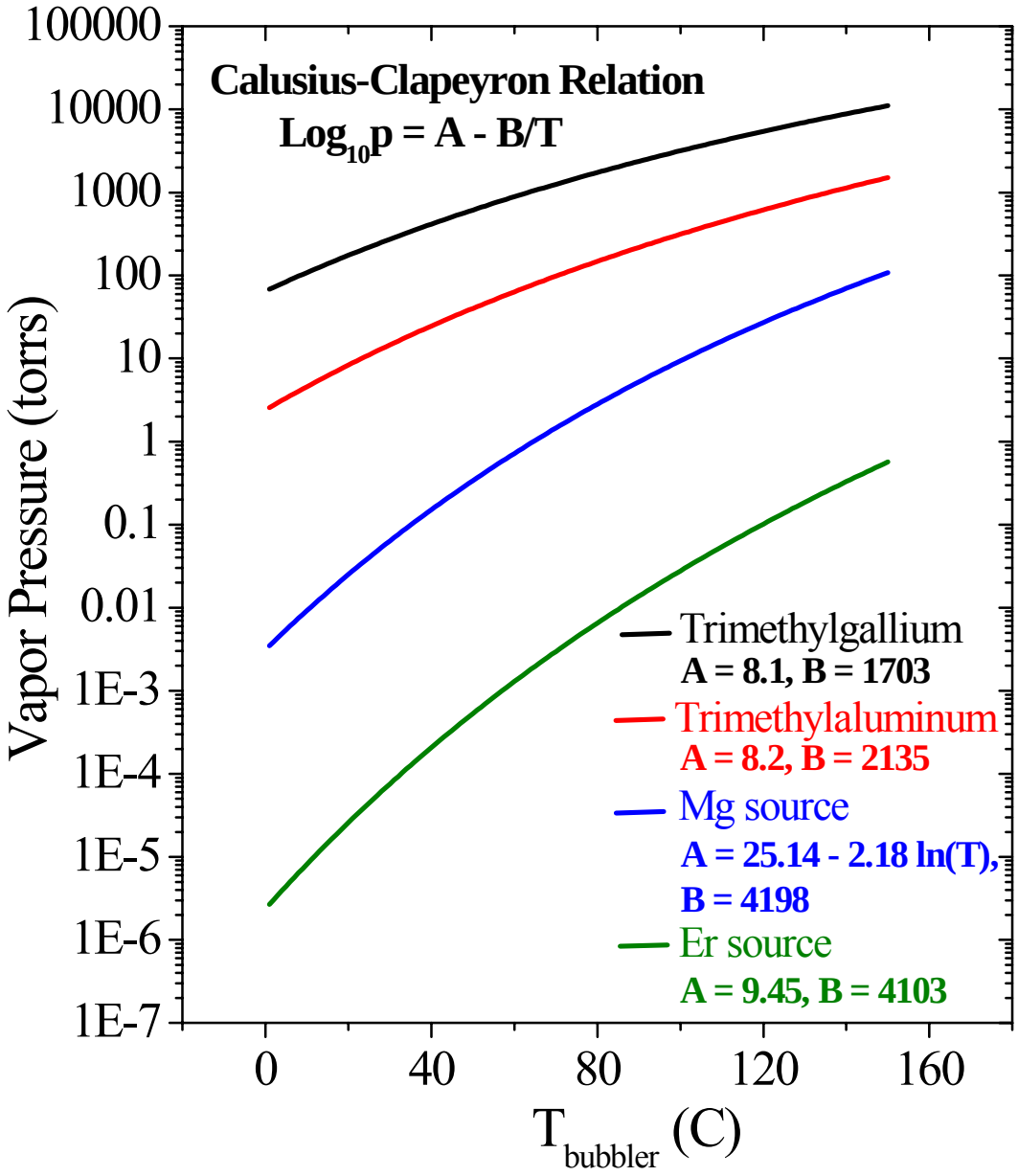

Figure 2-4 Vapor pressure plot for commonly used MO precursors. The equation used for the plot is the Clausius-Clapeyron relation: $\log_{10}(p) = A - B/T$. The values of A and B for trimethylgallium, trimethylaluminum, and Mg were provided by SAFC Hitech [62]. The A and B values for our Er source were taken from reference 63.

in p-type doping for Mg source vapor pressures of 30 millitorrs, it was reasoned that the Er vapor pressure at 100 C would be satisfactory for this work.

However, in order to prevent Er source condensation in the stainless steel doping line and valve system, the authors employed a specialized heating system to the valves and tubing. The system consists of several rubber, current-carrying, heating tapes acquired from Cole Parmer with adjustable heat output. The tapes were adhered to the doping line by a foil tape with a high temperature epoxy. Several thermistors and a controller from Cole Parmer were attached directly to the stainless steel tubing via a thermal bonding compound allowing for direct temperature measurement. During the growth of the Er-doped materials used for this work, the temperatures of the transport line were kept above bubbler temperature.

To allow for even higher doping concentrations, the pressure of the Er bubbler was adjusted compared to the other precursors. Fig. 2-5 is a schematic of the difference in transport lines employed for the TMGa, TMAl, Cp_2Mg, and TMIn source compared to the TRIPEr source. In moving the mass flow controller (MFC) to the opposite side of the source input, the pressure inside the bubbler is controlled by the reactor pressure. Thus, the ratio of the carrier gas to source gas is reduced, and the gas phase concentration of the source in the reaction zone is increased. The increase in gas phase concentration of the source gas allows for an increase in doping concentration capability. For the current work, low growth pressures between 10 – 50 torrs were used to reach the 10^{21} cm^{-3} values as outlined by the SIMS analysis depicted in the following sections.

2.1.3 Growth Chamber and Exhaust System

The growth chamber consists of a horizontal-flow quartz reactor (created by Technical Glass Products Inc.), a Boron Nitride coated graphite susceptor, a quartz positioning rod, and a quartz thermocouple tube. A Huttinger TIG 10/100 RF generator in combination with a 4-inch ,8-turn copper coil was used to provide heat during the epilayer growth. A type-R thermocouple (Platinum/Rhodium alloy) and a DP460 control unit created by OMEGA was used for temperature monitoring and control. For in-situ growth and surface morphology monitoring, a 670 nm Epieye reflectometer from ORS ltd. was employed. For a laser of fixed wavelength,

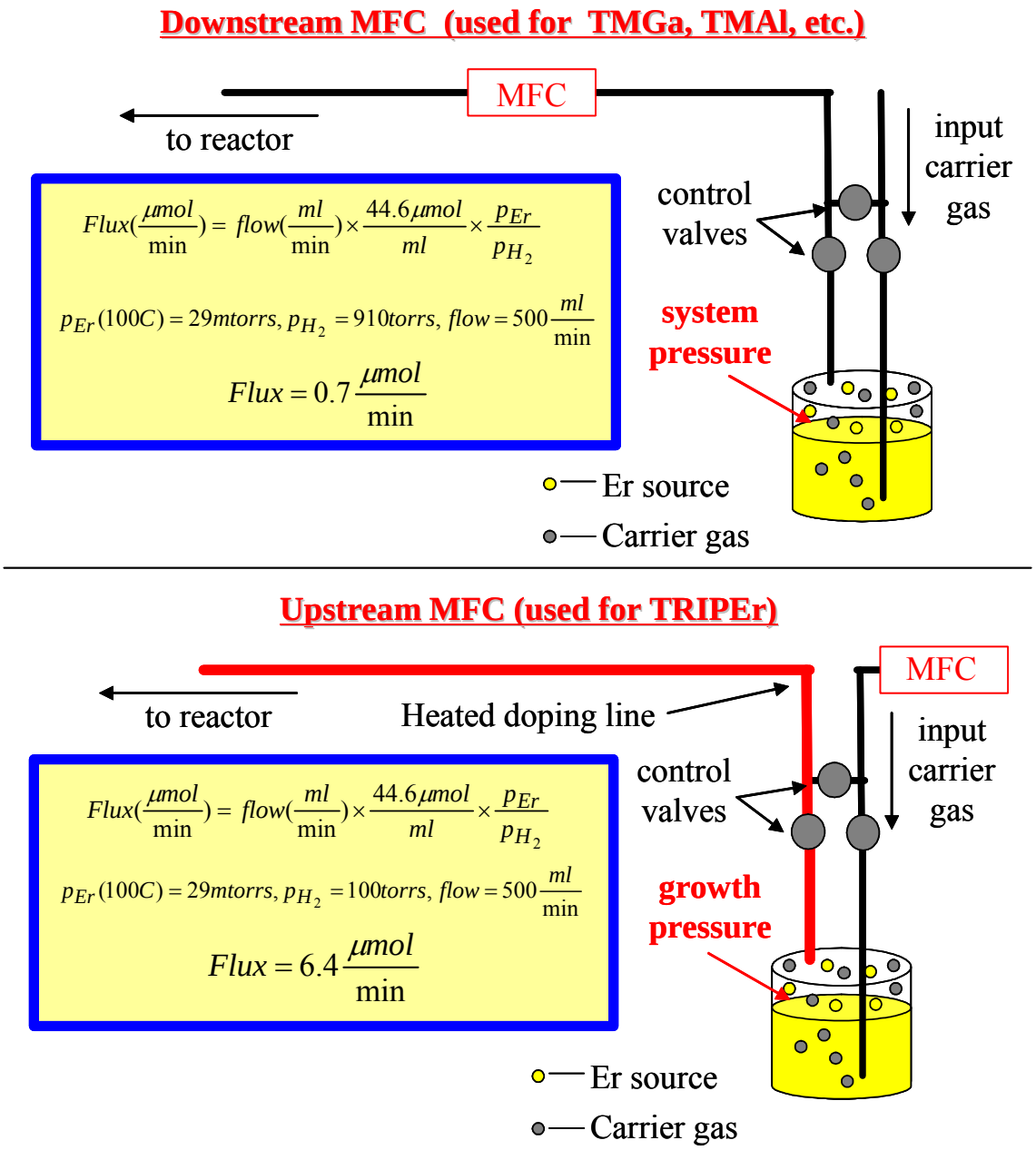

Figure 2-5 (Top) A schematic diagram of the gas handling system with the mass flow controller (MFC) placed downstream of the MO bubbler. (Bottom) A schematic diagram of the gas handling system with the mass flow controller (MFC) placed upstream of the MO bubbler. The equations in the shaded boxes show the values of the Er flow rate for each setup. Note, by placing the MFC upstream, the Er flow rate is increased dramatically.

polarity, and reflected angle incident upon a thin film, the thickness of the epilayer can be determined according to the equation (2-1):

$$n\lambda_m = d\sin\theta \tag{2-1}$$

where n is an integer, λ_m is the wavelength of the laser inside the material, and θ is the angle of reflection. As strain or surface roughness increases, the reflected intensity subsequently decreases. Thus, patterns with a decrease in signal intensity indicate a degradation in surface roughness or lattice strain. Fig. 2-6 is an interferometric pattern for the Er-doped GaN in which the brackets above indicate the different layers of the samples. Also depicted in Fig. 2-6 is the temperature profile (provided by RF induction heating) of Er-doped GaN as determined by the temperature control system.

Exhaust and pressure control of the MOCVD system was accomplished using a Pfeiffer DUO-350 mechanical pump, an MKS type-653 butterfly valve, an MKS type-722 pressure transducer, and an MKS type-651C control unit. The butterfly valve and transducer are placed downstream of the reactor, and are connected to the rotary pump. The transducer and throttle valve are also connected to the control unit which is in turn interfaced to the computer software. The user then inputs into the software the desired pressure. As the variable gas flows pass out of the reactor through the transducer, the transducer sends a reading to the control unit. The control unit then adjusts the throttle valve opening until the retuned signal from the transducer matches the user setpoint. For high vacuum pump downs prior to epilayer growth or for leak testing procedures, a single phase Pfeiffer rotary pump in conjunction with a Pfeiffer 400 Turbo unit was utilized. Under stable conditions, this configuration could produce 10^{-5} torr pressures.

A custom designed control chassis in conjunction with a Ni-DAQ board and a specialized Delphi software program was used to interface all aspects of the MOCVD system. The software program allows for direct input of varying growth parameters in a "recipe" format. The software also automates the growth process thus reducing operator error and time lag of manual input.

2.1 Photoluminescence (PL) Spectroscopy

PL spectroscopy is the premiere method for determining the optical properties of semiconductor materials in a non destructive and highly precise manner. The principle of PL spectroscopy is two fold: i) bombard the semiconductor material with sufficient optical energy (typically accomplished using laser systems) to create critical intrinsic transitions, and ii) collect

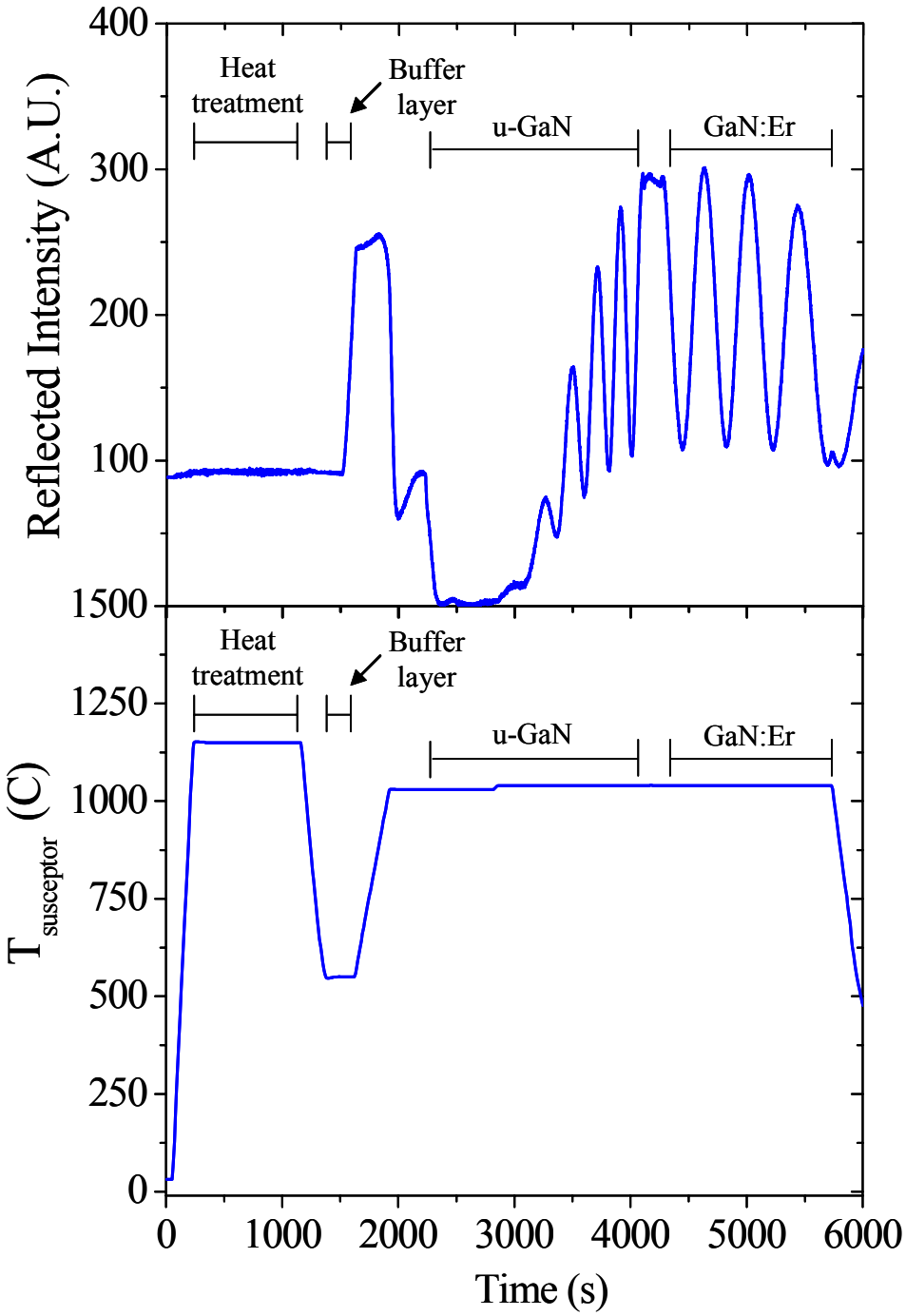

Figure 2-6 (Top) Reflectometer intensity versus growth time for Er-doped GaN. (Bottom) T_G versus growth time for Er-doped GaN as measured by the Type R thermocouple placed inside the graphite susceptor. The brackets identify the different layers in the material.

the semiconductor response emissions in order to determine material quality. For semiconductors, probing the bandgap emission and the subsequent emissions from with the bandgap region (i.e. impurities) are most important. Thus, PL systems must be designed in order to allow and detect optical wavelengths corresponding to the bandgap energies of the characterized materials. In the case of GaN (bandgap energy ~ 3.42 eV), laser systems and detectors in the ultra-violet (UV) range must be employed. For this work, a specialized time-resolved PL system consisting of a frequency-doubled and -tripled, 100 fs Ti:sapphire laser operating at an average power of 150 mW at 263 nm and 395 nm, and a repetition rate of 76 MHz was used. Fig. 2-7 is a pictoral representation of the PL system used in this work. IR (800 -1700 nm) PL detection was accomplished by an InGaAs detector, while visible (185 – 800 nm) PL detection was accomplished by a multi-channel plate photomultiplier tube, in conjunction with a 1.3 m monochromator. For PL decay lifetime measurements, either a single photon counting technique or a streak camera is used with precisions of 30 ps and 2 ps, respectively. A Janis cryostat system capable of producing temperatures of 10 – 800 K was utilized in order to probe the PL emission as a function of ambient temperature.

2.3 Electroluminescence (EL) Spectroscopy

Of equal importance to the characterization of the PL emission of semiconductor materials is the characterization of electroluminescence (EL). When a bias is applied to semiconductor materials, electron-hole recombination or impact excitation results in optical emission at wavelengths specific to the nature of the semiconductor material. In general, the dominant EL emission in semiconductor materials comes from the electron-hole pairs near the bandedge of the material, or from impurities/defects inherent in the material. In this work, the EL emission from Er-doped GaN devices was characterized using a custom-built EL probing station. Fig. 2-8 is a pictoral representation of the EL system used in this work. A Keithley 2400 series source meter was used to apply variable bias and current to the devices. An Olympus SZ61 Optical microscope was used for device positioning, and an Ocean Optics QP-600-mixed bifurcated fiber (190 – 1700 nm) was used to transfer the EL emission to VIS and IR detection systems. The IR spectrometer consisted of an InGaAs detector in conjunction with a 1.3 m monochromator, while the VIS spectrometer was an Ocean Optics PC2000 spectrometer. IR

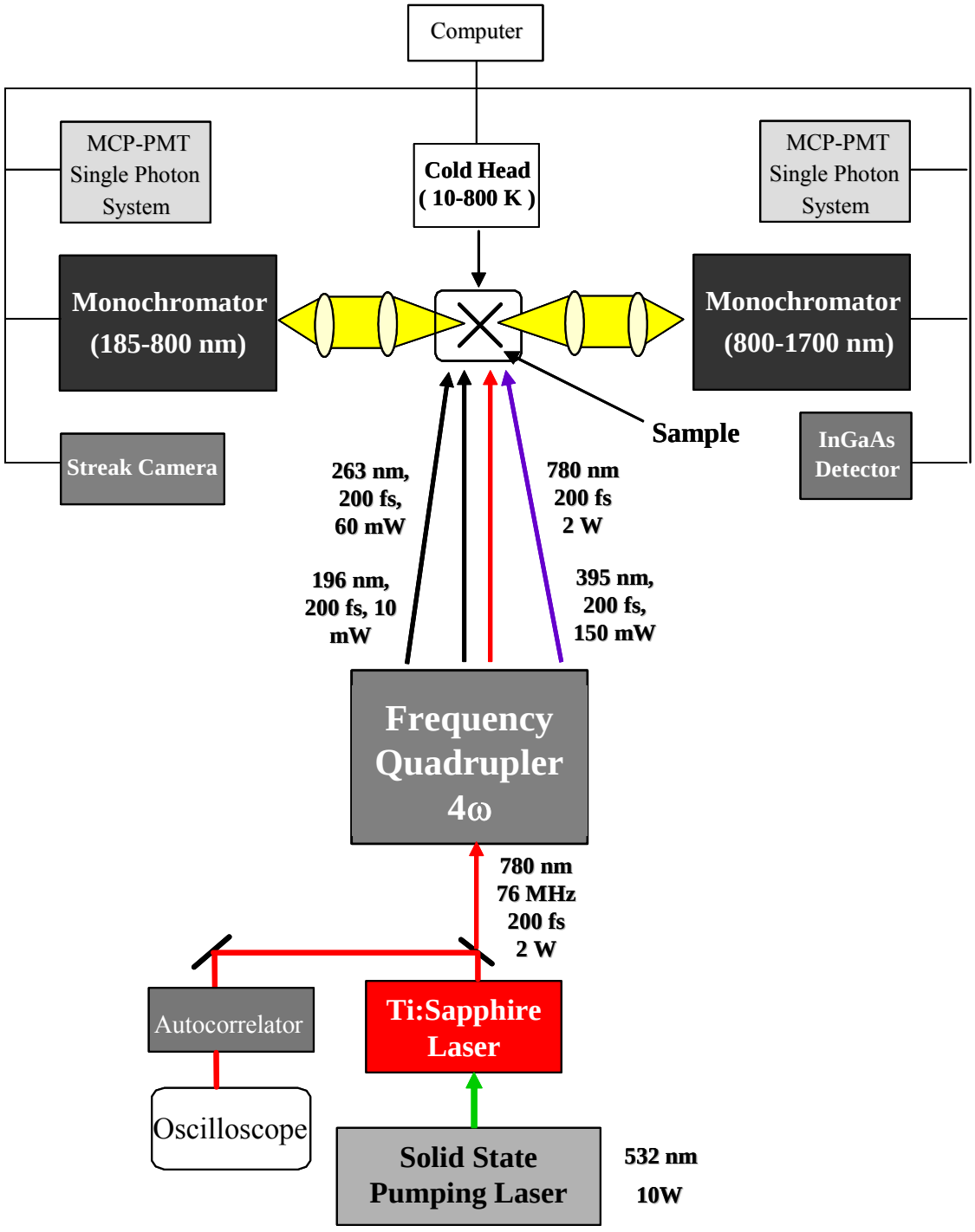

Figure 2-7 Pictoral representation of the different components of the PL spectroscopy system used for this work.

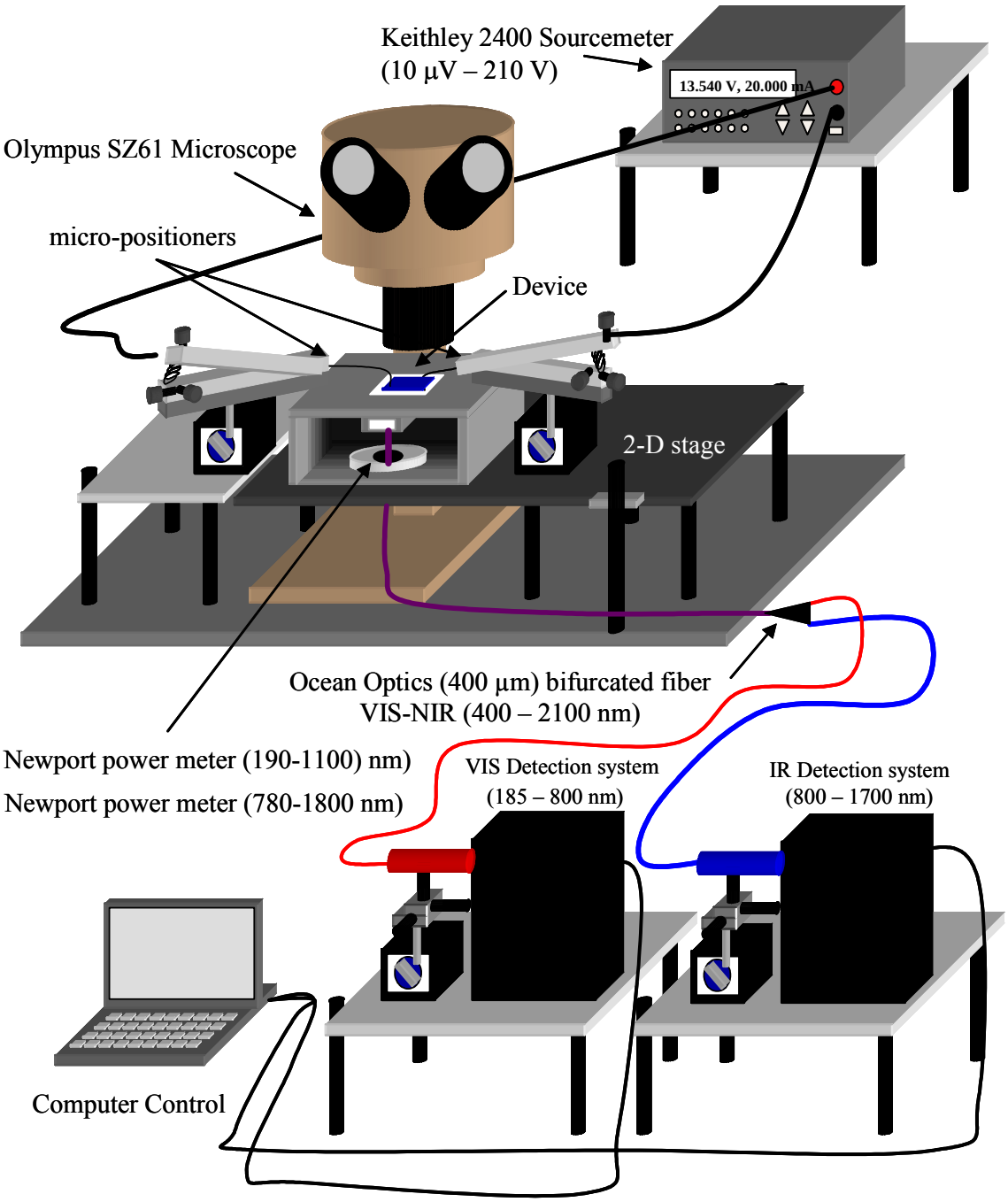

Figure 2-8 Pictoral representation of the different components of the EL spectroscopy system used for this work.

power measurements were made using a Newport 818-IR detector, while VIS power measurements were made using a Newport 818-UV-ST wand detector.

2.4 X-Ray Diffraction (XRD)

X-ray diffraction (XRD) is the main modern-day characterization tool utilized to study the crystalline properties of thin films. With this method, it is possible to determine structural information like layer orientation, lattice constants of certain planes, compressive/tensile lattice strain, and dislocation density. Through the detection of X-rays scattered constructively from different crystalline planes, the separation between planes can be determined from Bragg's equation (2-2):

$$n\lambda = 2d_{hkl}\sin(\theta) \tag{2-2}$$

for which λ is the X-ray wavelength, d_{hkl} is the lattice spacing for the given miller indice, and n is the order of reflection. For a hexagonal crystal such as the III-nitride system, d_{hkl} can be determined in terms of the a and c lattice constants according to equation (2-3):

$$d_{hkl} = \frac{1}{\sqrt{\frac{4}{3}\left(\frac{h^2 + hk + k^2}{a^2}\right) + \frac{l^2}{c^2}}} \tag{2-3}$$

for which hkl are the respective Miller indices, and a and c are lattice constants [64].

For this work, a Rigaku single crystal RINT2000V/PC XRD system was employed similar to the system pictured in Fig. 2-9. Fig. 2-9 also shows the crystalline structure of III-nitride materials, which is hexagonal wurtzite. The table in Fig. 2-9 gives the values of the lattice parameters for InN, GaN, and AlN. Kα1 = 0.154056 nm and Kα2 = 0.154439 nm X-rays produced from a copper filament were the X-rays produced by the system. For sample analysis Kα2 diffraction peaks were removed via a variable ratio software program.

For this work, the (002) plane of Er-doped GaN/InGaN materials was the main plane investigated to determine crystalline ordering and alloy composition. θ-2θ scans were employed to determine alloy composition of Er-doped InGaN. XRD rocking curves of the (002) plane were compared to determine crystalline ordering for both Er-doped GaN and Er-doped InGaN.

X-Ray Diffraction (XRD)

Rigaku – RINT 2000 ™

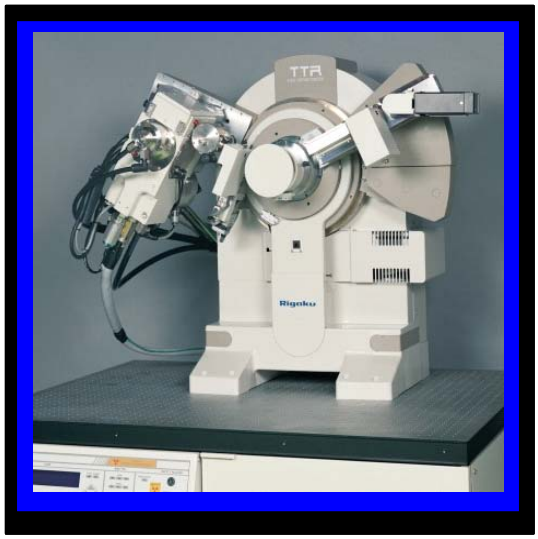

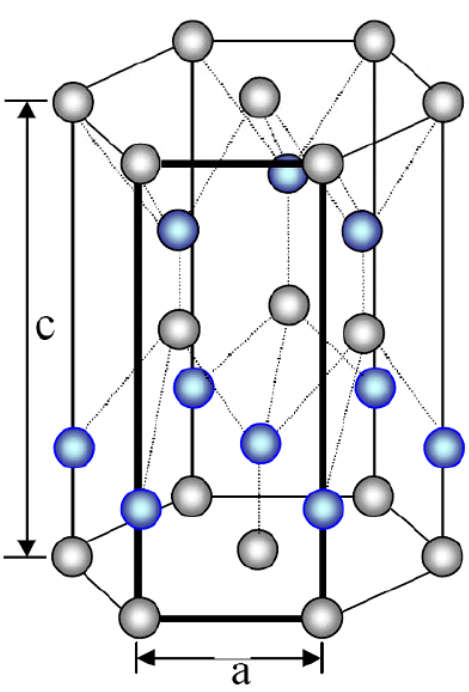

Al, Ga, In

N

	a(Å)	c(Å)
AlN	**3.112**	**4.982**
GaN	**3.189**	**5.186**
InN	**3.533**	**5.703**

Figure 2-9 (Top) Picture of XRD system similar to the one employed for this work. (Bottom) Crystalline structure of III-nitride materials, hexagonal wurtzite. The table lists the values of the a and c lattice parameters for all 3 materials [65].

2.5 Atomic Force and Optical Microscopy (AFM and OM)

The surface morphology of Er-doped GaN and InGaN was characterized by atomic force microscopy (AFM) and optical microscopy (OM). Atomic force microscopy is a high resolution surface profiling method well established in the semiconductor field. Through the focusing of a laser onto a thin cantilever containing a sharp tip, AFM systems map the deviations of thin film surfaces by detecting the deflection of the laser as it is scanned over the film surface. With the appropriate cantilever choice and feedback controls, AFM machines are capable of z-height resolution on the order of angstroms. Pictured in Fig. 2-10 is the Quesant Q-scope 250 AFM system (upper left) used in this work capable of operating in both non-contact and contact mode, and a z-height resolution of 0.5 nm.

Although OM microscopy does not have the resolution capability of AFM systems due to the diffraction limit of visible light, it is a much faster surface characterization method due to its relative simplicity. OM works on the principle of confocal imaging, and pictured in Fig. 2-10 (lower right) is a Nikon-600 that was used in this work. The OM system is capable of magnifications of 10 x (cm lengths) to 1000 x (10 μm lengths), and was utilized when surface mapping on much larger scales was needed.

Atomic Force Microscopy (AFM)

Quesant –Qscope 250 ™

Optical Microscopy (OM)

Nikon- 600 ™

Figure 2-10 (Upper left) Picture of Q-scope 250 AFM system used for this work. (Lower Right) Picture of Nikon OM system used for this work.

CHAPTER 3 - Results and Analysis

The objective of this work is to evaluate whether Er-doped III-N materials and devices synthesized by metal organic chemical vapor deposition (MOCVD) are a viable platform for new-age, chip-scale, current-injected optical amplifiers operating in the c-band of the telecommunication spectrum. This evaluation has an immense complexity unto itself, since the production of any efficient semiconductor device has many steps between the beginning growth substrate and the final working device. Thus, to provide simplicity to the evaluation process, the authors have created three subsets of the overall objective. The first subset is to achieve in-situ doping of Er into GaN/InGaN epilayers via the MOCVD process. The second subset is to understand the optical and structural properties of these Er-doped GaN/InGaN epilayers, and to study the effects of the MOCVD growth environment (V/III ratio, growth temperature, doping concentration, In alloying, etc.) on the optical and structural properties. The third subset is to apply optimized Er-doped GaN/InGaN epilayers to telecommunication device structures, and to characterize the efficiency and limitations of these devices.

3.1 Er-doped GaN

In order to understand the fundamental aspects of Er-doped GaN materials by MOCVD, simple material structures like that of Fig. 3-1 were grown. The samples were grown on commercial (0001) sapphire substrates provided by Honeywell Electronics. The sapphire substrates were 430 μm thick, and had an RMS z-profile deviation of 0.5 nm. Before growth, the samples were cleaned using acetone, isopropanol, and deionized water in an ultra-sonic bath. After insertion into the reaction chamber, the sapphire was heat treated at 1150 C for 10 minutes. The growth of these epilayers began with a thin GaN buffer layer, followed by a 1.2 μm GaN epilayer template, and a 0.5 μm Er-doped GaN layer. The GaN template and Er layer were grown at 10 torrs, and a T_G of 1040 C.

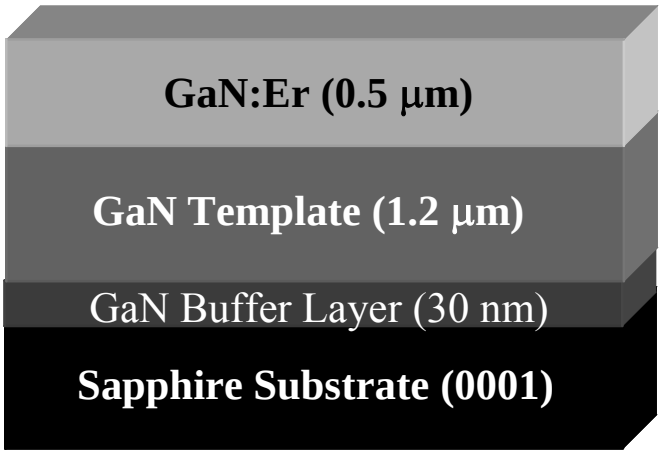

Figure 3-1 Block representation of the different layers of Er-doped GaN investigated in this work.

3.1.1 Optical Properties

Fig. 3-2 is the PL spectrum measured at 300 K of an optimized Er-doped GaN epilayer covering wavelengths from the visible to IR region, for an excitation wavelength (λ_{exc}) of 263 nm. Two sharp emission peaks are observed at wavelengths of 1.0 and 1.54 μm (with a full width at half maximum of 10.2 and 11.8 nm) corresponding to the radiative intra-4f Er^{3+} transitions from the $^4I_{11/2}$ (second excited state) and the $^4I_{13/2}$ (first excited state) to the $^4I_{15/2}$ (ground state), respectively. The room temperature PL intensity of the 1.54 μm peak is much larger than that of the 1.0 μm emission line. Fig. 3-2 also shows that virtually no visible emission lines generated by intra-4f transitions can be observed in Er-doped GaN epilayers grown by MOCVD. This is in sharp contrast to the results of Er-doped GaN obtained by MBE or ion-implantation, which exhibit the dominant intra-4f Er^{3+} transitions to be from the $^2H_{11/2}$ (537 nm) and $^4S_{3/2}$ (558 nm) to the $^4I_{15/2}$ ground state [53,56].

Fig. 3-2 also shows us that the dominant bandedge emission of Er-doped GaN at 300 K in is at 3.23 eV, which is red-shifted by 0.19 eV from the 3.42 eV bandedge emission of undoped GaN at 300 K [66]. The spectral red-shift of the bandedge emission in Er-doped GaN is related to the presence of Er. As explained later, it is believed that the 3.23 eV peak is from the recombination between electrons bound to an Er_{Ga}-V_N complex and free holes in the valence band. Here Er_{Ga} represents the substitution of Er onto the Ga sublattice and V_N is the nitrogen vacancy.

Fig. 3-3 is a comparison of the PL spectra of Er-doped GaN at 10 K, with above-bandgap excitation (λ_{exc} = 263) and below-bandgap excitation (λ_{exc} = 395 nm). It is observed that the PL intensity of the 1.54 μm emission with λ_{exc} = 263 nm excitation is more than 10 times larger than that with λ_{exc} = 395 nm. It is apparent that the above-bandgap excitation is much more efficient for the 1.54 μm emission. This result indicates that the generation of electron-hole (*e*-*h*) pairs results in a more efficient energy transfer to Er centers than through defect centers in the epilayers [57]. Thus, the subsequent optical amplifiers and emitters operating at 1.54 μm made from this material may be more efficient by employing an above-bandgap excitation scheme.

Figure 3-4 compares the shape of the PL spectra of the IR emission near 1.5 μm of Er-doped GaN for λ_{exc} = 263 nm between 10 and 450 K. It is evident that the 1.54 μm emission is dominant at low-temperatures. As the temperature is increased, the spectral nature of the Er

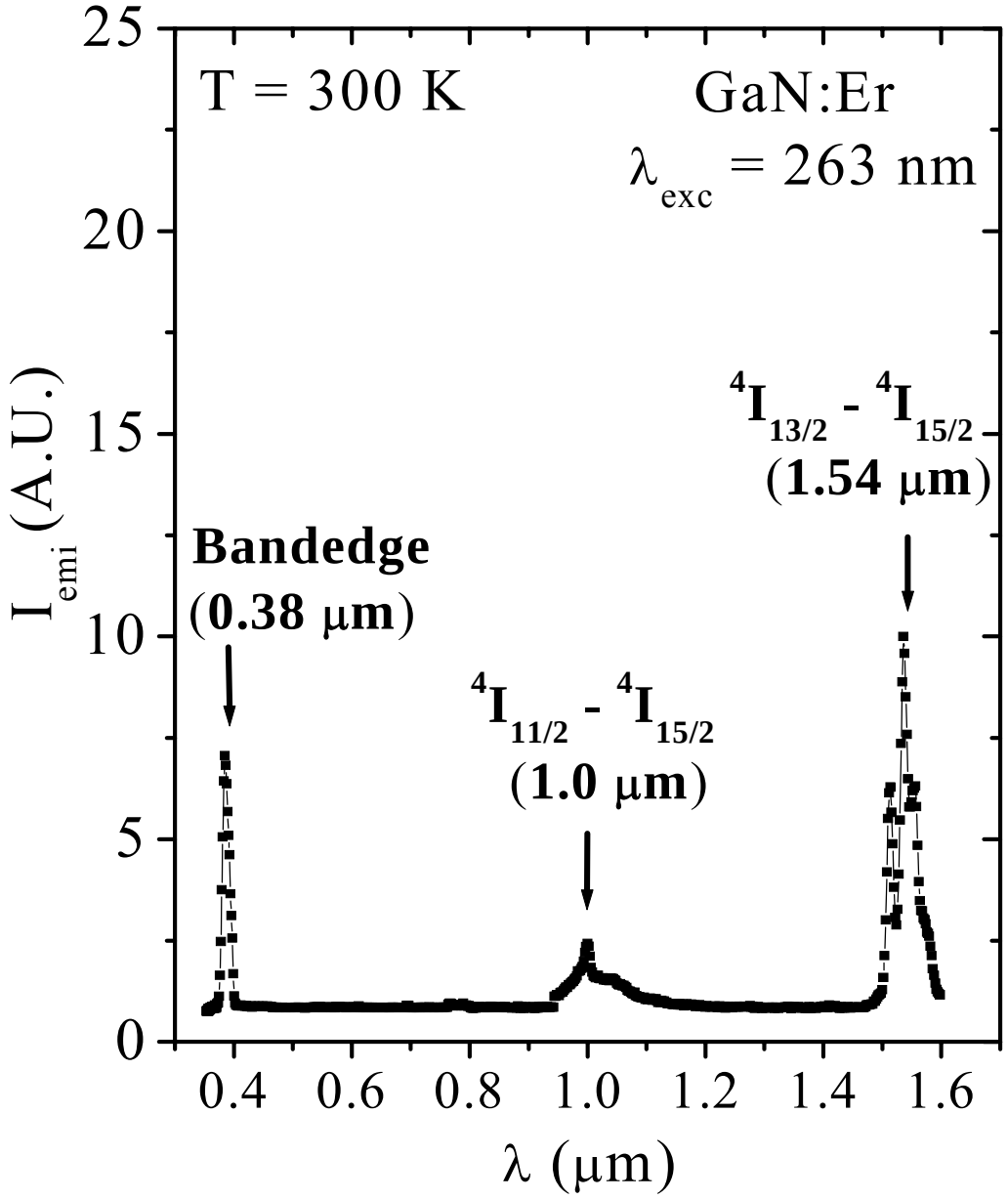

Figure 3-2 PL spectra of Er-doped GaN covering a broad spectral range from UV to IR for λ_{exc} = 263 nm at 300 K.

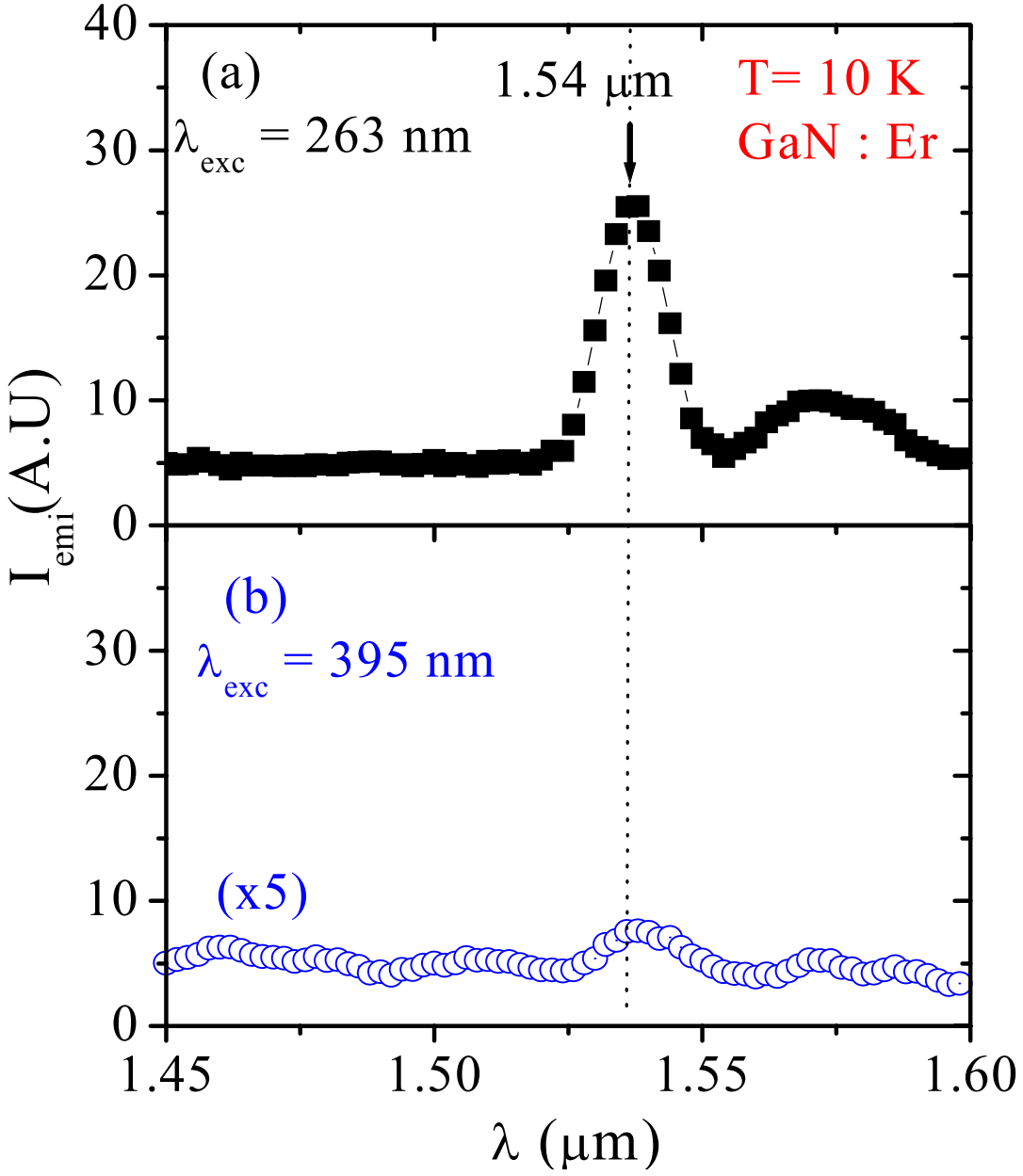

Figure 3-3 IR PL spectra of Er-doped GaN for a) λ_{exc} = 263 nm and b) λ_{exc} = 395 nm measured at 10 K.

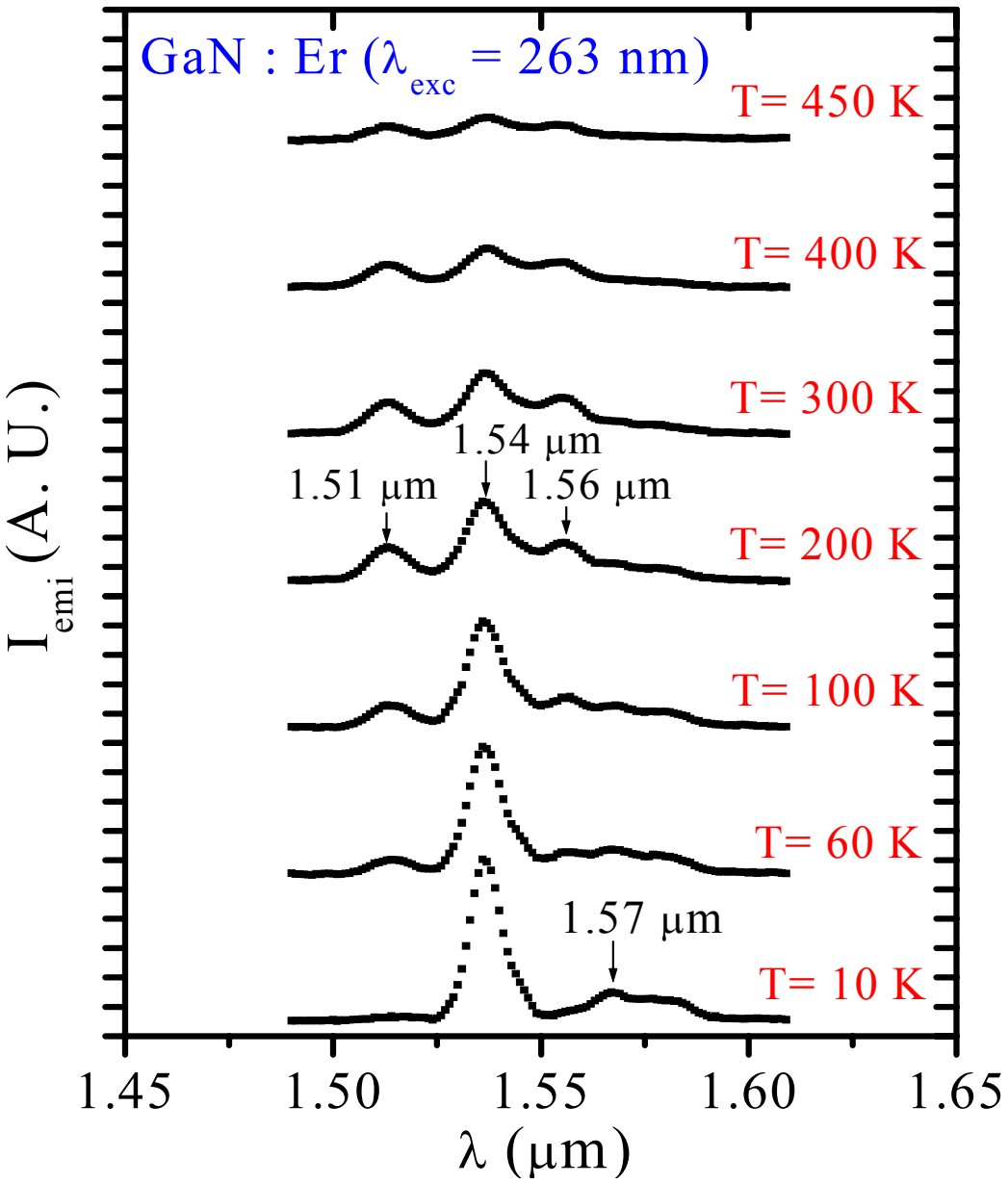

Figure 3-4 Comparison of the PL spectra of the IR emission in Er-doped GaN for λ_{exc} = 263 nm between 10 and 450 K.

emission changes as evident by the two additional emission peaks at 1.51 and 1.56 μm. The presence of these other peaks originates from the splitting of the $^4I_{13/2}$ due to the C_{3v} nature of the crystal field in GaN [67]. The presence of multiple peaks at room temperature for the Er-doped GaN system may allow for broadband optical amplification around the main c-band telecommunication wavelength (1.54 μm).

As explained earlier, it has been experimentally determined that the thermal quenching effect of the Er based PL emission is much larger in smaller bandgap semiconductors (SBGS) than WBGS. Since GaN is a WBGS, the integrated intensity of the 1.54 μm PL emission line for several temperatures was investigated to further verify this experimental observation. In Fig. 3-5, the integrated PL emission intensity (I_{int}) of the 1.54 μm emission line from Er-doped GaN for λ_{exc} = 263 nm is plotted as a function of temperature. The Er emission has a 20% decrease in I_{int} between 10 and 300 K, which represents the lowest reported degree of thermal quenching for rare-earth-doped GaN [50]. This result indicates that Er-doped GaN by MOCVD possesses one of the key properties required for new-age telecommunication materials.

In order to improve upon the thermal stability of this Er emission, a better understanding of the quenching mechanism must be determined. The data from Fig. 3-5 was fitted by the equation (3-1):

$$I_{\text{int}} = \frac{I_0}{1 + ce^{-\frac{E_0}{kT}}}, \qquad (3\text{-}1)$$

where I_0 is the integrated intensity at low-temperature, c is a fitting constant, E_0 is the activation energy of the thermal quenching, and k is Boltzmann's constant. The inset in Fig. 3-5 is an Arrhenius plot of the integrated PL emission intensity at 1.54 μm between 10 and 450 K. From this plot, an activation energy of 191 ± 8 meV was determined.

The density functional study of the Er-doped GaN system by Fihol et al. [68] showed that Er_{Ga}-V_N complexes in the Er-doped GaN system have a half-filled energy level at approximately 0.2 eV below the conduction band. This theoretical calculation is in good agreement with our experimental results obtained both from the activation energy of the 1.54 μm emission quenching and from the bandedge PL emission spectra. Thus, an Er trap-related donor level with an energy of 191 meV was identified and assigned to this Er_{Ga}-V_N complex. Our experimental results also match reasonably well with work by Song et al. [69], who used DLTS measurements

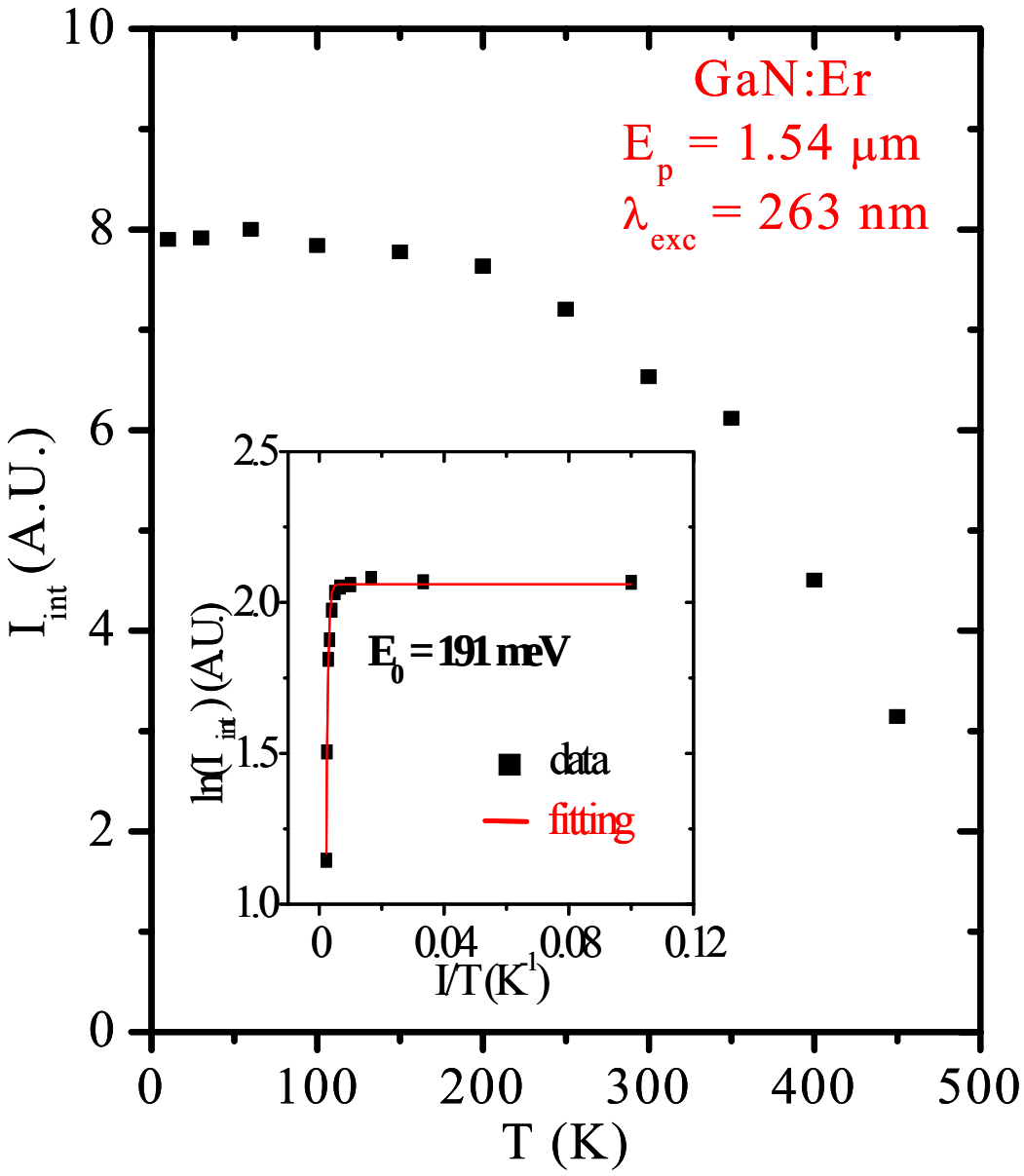

Figure 3-5 Integrated PL emission intensity of the 1.54 μm emission of Er-doped GaN between 10 and 450 K for λ_{exc} = 263 nm. The inset is an Arrhenius plot of the integrated PL intensity of the 1.54 μm emission.

on Er implanted GaN and measured an Er_{Ga}-V_N complex level of 188 meV below the conduction band. Thus, we conclude that the exchange of energy between the electrons bound to the Er_{Ga}-V_N complex (with an energy level at 191 meV) and the 4f cores states of Er is the dominant excitation mechanism of the 1.54 μm emission in MOCVD-grown Er-doped GaN using above-bandgap excitation.

Our results also provide a better understanding regarding the low degree of thermal quenching in WBGS. It is well established that for semiconductors, effective donor levels increase with increasing energy bandgap. The low degree of thermal quenching for Er-doped WBGS may be a result of this behavior. For smaller bandgap semiconductors, the majority of electrons bound to the Er traps are thermally excited into the conduction band even at low-temperatures since the binding energy is small. Thus, the electrons cannot efficiently transfer energy to the 4f electrons via an Auger-like process, resulting in a reduction of intra-4f excitation. But, for WBGS, the electrons remain bound to the Er related donor levels at higher temperatures since the energy levels are deeper. The Auger energy transfer between bound electrons and 4f electrons can still occur, and the subsequent thermal quenching is dramatically reduced.

In Figure 3-6, we compare in more detail the dominant bandedge emission of undoped and Er-doped GaN at 10 and 300 K for λ_{exc} = 263 nm. In contrast to the dominant bandedge transition of undoped GaN at room temperature of 3.42 eV [66], the dominant bandedge emission of Er-doped GaN is 3.23 eV. The difference in transition energies of the bandedge emissions for undoped and Er-doped GaN at room temperature (3.42 – 3.23 = 0.19 eV) coincides with that of the extrapolated thermal activation energy (0.191 eV). In order to further identify the nature of this transition, the dynamical behavior of the emission has been studied through time-resolved PL. The inset of Fig. 3-6 is the temporal response of the 3.23 eV PL emission peak in Er-doped GaN measured at 10 K. The lifetime of the 3.23 eV transition was determined to be 200 ps, which suggests that this is an impurity-to-band related transition [70]. Thus, the dominant 3.23 eV bandedge PL emission in Er-doped GaN is believed to be due to the recombination between electrons bound to the Er_{Ga}-V_N complex and free holes in the valence band.

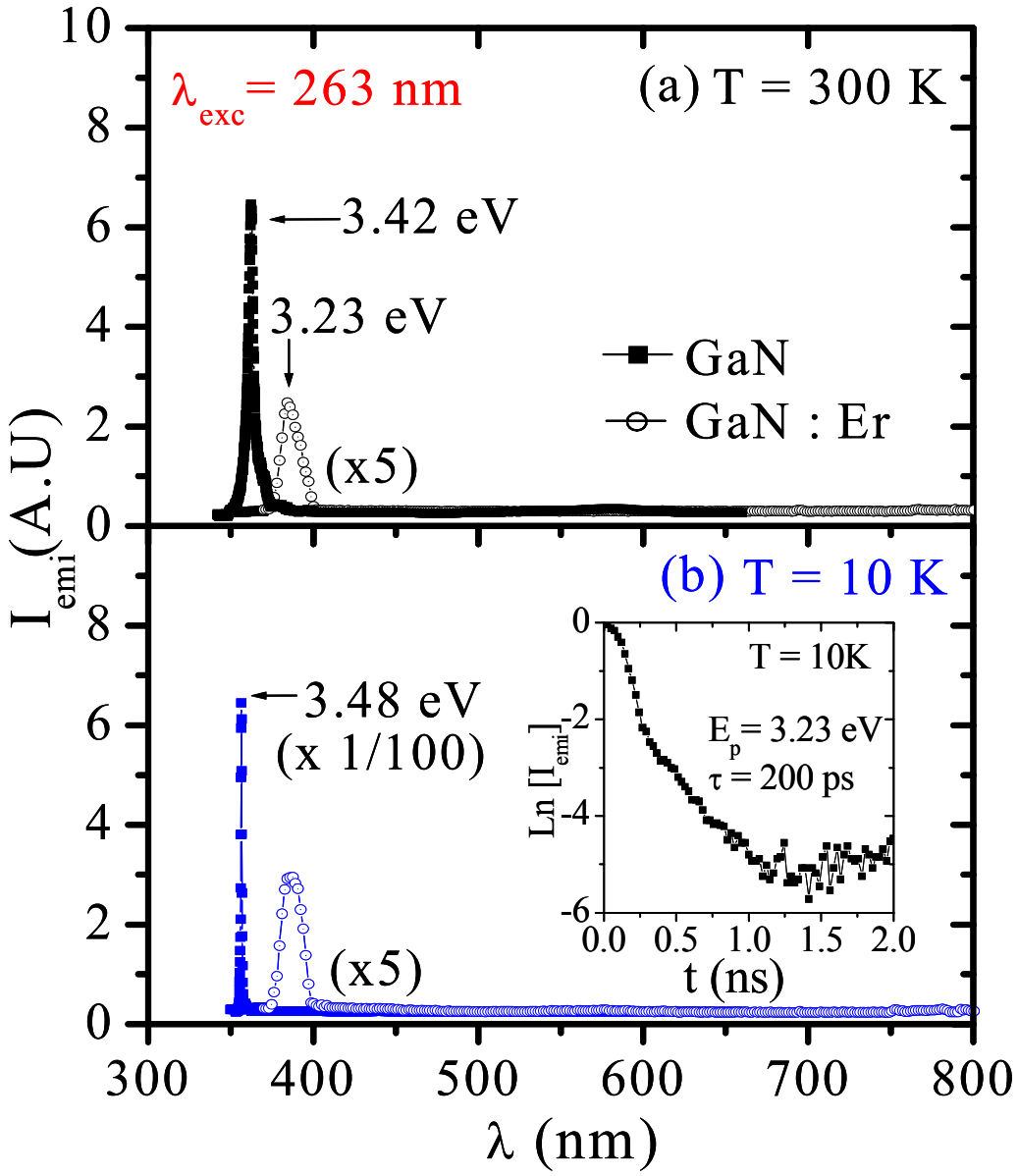

Figure 3-6 Comparison of the bandedge emission of undoped and Er-doped GaN at (a) 300 K and (b) 10 K for λ_{exc} = 263 nm. The inset is the temporal response of the 3.23 eV emission intensity in Er-doped GaN at 10 K.

3.1.2 Structural Properties

For Er-doped GaN to have candidacy as a next generation gain medium for the telecommunication industry, the Er dopant must not significantly perturb the crystalline nature of GaN. Thus, Er-doped GaN must retain both a high crystalline ordering and be free of other elements that may be parasitic to GaN devices. As mentioned in the experimental methods section, XRD rocking curves for the (002) peak of Er-doped GaN were utilized to probe crystalline ordering. Secondary ion mass spectroscopy (SIMS), performed by Evans Analytical Group, was used to determine the Er depth profile and to investigate the presence of other elements. Also, AFM images and OM were used to characterize the surface morphology of Er-doped GaN.

Fig. 3-7 is the SIMS profile for Er-doped GaN. The profile shows that Er concentrations (n_{Er}) up to 2 x 10^{21} cm^{-3} are possible. This number is comparable to previously reported n_{Er} in GaN synthesized by molecular beam epitaxy (MBE) [51], and much larger than any reported values of Er in InP, GaAs or Si [41,45,71]. Theoretical calculations show that n_{Er} larger than 10^{20} cm^{-3} are needed for gain values of 30 dB in waveguides less than 5 mm in length. Thus, we see here that Er-doped GaN via MOCVD satisfies yet another requirement for chip-scale amplifiers. Fig. 3-7 also shows that C and H concentrations are relatively low and similar in value to those achieved in high-quality undoped GaN [72]. Oxygen, a parasitic element to the electrical and optical properties of GaN, is not detectable in Er-doped GaN.

Fig. 3-8 is a rocking curve comparison of the (002) peak for both Er-doped GaN and high quality undoped GaN. It is widely accepted that the full width at half maximum (FWHM) of the rocking curve is a quantitative measure of the crystalline ordering. A smaller FWHM implies that more of the atoms within the crystalline plane have the same lattice parameter, implying that the crystalline ordering for small FWHM is much better than a crystal with a larger FWHM. Thus, by comparing the FWHM of both Er-doped GaN and GaN, we can determine the extent of the lattice perturbation due to the large Er concentration. As clearly seen in Fig. 3-8, the FWHM for the two samples are almost identical. The incorporation of such a large n_{Er} does not cause any significant change in the crystalline ordering, implying Er-doped GaN via MOCVD has a similar crystalline ordering to that of undoped GaN.

Fig. 3-9 is a comparison of the AFM images of high quality undoped GaN and Er-doped GaN with n_{Er} = 2 x 10^{20} cm^{-3} and 2 x 10^{21} cm^{-3}. Clearly, the surface of Er-doped GaN with n_{Er} =

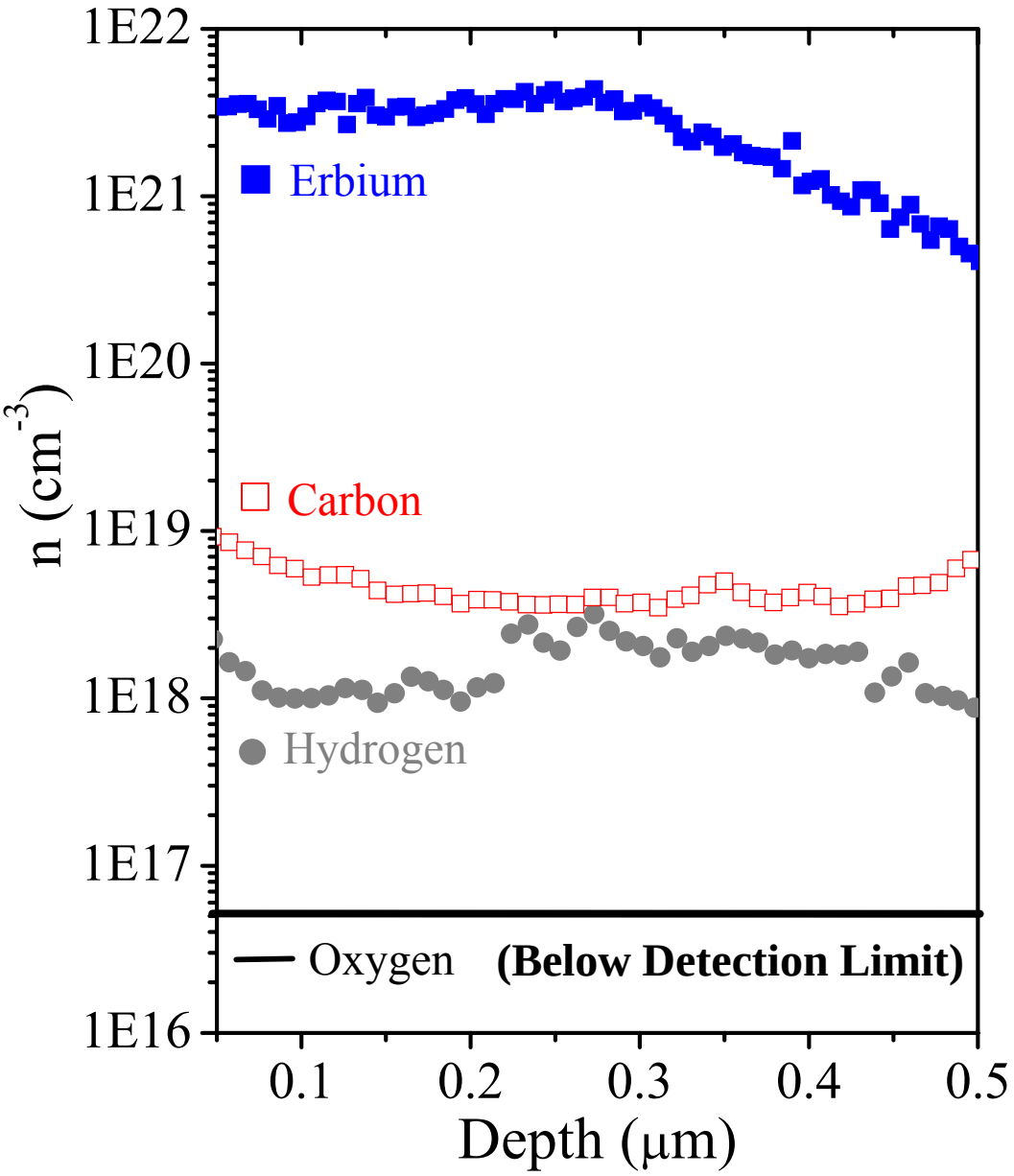

Figure 3-7 SIMS plot of Er-doped GaN grown by MOCVD performed by Evans Analytical Group.

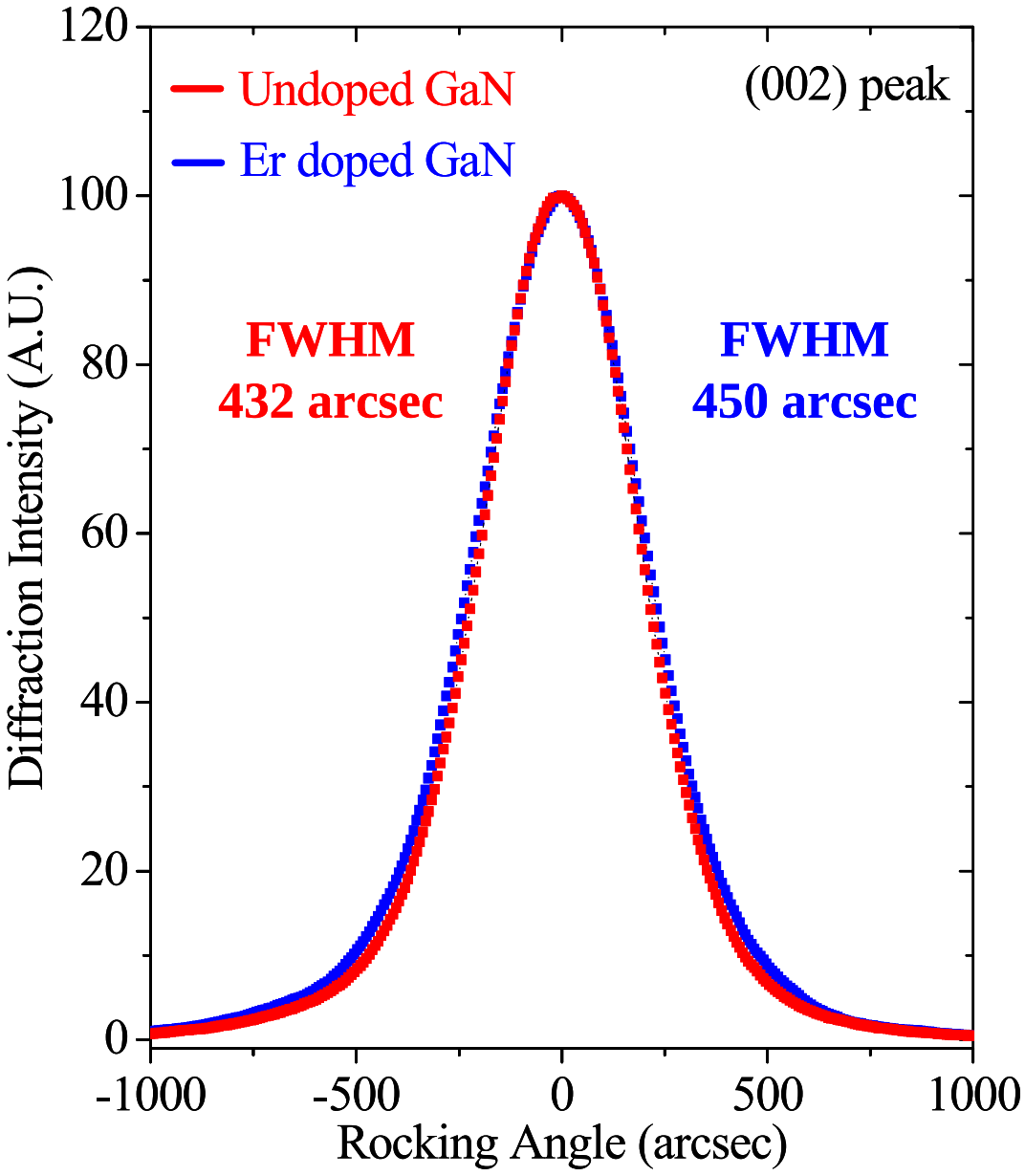

Figure 3-8 XRD rocking curve of the (002) peak of Er-doped GaN and undoped GaN. The colored numbers indicate the FWHM of the rocking curve of the (002) peak.

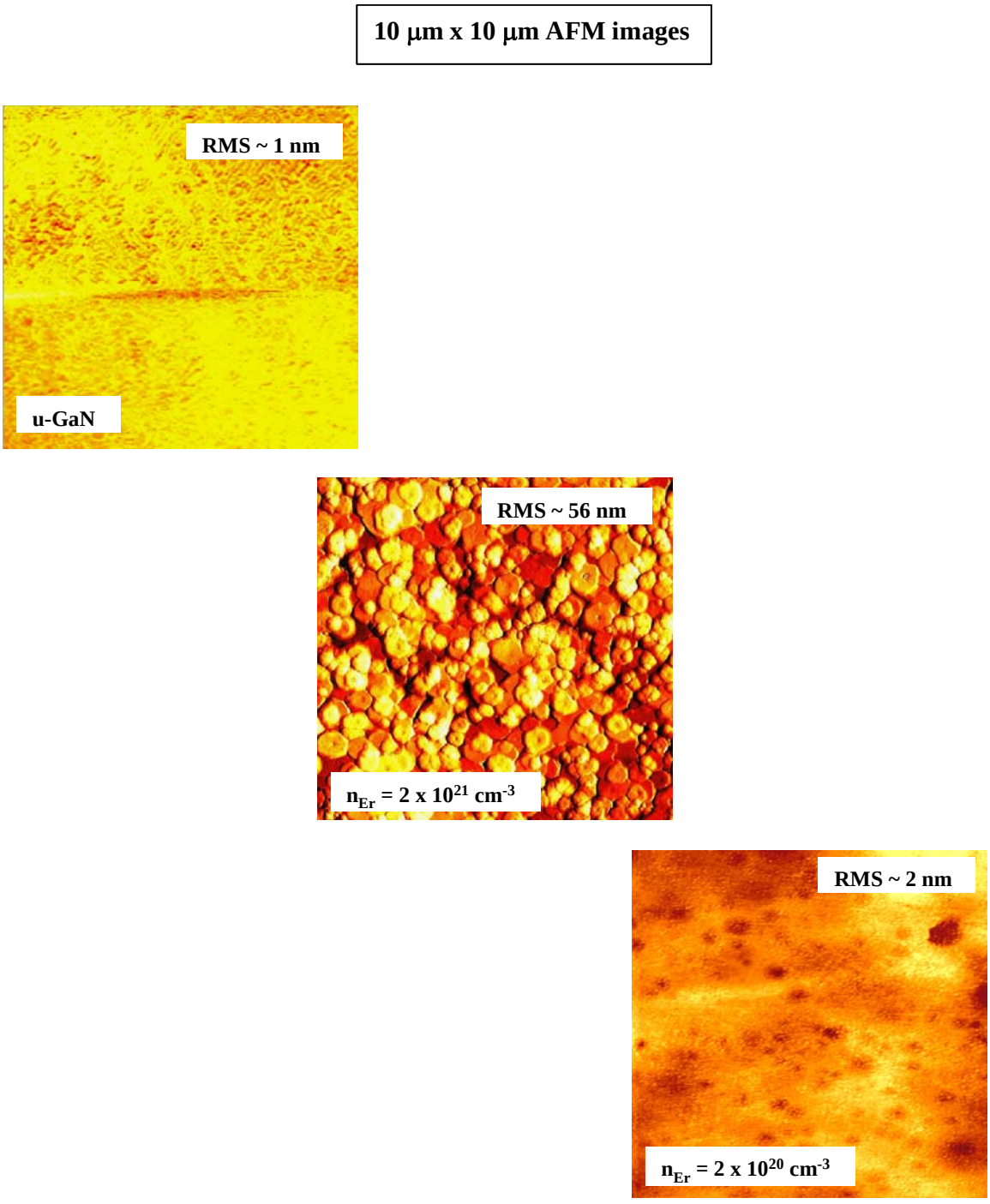

Figure 3-9 10 x 10 μm AFM images of undoped GaN, Er-doped GaN (n_{Er} = 2 x 10^{21} cm^{-3}), and Er-doped GaN (n_{Er} = 2 x 10^{20} cm^{-3}). The number in the top right of each image represents the root mean square (RMS) deviation of the z-height for each epilayer.

2 x 10^{21} cm^{-3} suffers from a large degradation in surface smoothness. The RMS deviation in the z-dimension is ~ 56 nm, which is much higher than the atomically flat value of 1.0 nm for that of undoped GaN. For device applications, a surface roughness RMS value below 3 nm is preferred. The sample with n_{Er} = 2 x 10^{20} cm^{-3} , however, has an RMS value of 2 nm, which more than meets the 3 nm preference. Thus, the most of the materials and devices studied in this work contained n_{Er} = 2 x 10^{20} cm^{-3} in order to be device-applicable.

3.1.3 Growth Environment

Of equal importance to an understanding of the optical and structural properties of Er-doped GaN is an understanding of the effect of the growth environment on the emission intensity and crystalline properties. Varying such growth conditions as the V/III ratio (the ratio between the NH_3 and group-III precursor concentration), T_G, P_G, and dopant concentration induce changes within the crystal that alter the optical and structural properties. The change in the crystal properties will in turn alter the excitation dynamics of the Er system thus changing the emission intensity. In order to apply these epilayers to device platforms, the surface roughness, crystalline quality, and emission intensity for different growth environments will have to be optimized.

In this work several Er-doped GaN epilayers were grown at different T_G with an epilayer structure identical to that used in the study on the optical properties (see Fig. 3-1) Fig. 3-10 is a plot of the PL spectra at 300 K of Er-doped GaN for T_G between 890 and 1060 C for λ_{exc} = 263 nm. Temperatures above 1060 C were not implemented due to rapid deterioration of the surface due to particle desorption. Fig. 3-10 clearly shows that the profile of the emission spectra remains relatively unchanged for each T_G, yet the intensity increases significantly with increasing T_G. In order to obtain an understanding between T_G and PL emission intensity, the integrated intensity of the 1.54 μm PL emission vs. T_G was plotted. The inset to Fig. 3-10 is the least squared fit to the integrated intensity of the 1.54 μm PL emission data points using the equation,

$$I = I_0 e^{-E_F / kT} \tag{3-2}$$

where k is the Boltzmann constant, E_F is the formation energy of the Er emitting center, and I_0 is a fitting constant. The calculated formation energy for the Er-emitting centers in Er-doped GaN

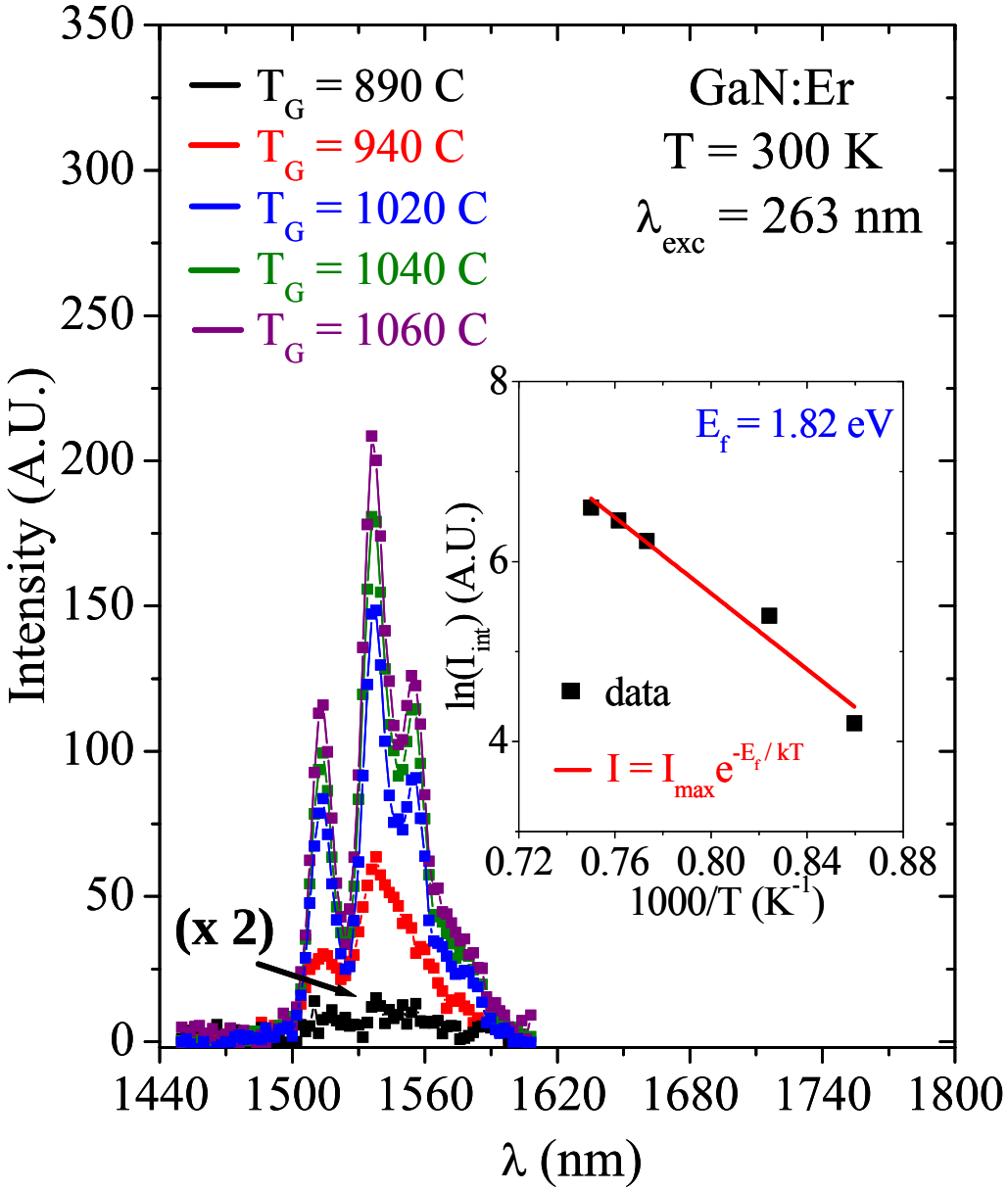

Figure 3-10 PL spectra measured at 300 K of Er-doped GaN for λ_{exc} = 263 nm for T_G =890, 940, 1020, 1040, and 1060 C. The inset is an arrhenious plot of the integrated PL intensity of the 1.54 μm emission. The red line is the least squares fit of the data points according to equation listed in the inset. The value of E_F determined from the least squares fit is 1.82 ± 0.1 eV.

is 1.82 eV ± 0.1 eV. It is well understood that the formation energy of a defect/impurity is a numerical measure of the probability of that defect/impurity being formed at a fixed growth temperature. Larger formation energies imply that larger T_G must be used to incorporate a larger concentration of the impurity/defect. The calculated value of the formation energy of the Er emitting center for Er-doped GaN is rather large, and it implies that higher T_G must be utilized for high Er emitting center concentrations. Recently, our group showed the dominant Er-emitting centers in Er-doped GaN by MOCVD to be an Er-V_N complex [73]. Thus, we identify here that the formation energy of that complex to be 1.82 eV ± 0.1 eV.

Fig. 3-11 is a comparison of the surface and crystalline ordering as a function of T_G. The left portion of Fig. 3-11 is a comparison of the optical images (magnification = 750 x) of Er-doped GaN for T_G = 890, 940, 1020, 1040, and 1060 C. The right portion of Fig. 3-10 is a plot of the numerical values of the FWHM of the (002) curve for the same T_G. For all five growth temperatures, the linewidth remains relatively unchanged. This implies that the growth temperature does not perturb the crystalline ordering, and that each sample has a high degree of crystalline quality. However, as T_G increases, the surface becomes very distorted, and the surface changes from atomically flat to containing large clusters. The change in surface morphology can be attributed to the increasing incorporation of Er-emitting centers. At low-temperatures, there is not sufficient thermal energy for a large incorporation of Er-emitting centers because of their large formation energy. Thus, very little perturbation to the in-plane lattice occurs by the Er-emitting centers that have different lattice spacing. The small change in lattice structure leads to relatively flat surface morphologies. As the temperature increases, more emitting centers are incorporated into the epilayer. An increased number of Er centers will induce more stress in the monolayer resulting in the growth of distorted surfaces.

In conjunction with the effect of growth temperature on the crystalline properties, is the interaction between Er and the other source gases involved in the MOCVD process. Since the synthesis of Er-doped GaN via MOCVD has not been accomplished to date, the gas phase interaction of the Er precursor with NH_3 or the other commonly used gases is completely unknown. In order to prepare Er-doped GaN epilayers for device applications, this interaction must be understood. In an ideal growth setting for MOCVD, the group-III source and the group-V source have negligible chemical interaction before encountering the reaction zone above the substrate. The two precursors would then pyrolize in the reaction zone due to the elevated

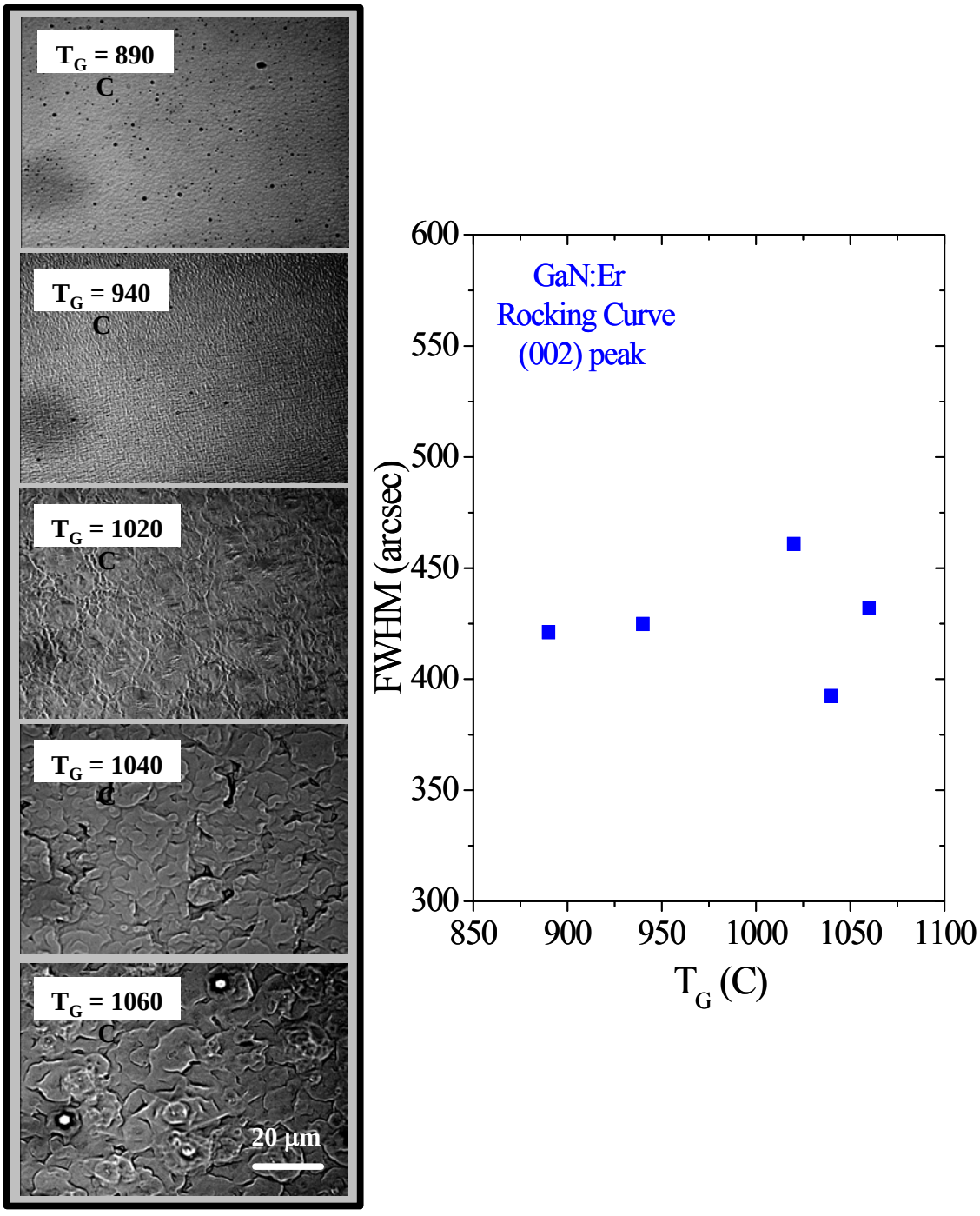

Figure 3-11 (left) Optical microscope images (magnification = 750 x) of Er-doped GaN for T_g = 890, 940, 1020, 1040, and 1060 C. (right) Plot of FWHM of the (002) rocking curve of Er-doped GaN as a function of T_G.

temperatures, and the group-III atoms and group-V atoms would adsorb onto the surface. However, in the case of MOCVD growth of GaN, the reaction between the commonly used precursors is not so ideal.

Separately, the decomposition of TMGa and NH_3 is well understood. The decomposition of TMGa begins with the removal of the first and second methyl radicals, with activation energies of 58-60 kcal/mol and 35.4 kcal/mol, respectively [74]. At the growth temperatures commonly employed for high-quality GaN epilayers (~ 1000 C), the TMGa is completely pyrolized in the reaction zone. But, in contrast to the TMGa, only a fraction of the NH_3 precursor dissociates at 1000 C due to the much larger bonding energy of NH_3 [74]. In order to alleviate this low supply of atomic nitrogen, common MOCVD growth environments for GaN have a large V/III ratio.

Studies have shown that the heterogeneous decomposition of NH_3 with TMGa is an important process during GaN growth [74,75]. It has been shown that at temperatures far below typical GaN growth environments, adducts formed between TMGa and NH_3 are the dominant gas species. These adducts provide a much higher decomposition rate at 1000 C than that of NH_3, and are thus the main species involved with the growth of GaN. However, without careful reactor design, prolonged interaction of TMGa and NH_3 before the reaction zone can lead to non-uniformities and poor crystalline qualities. This result has led MOCVD engineers to design reactor systems that eliminate unwanted precursor exposure via low growth pressures, isolated precursor doping lines, and large gas velocities.

In this work, several Er-doped GaN epilayers were grown with varying NH_3 and Er flow rates in order to evaluate the interaction between the Er precursor and NH_3. The sample structure is identical with Fig. 3-1, and T_G was fixed at 1040 C with P_G = 10 torrs. Fig. 3-12 is a comparison of the surface and crystalline ordering as a function of NH_3 flow rate for fixed Ga and Er flow rate. The left portion of Fig. 3-12 is a comparison of the optical images (magnification = 100 x) of Er-doped GaN for NH_3 = 0.2, 0.4, 0.6, 0.8, 1.0, and 1.2 l/min. The right portion of Fig. 3-12 is a plot of the numerical values of the FWHM of the (002) curve for the same NH_3 flow rates. The FWHM does not change significantly despite the changing NH_3 flow rate, indicating that the crystalline ordering is relatively un-perturbed. However, the optical images from Fig. 3-12 clearly show a changing surface morphology for each NH_3 flow rate. At higher NH_3 flow rates, we see a large density of hexagonal

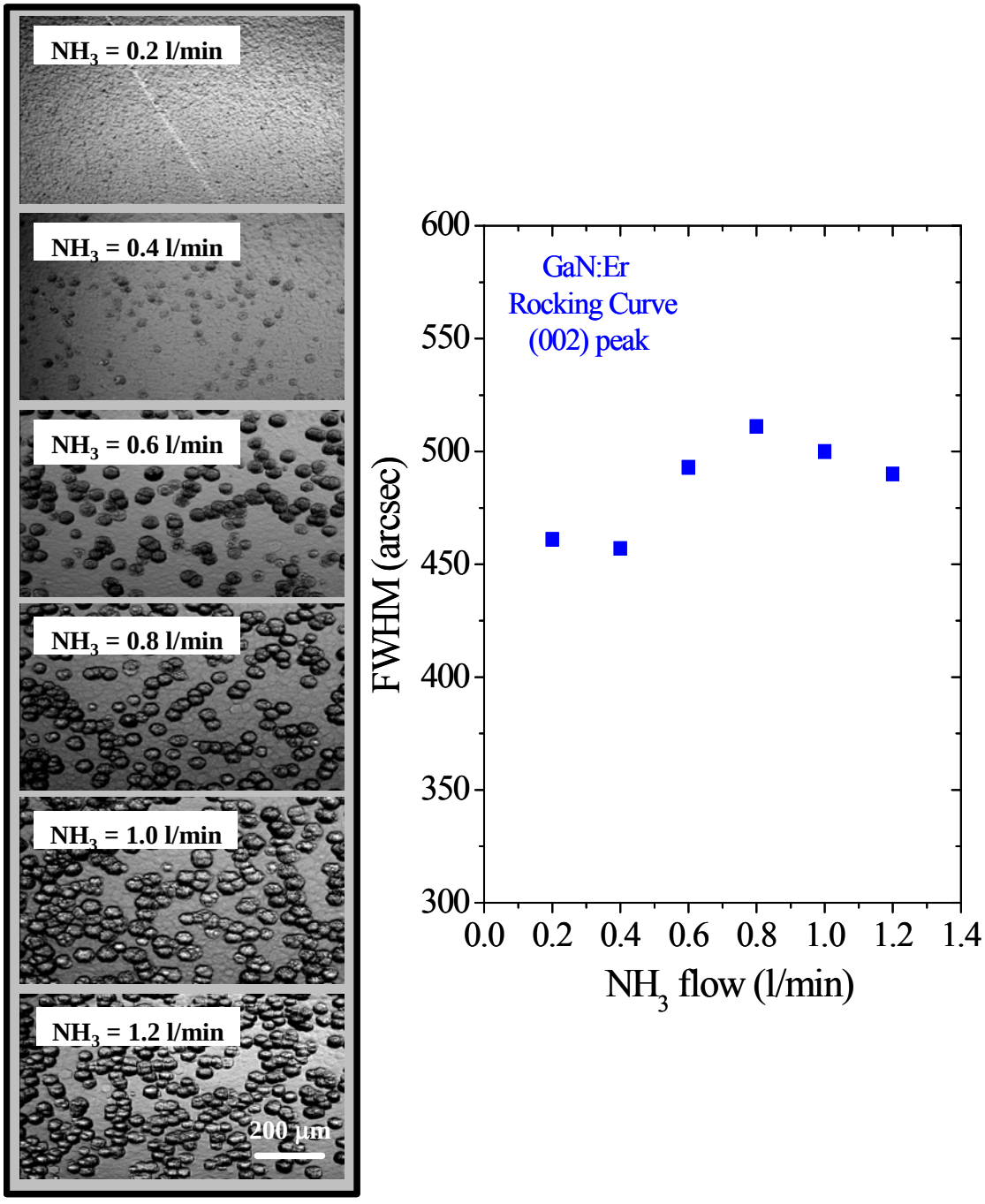

Figure 3-12 (left) Optical microscope images (magnification = 100 x) of Er-doped GaN for NH_3 = 0.2, 0.4, 0.6, 0.8, 1.0, and 1.2 l/min. (right) Plot of FWHM of the (002) rocking curve of Er-doped GaN as a function of NH_3 flow rate.

pyramids (~ 30 - 40 μm in diameter) forming on the surface, while lower NH_3 flow rates contain much smaller densities. For the smallest NH_3 flow rate, the pyramids have disappeared completely. Note the dimensions of the pyramid clusters are independent of the NH_3 flow rate.

Fig. 3-13 is the PL spectra of Er-doped GaN at 300 K for λ_{exc} = 263 nm and NH_3 flow rates of 0.2, 0.4, 0.6, 0.8, 1.0, and 1.2 l/min. As the NH_3 flow rate decreases, the PL intensity decreases as well. Since the crystalline quality does not change for the varying NH_3 flow rates, the change in PL intensity cannot be related to a change in crystalline ordering, and it must be related to a gas phase reaction of the Er precursor with NH_3. Since the PL intensity increases with increasing NH_3 flow rate similar to the increase in cluster density with increasing NH_3 flow rate, it is suggested that the pyramidal clusters are a result of adduct formation between the NH_3 and Er precursor. As the NH_3 flow rate increases, more adducts are formed in the gas phase leading to a higher density of surface clusters. These surface clusters would in turn be Er rich, causing an increase in PL intensity.

To investigate the relationship between the NH_3 and Er precursor further, Er-doped GaN with a varying Er flow rate and constant Ga and NH_3 flow rate were synthesized. Again, the epilayer structure is that of Fig. 3-1, and all other growth parameters (pressure, temperature) were fixed. Fig. 3-14 is a comparison of the surface and crystalline ordering as a function of Er flow rate. The left portion of Fig. 3-14 is a comparison of the optical images (magnification = 500 x) of Er-doped GaN for Er = 32, 63, 125, 250, and 500 ml/min. The right portion of Fig. 3-14 is a plot of the numerical values of the FWHM of the (002) curve for the same Er flow rates. In contrast to the change in pyramid density as a result of a varying NH_3 flow rate, a varying Er flow rate causes the diameter of the pyramids to change. At Er flow rates below 125 ml/min, no surface clusters are present. For Er flow rates between 125 – 500 ml/min, we see that the diameter of the clusters increases, changing from 3 – 5 μm in diameters up to 30 – 40 μm (see numerical values inset into Fig. 3-14).

Fig. 3-15 is the IR PL spectra measured at 300 K for λ_{exc} = 263 nm and Er = 32, 63, 125, 250, and 500 ml/min. The shape of the emission profile does not change for the varying Er flow rate, but the emission intensity does decrease with decreasing Er flow rate. In fact, at Er flow rates below 125 ml/min, no PL signal was detected. The correlation between surface cluster size and PL intensity for varying Er flow rate is further evidence that the clusters are in fact Er rich centers, and that the gas phase interaction between the Er precursor and NH_3 drastically effects

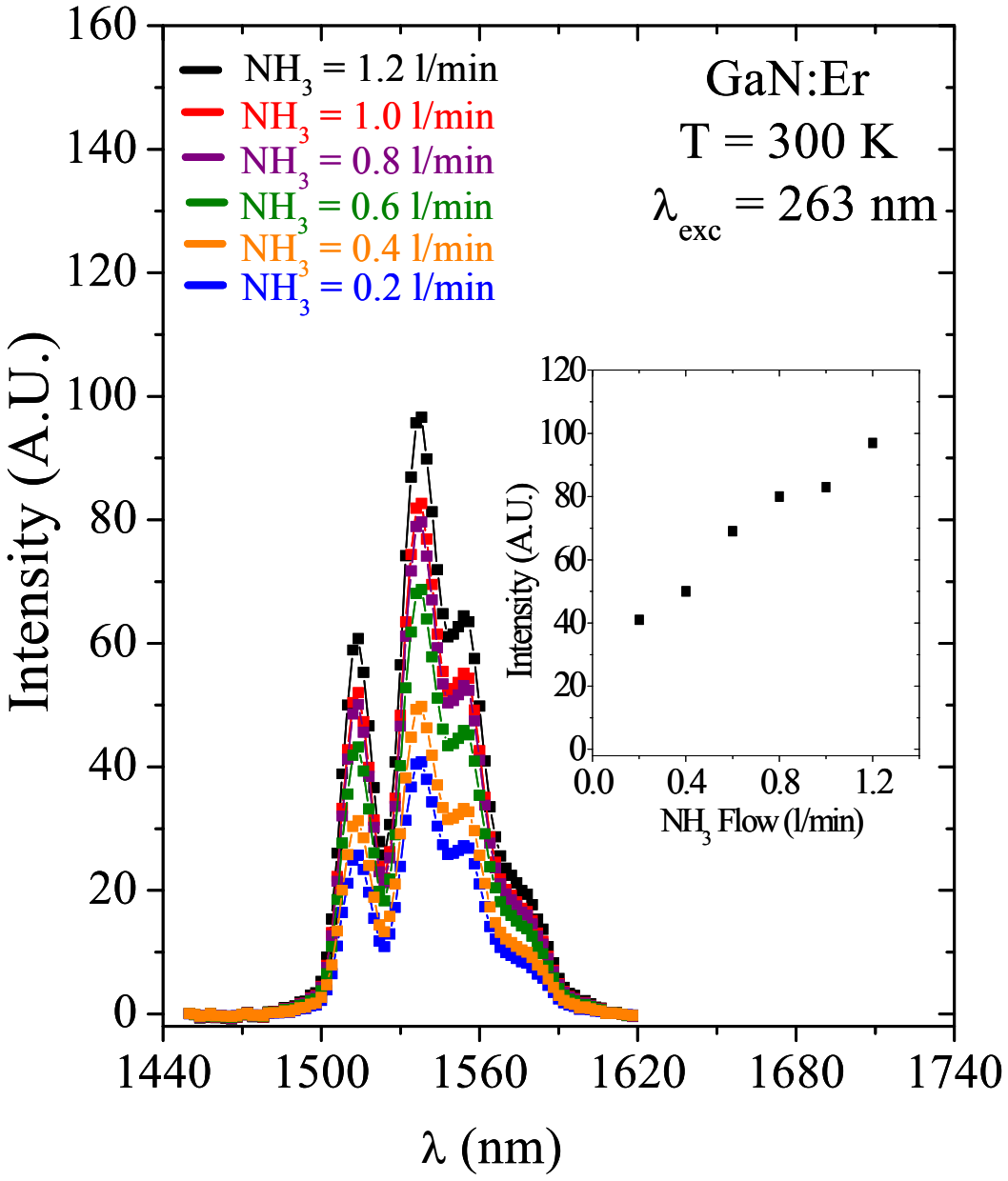

Figure 3-13 PL spectra measured at 300 K of Er-doped GaN for λ_{exc} = 263 nm for NH_3 flow rates of 0.2, 0.4, 0.6, 0.8, 1.0, and 1.2 l/min. The insert is the peak intensity of the 1.54 μm PL emission vs. NH_3 flow rate.

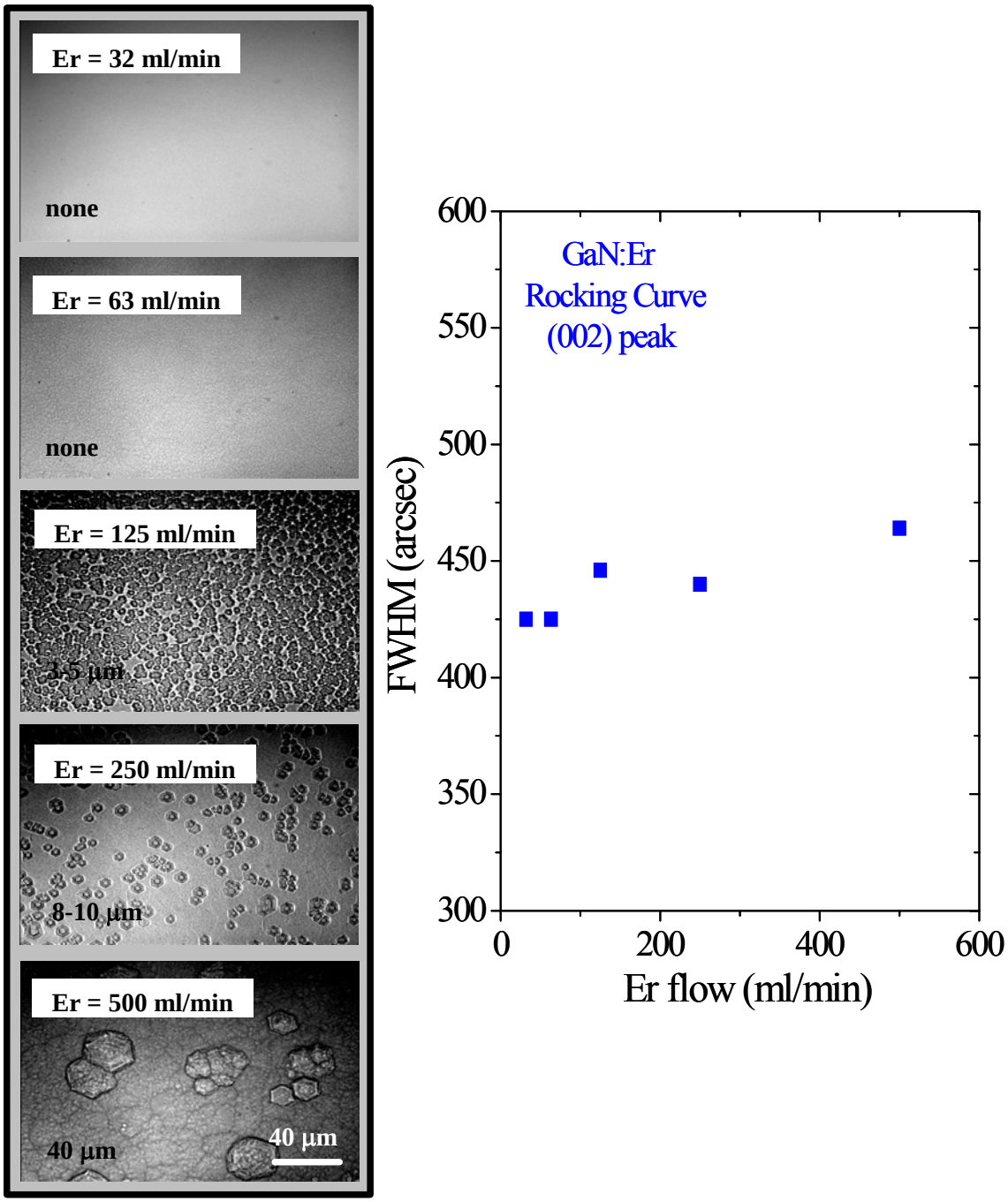

Figure 3-14 (left) Optical microscope images (magnification = 500 x) of Er-doped GaN for Er = 32, 63, 125, 250, and 500 ml/min. The numbers in the lower left represent the average cluster diameter. (right) Plot of FWHM of the (002) rocking curve of Er-doped GaN as a function of Er flow rate.

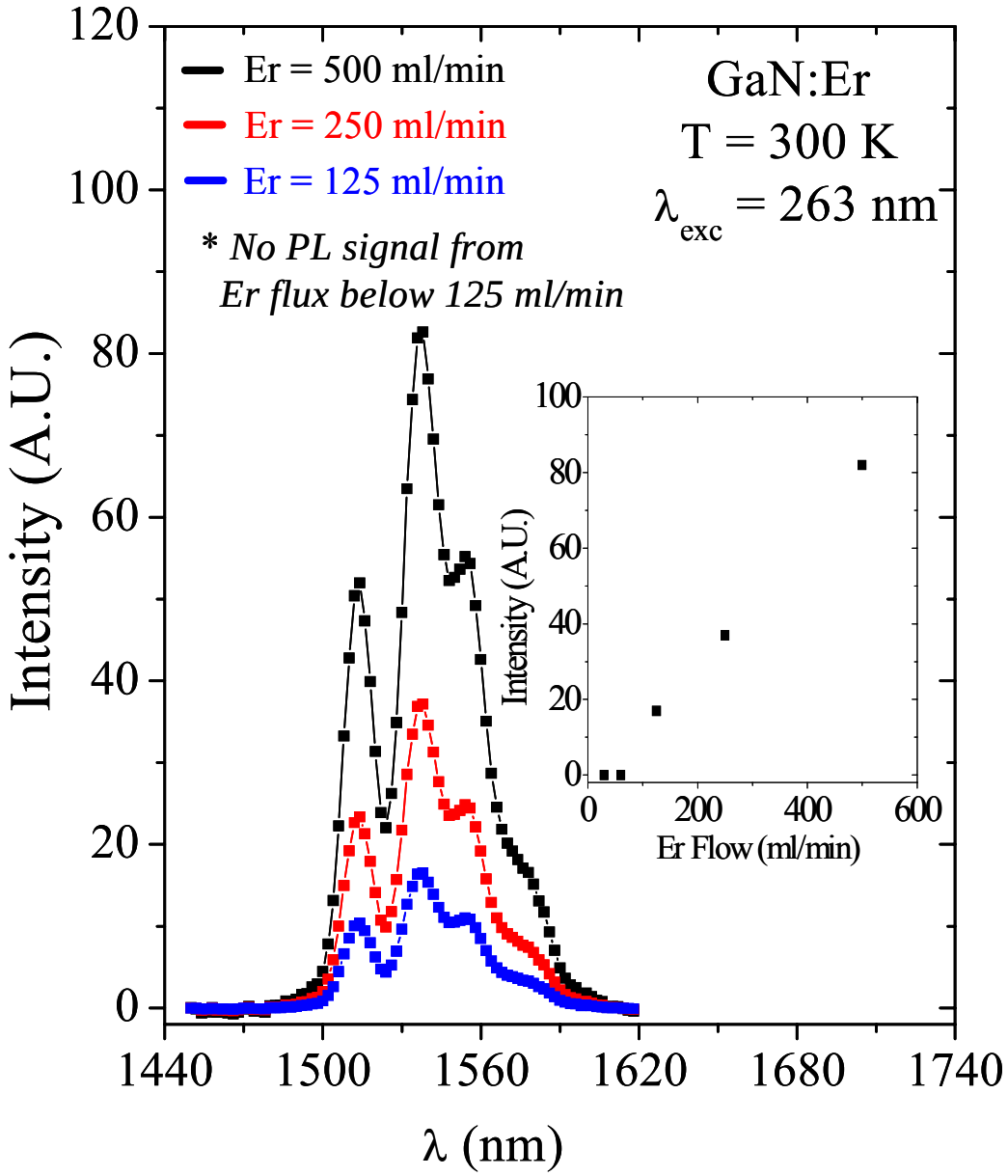

Figure 3-15 PL spectra measured at 300 K of Er-doped GaN for λ_{exc} = 263 nm for Er flow rates of 31, 63, 125, 250, and 500 ml/min. The insert is the peak intensity of the 1.54 μm PL emission vs. Er flow rate.

the Er concentration. At larger values of Er flow rate, more Er molecules are present for adduct formation with NH_3 causing larger adduct size. The larger adducts result in surface clusters with a larger diameter. The larger diameter clusters would have more Er resulting in larger PL intensities. At smaller Er flow rates, the lacking number of Er molecules form adducts of smaller diameter and thus result in smaller diameter surface clusters. The smaller clusters have less Er, thus resulting in a smaller PL intensity. At Er flow rates below 125 ml/min, there is an insufficient amount of Er precursor to form adducts with NH_3. Thus, no surface clusters form, and the PL emission cannot be detected.

Another way to examine the interaction between the Er precursor and NH_3, is to vary the speed of the carrier gas. By adjusting the total flow rate of the carrier gas while keeping the NH_3 and Er flow rate constant, the volume fraction of the two precursors remains constant while the speed of the gas changes. As the gas speed increases, the exposure time between the two gas species is reduced, thus reducing the likelihood of adduct formation. Fig. 3-16 is a comparison of the surface and crystalline ordering as a function of H_2 flow rate. The left portion of Fig. 3-16 is a comparison of the optical images (magnification = 100 x) of Er-doped GaN for H_2 = 0.4, 0.8, 1.2, 1.5, and 2.0 l/min. The right portion of Fig. 3-16 is a plot of the numerical values of the FWHM of the (002) curve for the same H_2 flow rates. The OM images show little deviation in surface cluster density or size over the range of H_2 flow rate. The small change in surface morphology may indicate that only a small amount of adduct is formed between the Er precursor and the NH_3 for the carrier gas flow rates studied

Fig. 3-17 is a plot of the PL spectra in the IR region of Er-doped GaN at 300 K for λ_{exc} = 263 nm for H_2 = 0.4, 0.8, 1.2, 1.5, and 2.0 l/min . From Fig. 24 we see that the PL intensity increases as the carrier gas flow rate rate decreases. A slower gas flow rate (longer exposure time between the Er precursor and NH_3) results in a higher PL intensity. Thus, the longer exposure time seems to allow a slight increase in adducts formed between the Er precursor and NH_3, thus increasing the Er-emitting centers (PL intensity) contained in the clusters.

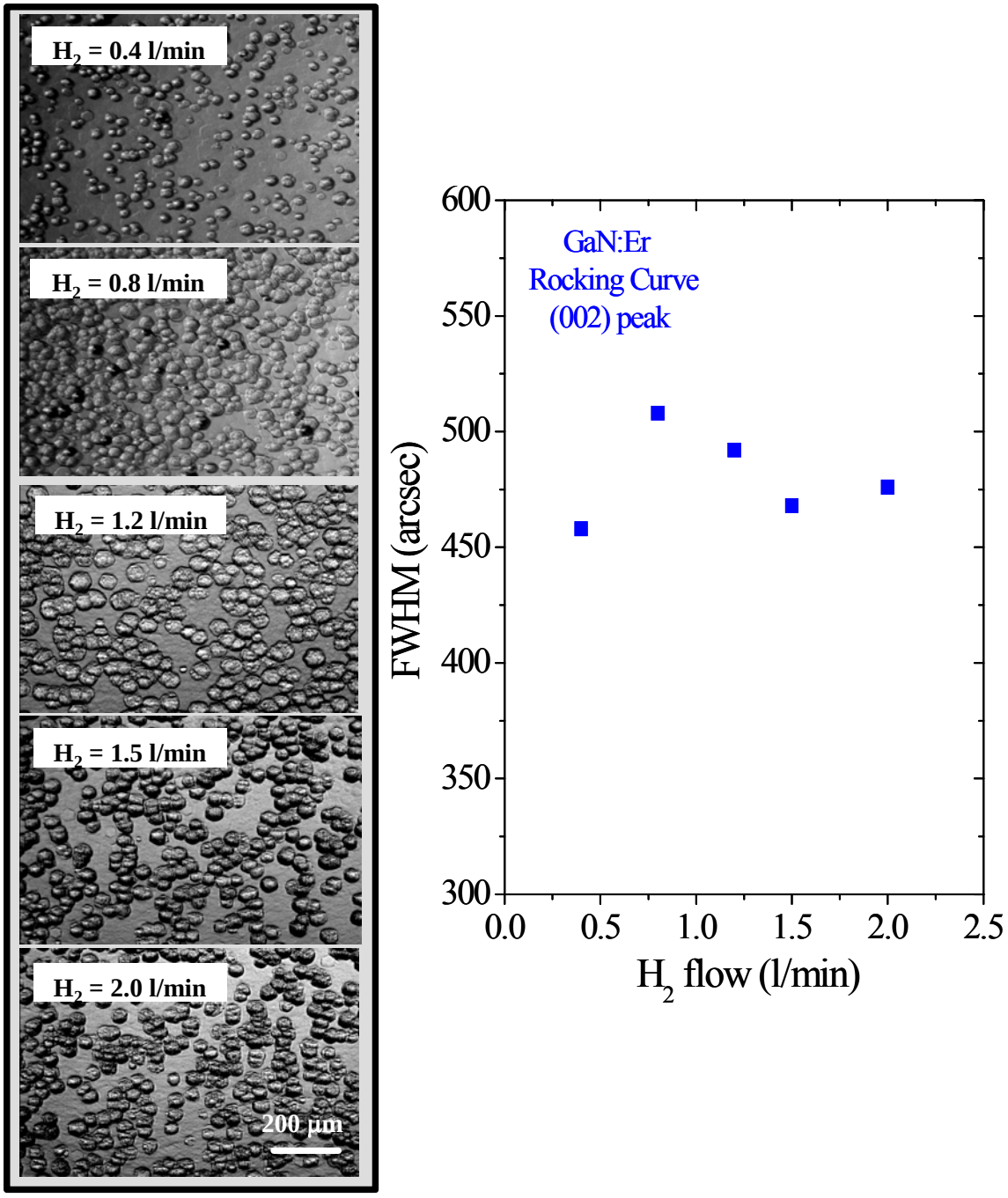

Figure 3-16 (left) Optical microscope images (magnification = 100 x) of Er-doped GaN for H_2 = 0.4, 0.8, 1.2, 1.5, and 2.0 l/min. (right) Plot of FWHM of the (002) rocking curve of Er-doped GaN as a function of H_2 flow rate.

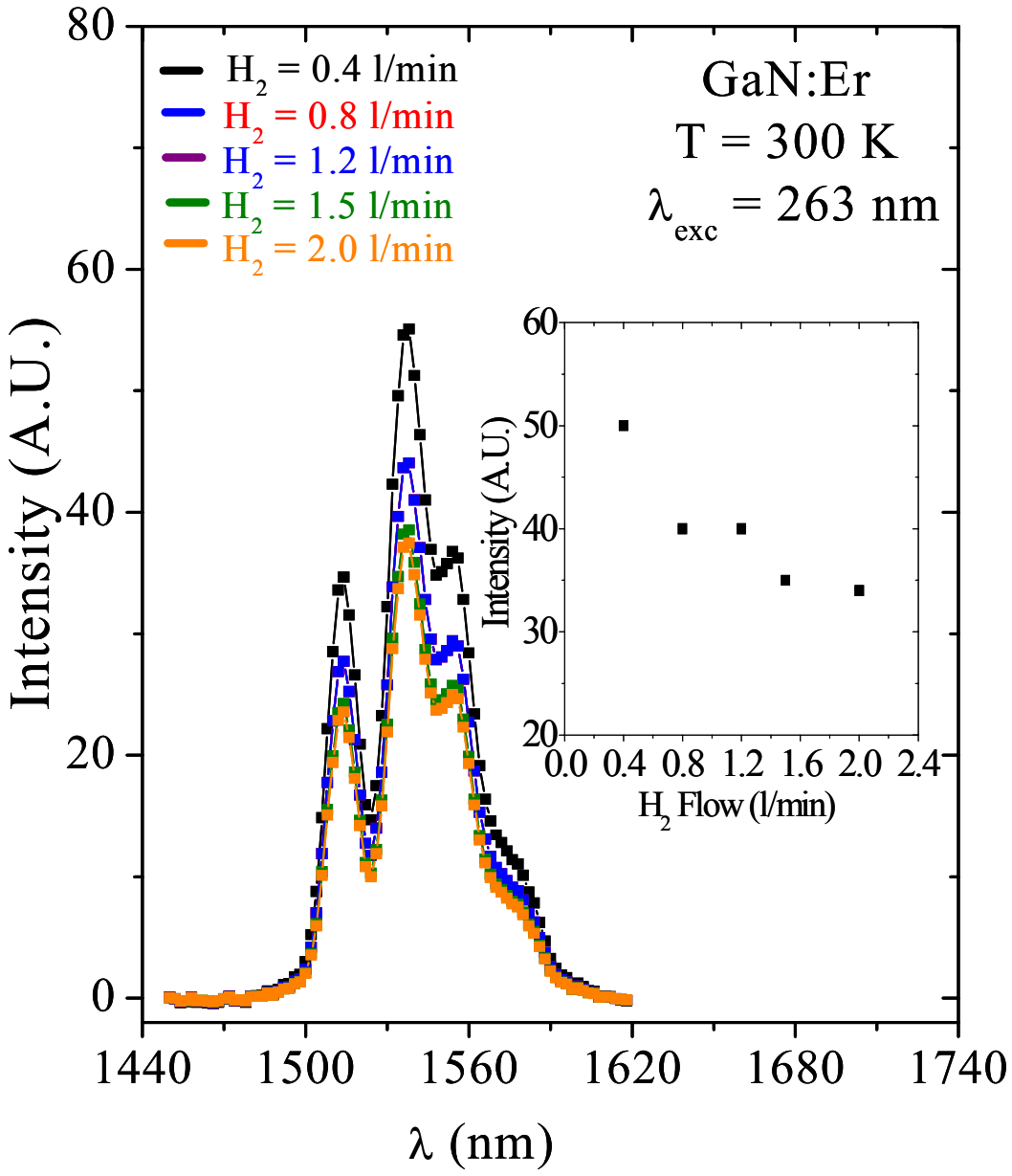

Figure 3-17 PL spectra measured at 300 K of Er-doped GaN for λ_{exc} = 263 nm for H_2 flow rates of 0.4, 0.8, 1.2, 1.5 and 2.0 l/min. The insert is the peak intensity of the 1.54 μm PL emission vs. H_2 flow.

3.2 Er-doped InGaN

In the study of the optical properties of Er-doped GaN, it was determined that the excitation of the Er centers was far more efficient using above-bandgap energy. Thus, in employing Er-doped GaN as the amplification medium in devices operating at 1.54 μm, LEDs at wavelengths below 360 nm would have to be used in order to take advantage of this highly efficient excitation method. Although LEDs at these wavelengths have been realized, the efficiency of these emitters is far too low for commercial applications. However, blue and green LEDs are a very mature technology, and would be a great candidate for monolithically integratable excitation sources. Although blue/green wavelengths are of energy insufficient for above-bandgap excitation of GaN, InGaN alloys have a much lower bandgap energy and could be tailored to fit the excitation wavelength of high-power blue and green LEDs through tertiary alloying. Thus, if highly efficient Er-doped InGaN epilayers could be achieved, they might be a much more suitable gain medium for new-age telecommunication devices.

Over the last 10 years, huge advancements in blue/green LED efficiencies have occurred. Currently, commercial LEDs at wavelengths of 405 – 460 nm have external quantum efficiencies of 20 – 40 %. Thus, Er-doped InGaN epilayers with bandgap energies lower than the equivalent wavelength energies would be excited using an above-bandgap mechanism, and may be ideal amplification media for telecommunication devices. Experiments have shown that the bandgap energy of the InGaN alloy spectrum follows equation (3-3) [72]:

$$E_G(x) = 0.7x + 3.42(1-x) - 1.43x(1-x) \tag{3-3}$$

Fig. 3-18 is a plot of the $In_xGa_{1-x}N$ bandgap energy/wavelength as a function of the mole fraction of In. Also contained in Fig. 3-18 is a magnified view of InGaN bandgap energy for In fractions between 5 – 20% with a box representing the range (405 -475 nm) of highly efficient commercial LEDs. As seen in the Fig. 3-18, the overlap of commercial wavelengths with In fraction for above-bandgap excitation occurs between 8 – 20% In fraction. In this work, the target was to grow Er-doped InGaN epilayers within this range, and determine the mole fraction with the highest Er emission efficiency.

While growth of high quality GaN is now commonplace among MOCVD scientists, InGaN with high In fractions is still under heavy investigation. Due to the much lower bonding energy between In and N [5], T_G for InGaN must be much lower (~ 200 – 300 C) than that of GaN. At low T_G, the crystalline quality and surface is slightly degraded, and dislocations are

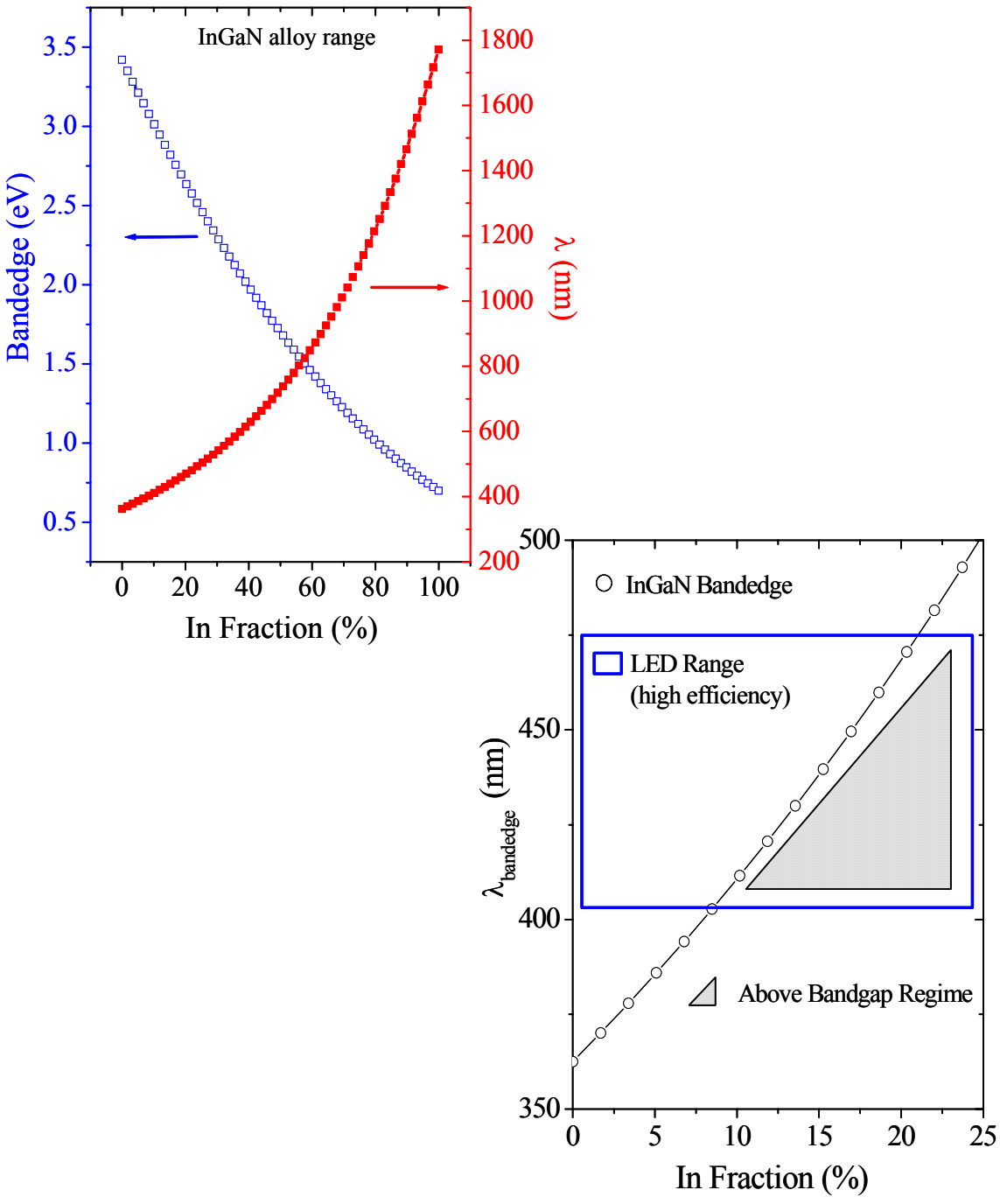

Figure 3-18 (upper right) Plot of bandedge energy/ bandedge wavelength ($\lambda_{bandedge}$) as a function of In fraction using the equation: E(x) = 0.7x +3.42(1-x)-1.43x(1-x). (lower left) Plot of $\lambda_{bandedge}$ for an In fraction of 0 – 25 %. The box represents the range for commercial LEDs with high efficiency, and the shaded area represents the region which corresponds to a wavelength of above-bandgap energy for the corresponding In fraction.

readily incorporated into the epilayer when growing on GaN due to the lattice mismatch between the layers. High In fraction epilayers must also be grown using large In/Ga precursor ratios, large V/III ratios, and at slow growth rates. As will be discussed at length below, these drastic changes in growth environments from GaN are complex obstacles for the growth of highly efficient Er-doped InGaN materials.

The Er-doped InGaN sample structure used for this work was very similar to the previously studied Er-doped GaN. The epilayers were grown on the same (0001) sapphire substrates from Honeywell Electronics, and the substrate preparation followed the same procedure as that of Er-doped GaN. The growth of these epilayers began with the same thin GaN buffer layer and 1.2 μm GaN template layer as in the Er-doped GaN epilayers, followed by a 300 nm Er-doped InGaN layer. The InGaN layer was grown at pressures between 10 and 50 torrs. The In fraction of the Er-doped InGaN epilayers was determined from the peak diffraction angle of è-2è XRD scans. The FWHM of XRD rocking curve for the (002) plane was utilized to determine the crystalline ordering. The optical properties were determined using the same PL system used for Er-doped GaN.

Fig. 3-19 is a θ-2θ XRD scan of Er-doped InGaN grown in the same growth conditions (NH3 flux, PG, etc.) as that of Er-doped GaN but at T_G = 760 C (T_G = 1040 C for Er-doped GaN). Clear peaks are seen at 34.36 and 34.52 degrees corresponding to the (002) diffraction peak of $In_{0.05}Ga_{0.95}N$ and GaN, respectively. The inset (top) of Fig. 3-19 contains 10 x 10 μm AFM images of Er-doped $In_{0.05}Ga_{0.95}N$ and GaN, as well as a block diagram of the epilayer structure. The root mean square deviation of the z-height of Er-doped $In_{0.05}Ga_{0.95}N$ is higher (4 nm) than that of Er-doped GaN (2 nm). The other inset (lower right) of Fig. 3-19 contains a comparison of the (002) XRD rocking curves of Er-doped $In_{0.05}Ga_{0.95}N$ and GaN. The FWHM for both samples is nearly identical indicating that the crystalline quality of Er-doped $In_{0.05}Ga_{0.95}N$ is nearly identical to that of Er-doped GaN.

Fig 3-20 is a comparison of the PL spectra measured at 300 K for Er-doped $In_{0.05}Ga_{0.95}N$ and GaN for λ_{exc} = 263 nm. Fig. 3-20 shows that the PL emission intensity at 1.54 μm is ~ 16 x smaller in the $In_{0.05}Ga_{0.95}N$ than that in GaN. This dramatic decrease in PL intensity is attributed to the lower TG for the InGaN layer. As was determined in the study of Er-doped GaN, the high formation energy value of the Er emitting centers(~ 1.82 eV) demands that high T_G be employed to incorporate large concentrations. We can also expect that the formation energy of the Er

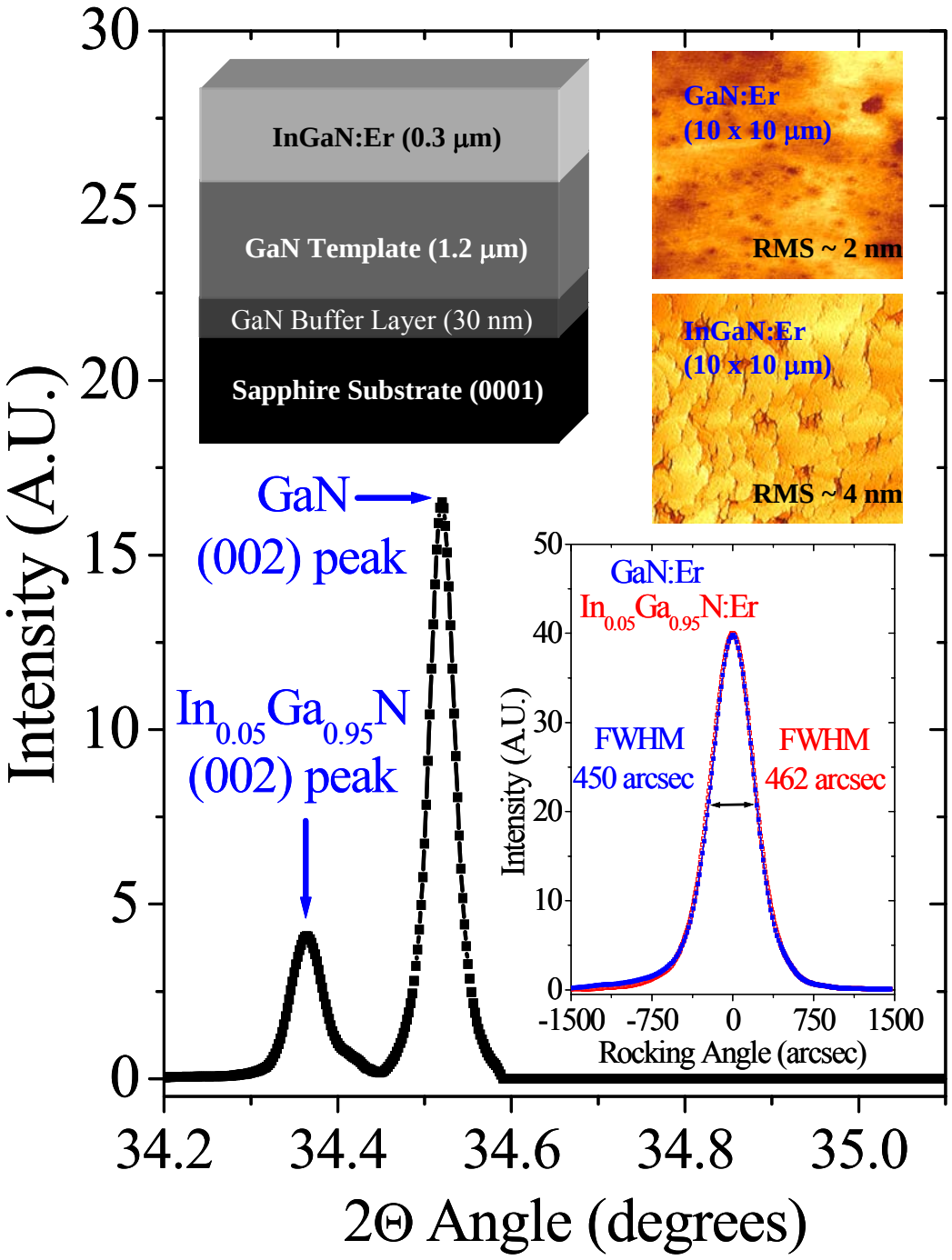

Figure 3-19 XRD θ-2θ spectra for Er-doped $In_{0.05}Ga_{0.95}N$ grown on a GaN template. The lower right inset is a comparison of the rocking curve of the (002) peak for Er-doped $In_{0.05}Ga_{0.95}N$ and Er-doped GaN. The colored images are AFM (10 x 10 μm) images for Er-doped $In_{0.05}Ga_{0.95}N$ and Er-doped GaN. The block structure identifies the layers in Er-doped InGaN used for this work

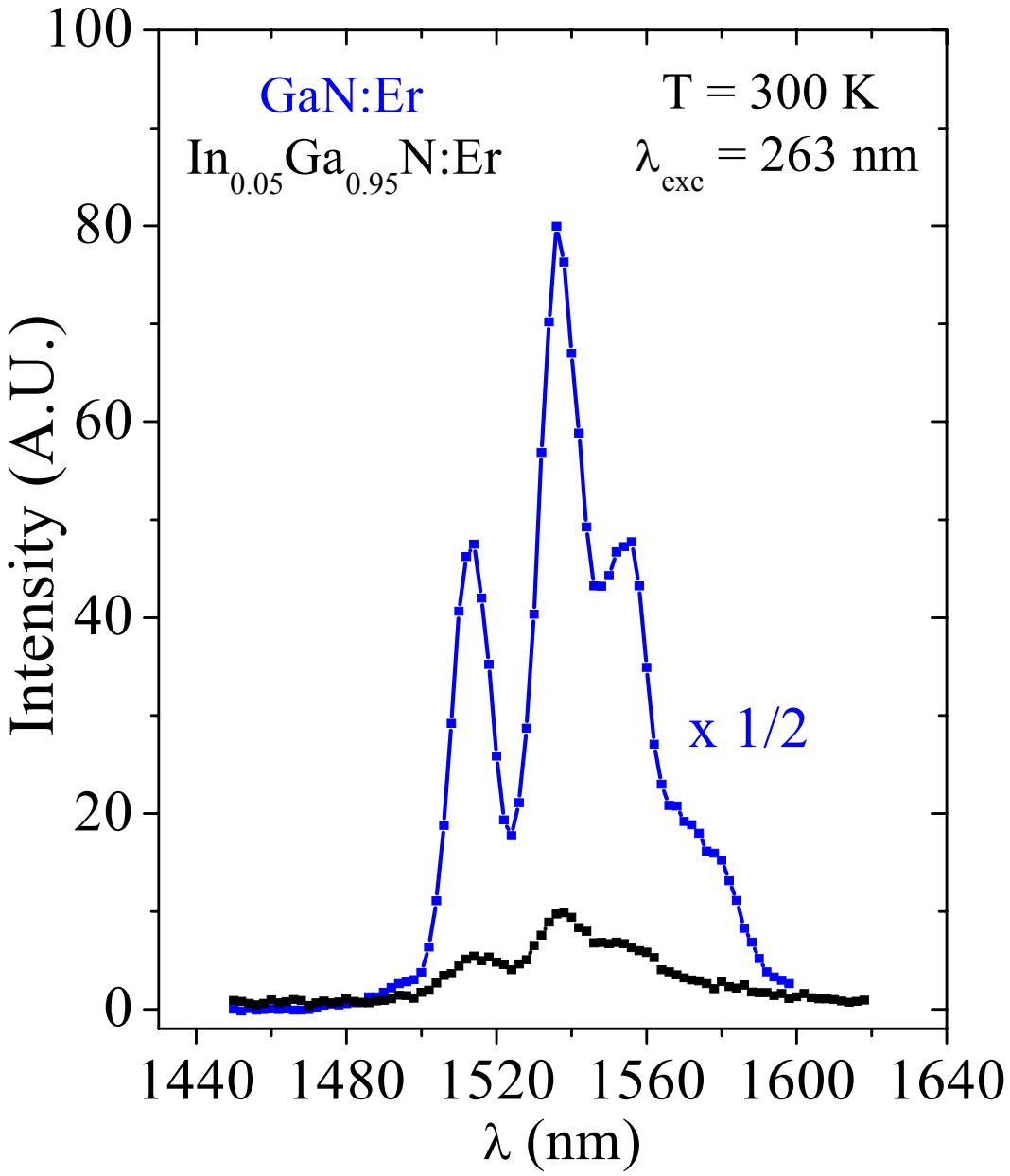

Figure 3-20 PL spectra measured at 300 K of Er-doped $In_{0.05}Ga_{0.95}N$ and Er-doped GaN for λ_{exc} = 263 nm.

emitting centers in $In_{0.05}Ga_{0.95}N$ to be slightly smaller than that of GaN. Equation (3-4) gives the estimated change in Er emitting centers between Er-doped $In_{0.05}Ga_{0.95}N$ and Er-doped GaN.

$$\frac{e^{-E_F(GaN)/kT_{GaN}}}{e^{-E_F(InGaN)/kT_{InGaN}}} \tag{3-4}$$

where k is Boltzmann's constant, E_F(GaN) is the formation energy of the Er-emitting centers in GaN, T_{GaN} is the growth temperature of GaN, E_F(InGaN) is the formation energy of the Er-emitting centers in InGaN, and T_{InGaN} is the growth temperature of InGaN. Since the change in formation energy between $In_{0.05}Ga_{0.95}N$ and GaN is small, we can expect a decrease in the number of Er emitting centers for the InGaN layer by a factor of ~ 28, which is within a factor of 2 compared to the decrease in PL intensity plotted in Fig. 3-20. Thus, the drop in PL intensity at 1.54 μm can in large part be attributed to the fact that much fewer Er centers are implemented into Er-doped $In_{0.05}Ga_{0.95}N$ because of the much lower T_G.

The low growth temperature required for InGaN and high formation energy for the Er emitting centers has proven to be the most challenging obstacle to overcome for this work. In order to increase the 1.54 μm PL emission intensity in Er-doped InGaN, the previous data suggests that the epilayer be grown at much higher growth temperatures, or increase the In mole fraction so as to decrease the formation energy of the Er emitting centers. However, as discussed below, problems other than the high formation energy affect the PL emission.

It is possible to increase the In fraction in the alloy at a constant growth temperature by employing slower growth rates, larger growth pressures, and larger NH_3 fluxes. Thus, Er-doped InGaN epilayers with varying growth rates, growth pressures, and NH_3 fluxes were grown in hopes to optimize both the Er emission and In mole fraction without disturbing the growth temperature.

Fig 3-21 (upper left) is the XRD rocking curve of the (002) peak of Er-doped InGaN for P_G = 10, 20, and 50 torrs. Also contained in Fig. 3-21 (lower right) is the In fraction of Er-doped InGaN for the same P_G, while the inset (lower right) is the FWHM of the (002) rocking curve as a function of P_G. As P_G increases, the In fraction increases from 5% to 16%. The increase in In fraction is most likely a result of the larger sticking coefficient for In at higher pressures, as predicted by Henry's law. The FHWM of the (002) rocking curve also increases with increasing In mole fraction mostly in part due to the larger lattice mismatch between the InGaN and the underlying GaN.

Fig. 3-22 is the IR PL spectra measured at 300 K of Er-doped InGaN for λ_{exc} = 263 nm for P_G = 10, 20, and 50 torrs. The inset to Fig. 3-22 is a plot of the integrated intensity of the 1.54 μm PL emission as a function of In fraction for the samples of different P_G. Although the In fraction increased as desired, Fig. 3-22 clearly shows a drop in PL intensity for increasing P_G. The nature of the decrease in PL intensity at 1.54 μm is still not yet completely understood. The decrease in PL intensity at 1.54 μm is in part due to the fact that the gas phase concentration of the Er precursor decreases with an increasing P_G as detailed in the doping line configuration of the Er system for this MOCVD machine. The decrease in PL intensity may also be a result of the increase in adduct formation between the Er precursor and NH_3 with increasing P_G, in combination with a slight decrease in crystalline quality as evident from the increasing FWHM of the (002) rocking curve for increasing P_G. As the In fraction increases, we also expect the dislocation density to increase, leading to an increase in non-radiative recombination centers.

In continuing attempts to increase the In fraction without decreasing the growth temperature, several Er-doped InGaN epilayers with different NH_3 flow rates were grown. Fig 3-23 (upper left) is the XRD rocking curve of the (002) peak of Er-doped InGaN for NH_3 flow rates of 0.4, 0.8, 1.6, and 2.4 l/min. Also contained in Fig. 3-23 (lower right) is the In fraction of Er-doped InGaN for the same samples, while the inset (lower right) is the FWHM of the (002) XRD rocking curves as a function of NH_3 flow rate. Clearly shown in Fig. 3-23 is an increasing In fraction and decreasing FWHM for increasing NH_3 flow rates. The increase in In fraction with increasing NH_3 flow can be attributed to the increase of available atomic nitrogen. As the NH_3 flow rate increases, more NH_3 is available for decomposition into atomic nitrogen allowing for more In to incorporate into the epilayer. Although the decrease in FWHM of the (002) rocking curve is still not completely understood, it is speculated to be a result of a reduction in nitrogen vacancies due to the increased NH_3 flow rate.

Fig. 3-24 is the IR PL spectra of Er-doped InGaN measured at 300 K for λ_{exc} = 263 nm and NH_3 flow rates of 0.4, 0.8, 1.6, and 2.4 l/min. The inset to Fig. 3-24 is a plot of the integrated intensity of the 1.54 μm PL emission as a function of In fraction for the samples of different NH_3 flow rates. Again, the PL intensity at 1.54 μm decreases with an increasing NH_3 flow rate, and subsequently, an increasing In fraction. The decrease in PL intensity for increasing NH_3 flow is again in part attributed to an increase in dislocation density resulting from the increased In fraction

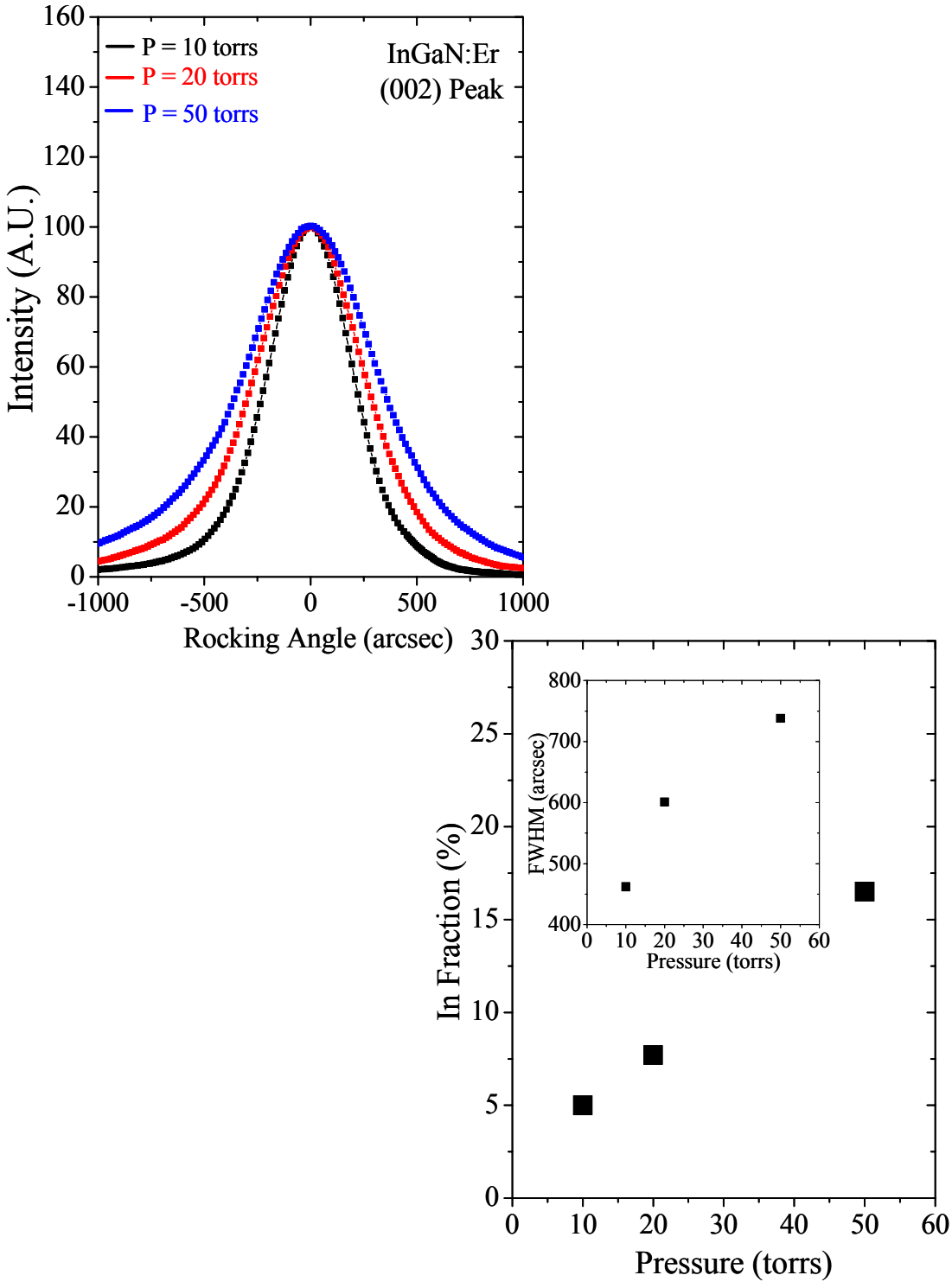

Figure 3-21 (upper left) XRD rocking curve of Er-doped InGaN for P_g = 10, 20, and 50 torrs. (lower right) Plot of In fraction as a function of P_G for Er-doped InGaN. The inset shows the FWHM of the (002) rocking curve as a function of P_G.

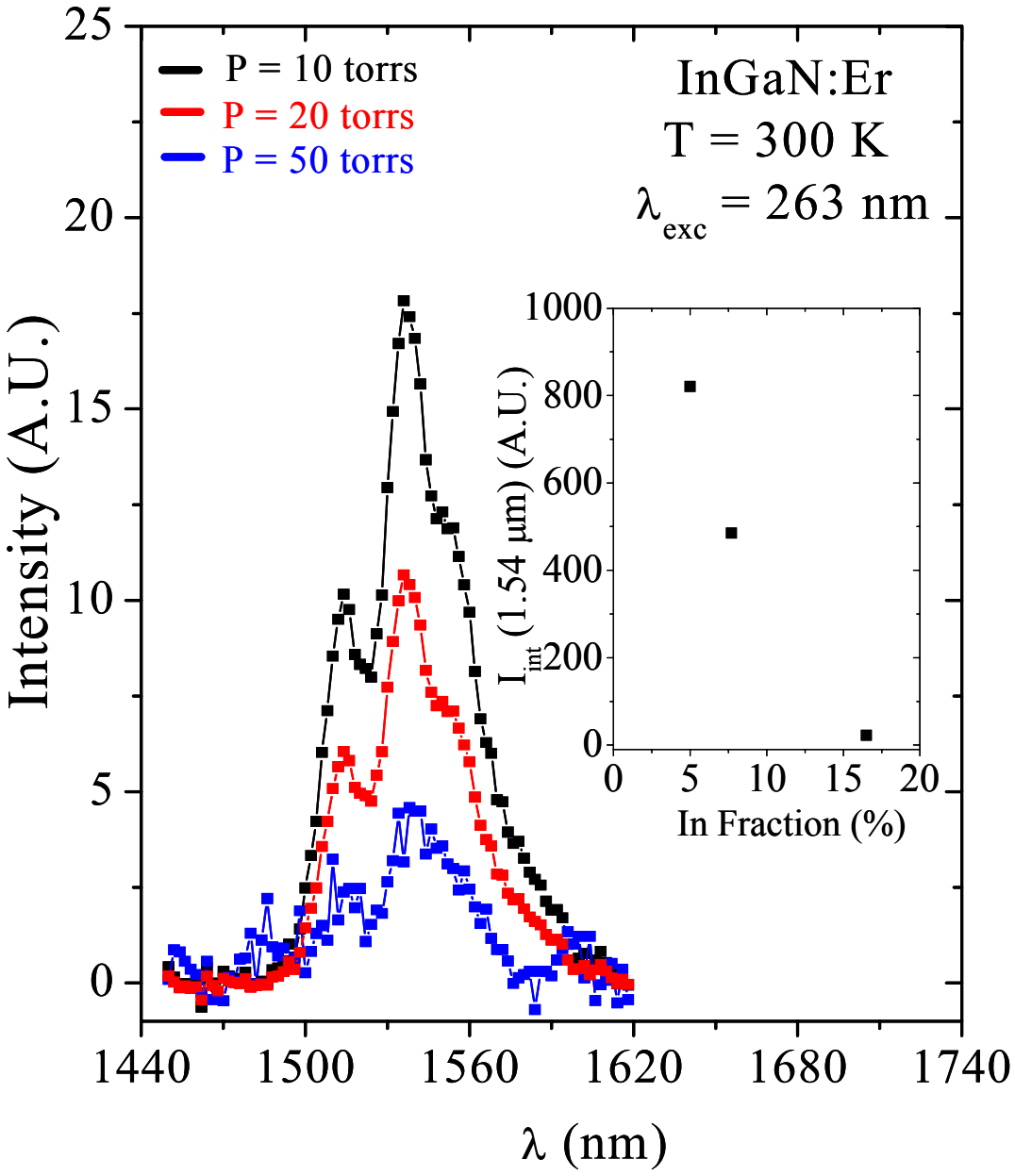

Figure 3-22 PL spectra measured at 300 K of Er-doped InGaN for λ_{exc} = 263 nm for P_G = 10, 20, and 50 torrs. The insert is the integrated intensity of the 1.54 μm PL emission vs. In fraction.

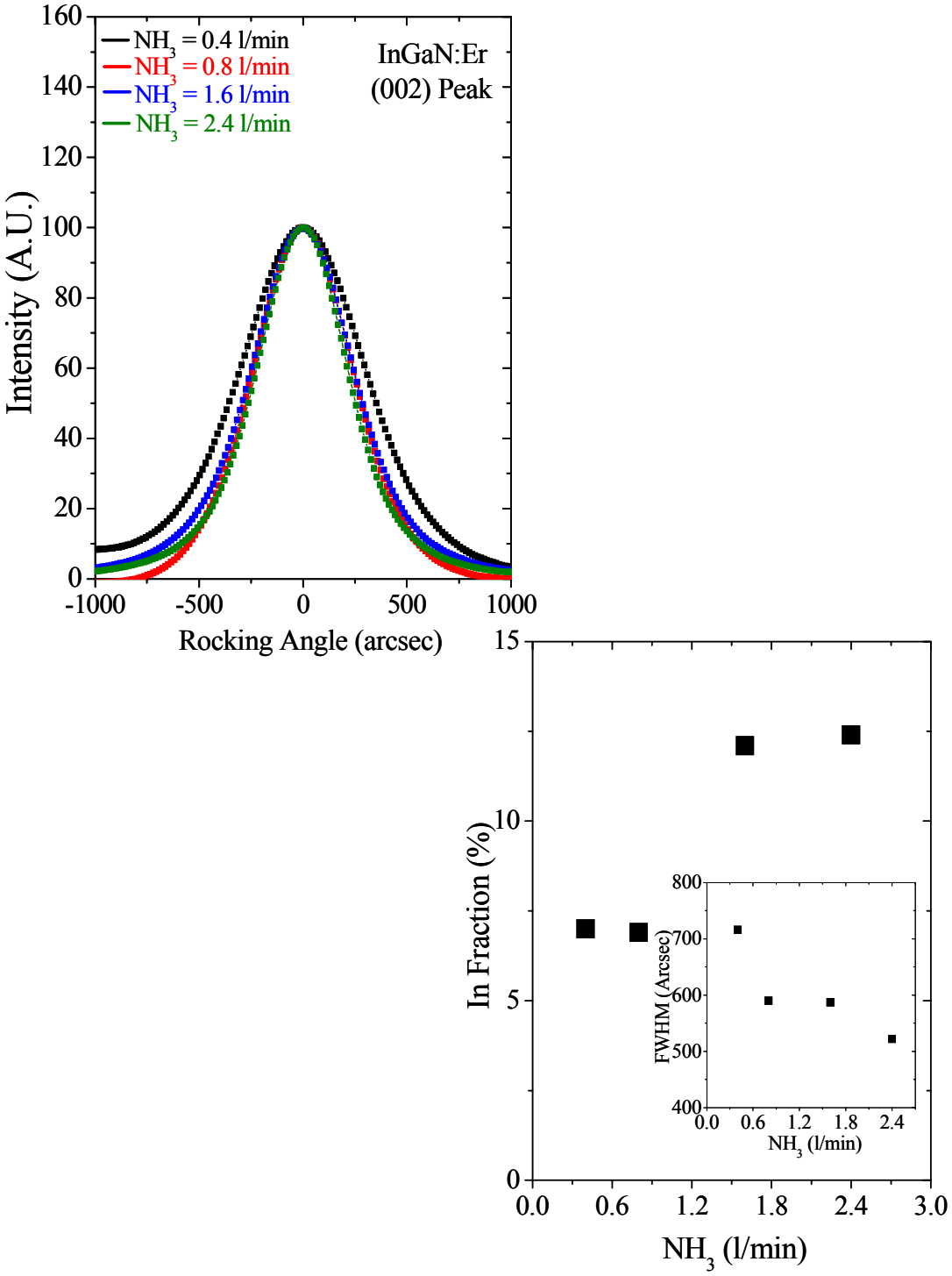

Figure 3-23 (upper left) XRD rocking curve of the (002) peak for Er-doped InGaN for NH_3 flow rates of 0.4, 0.8, 1.6, and 2.4 l/min. (lower right) Plot of In fraction as a function of NH_3 flow rate for Er-doped InGaN. The inset shows the FWHM of the (002) rocking curve as a function of NH_3 flow rate.

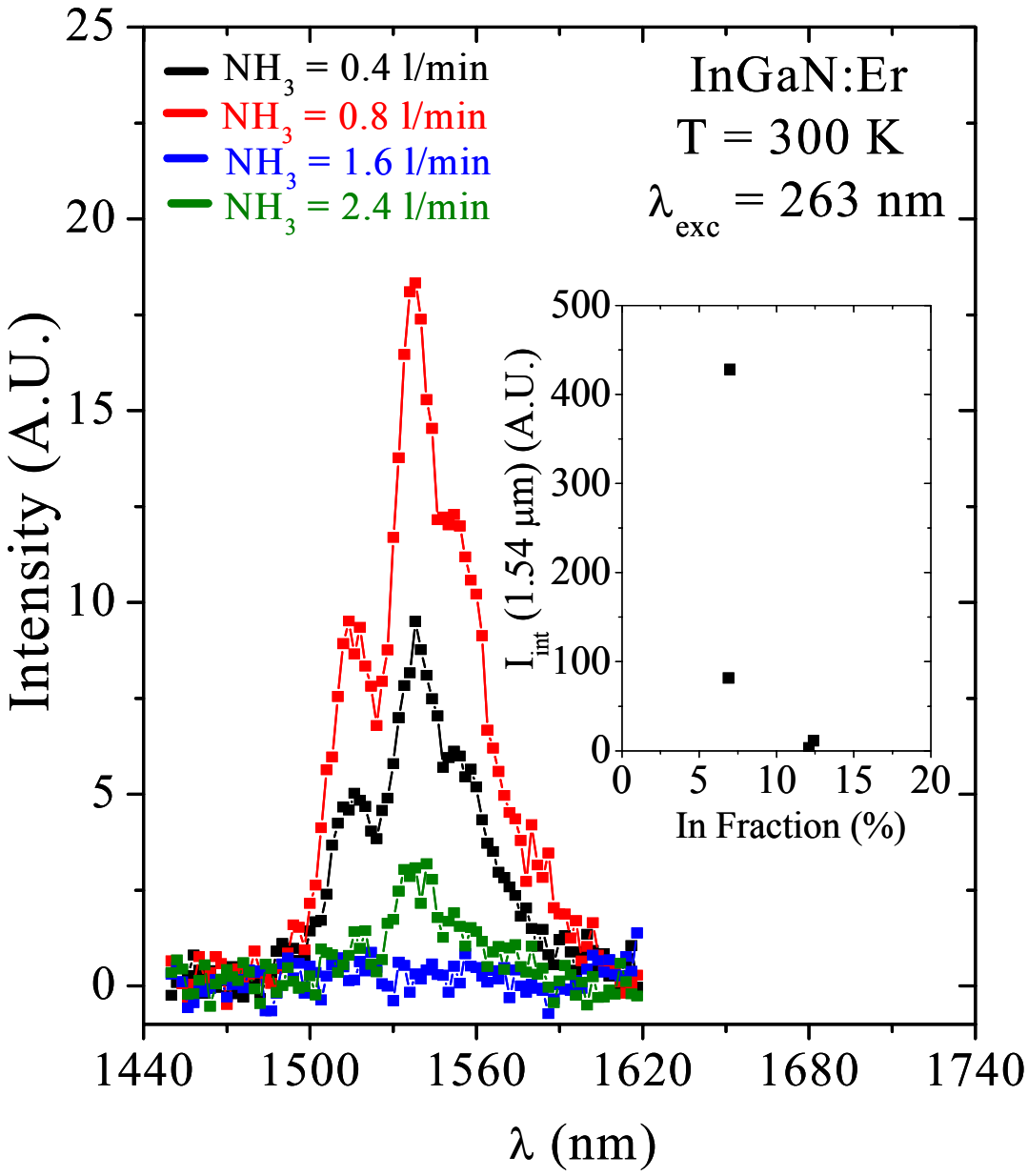

Figure 3-24 PL spectra measured at 300 K of Er-doped InGaN for λ_{exc} = 263 nm for NH_3 flow rates of 0.4, 0.8, 1.6, and 2.4 l/min. The insert is the integrated intensity of the 1.54 μm PL emission vs. In fraction.

Er-doped InGaN samples with varying Ga flow rates were grown as well to increase the In fraction and optimize the PL emission at 1.54 μm. Fig. 3-25 (upper left) is the XRD rocking curve of the (002) peak of Er-doped InGaN for Ga flow rates of 0.3, 0.5, 0.75, and 1.0 ml/min. Also depicted in Fig. 3-25 (lower right) is the In fraction of Er-doped InGaN for the same Ga flow rates, while the inset (lower right) is the FWHM of the (002) rocking curve as a function of Ga flow rate. Fig. 3-25 shows that the In fraction increases with a decreasing Ga flow rate as we expected, and that the FWHM increases with a decreasing Ga flow rate as well. The increase in the FHWM of the (002) rocking curve is again attributed to the larger lattice mismatch between the InGaN and the underlying GaN.

Fig. 3-26 is the IR PL spectra of Er-doped InGaN measured at 300 K for λ_{exc} = 263 nm and Ga flow rates of 0.3, 0.5, 0.75, and 1.0 ml/min. The inset to Fig. 3-26 is a plot of the integrated intensity of the 1.54 μm PL emission as a function of In fraction for the samples of different Ga flow rates. We again incur the same problem with the increasing In mole fraction and PL intensity at 1.54 μm. As the mole fraction increases with decreasing Ga flow rate, the PL intensity decreases. Again, this decrease is attributed to an increase in dislocation density with increasing In fraction in conjunction with a slightly degraded crystalline quality as evident from the increasing FWHM of the (002) rocking curve.

Through an increase in P_G, an increase in NH_3 flow rate, and a decrease in Ga flow rate, we were successful in increasing the In fraction without changing T_G. However, in each case, an increase in In fraction caused a subsequent decrease in the Er based PL intensity at 1.54 μm. We speculate that the decrease in PL intensity results from an increase in dislocation density, a source for non-radiative recombination. As the In fraction increases, the lattice mismatch between the Er-doped InGaN layer and underlying GaN increases, thus leading to an increase in dislocation density. Thus, our preliminary data shows that the mechanism for decrease in PL intensity at 1.54 μm for Er-doped InGaN samples with a larger In fraction is similar to the same mechanism responsible for efficiency reduction in LEDs with active layers with a high In fraction.

Despite the need for further optimization, in the following chapter, these Er-doped InGaN epilayers were applied to novel devices structures, and the subsequent properties and efficiencies of the devices were studied.

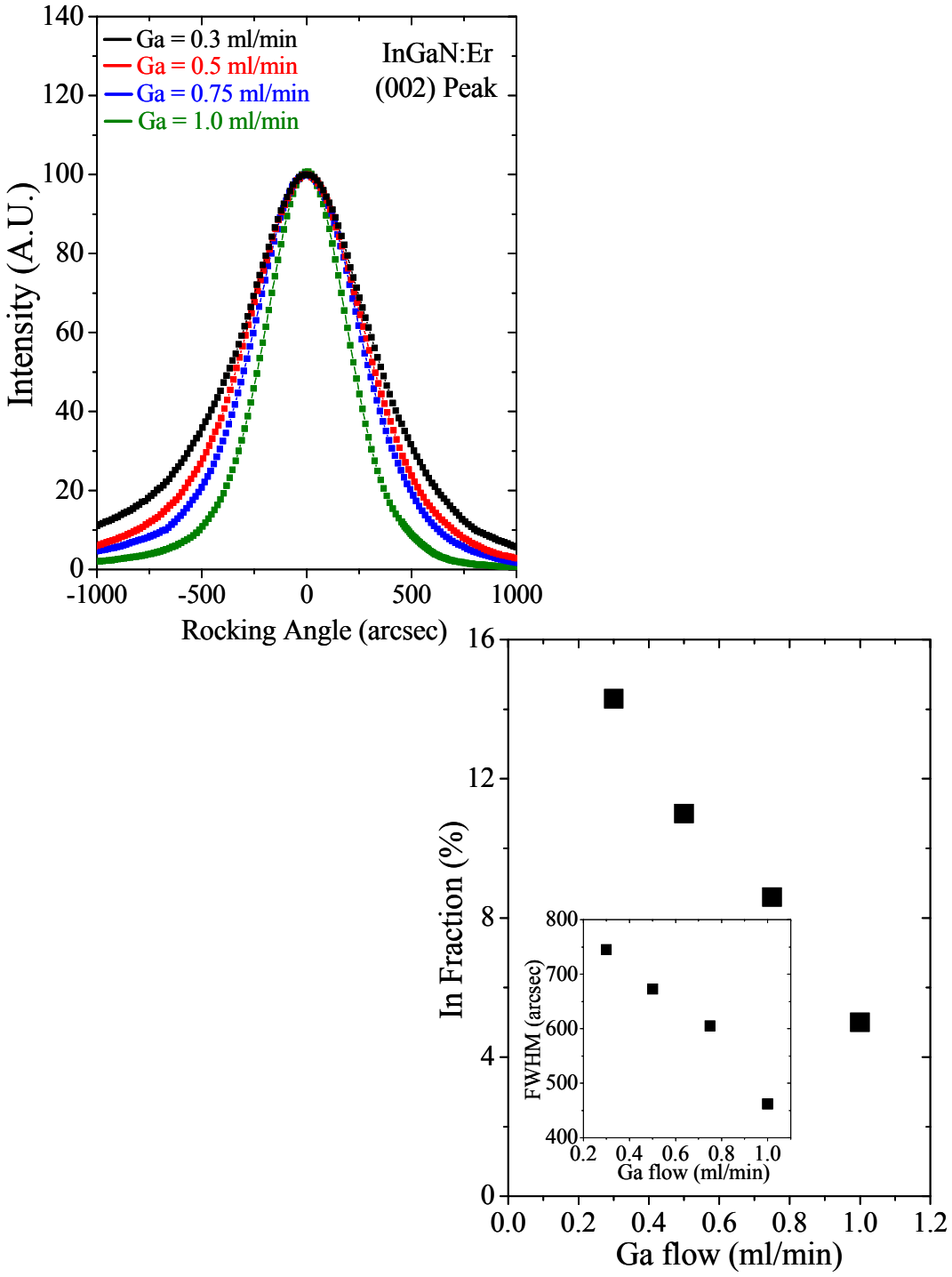

Figure 3-25 (upper left) XRD rocking curve of the (002) peak for Er-doped InGaN for Ga flow rates of 0.3, 0.5, 0.75, and 1.0 ml/min. (lower right) Plot of In fraction as a function of Ga flow rate for Er-doped InGaN. The inset shows the FWHM of the (002) rocking curve as a function of Ga flow rate.

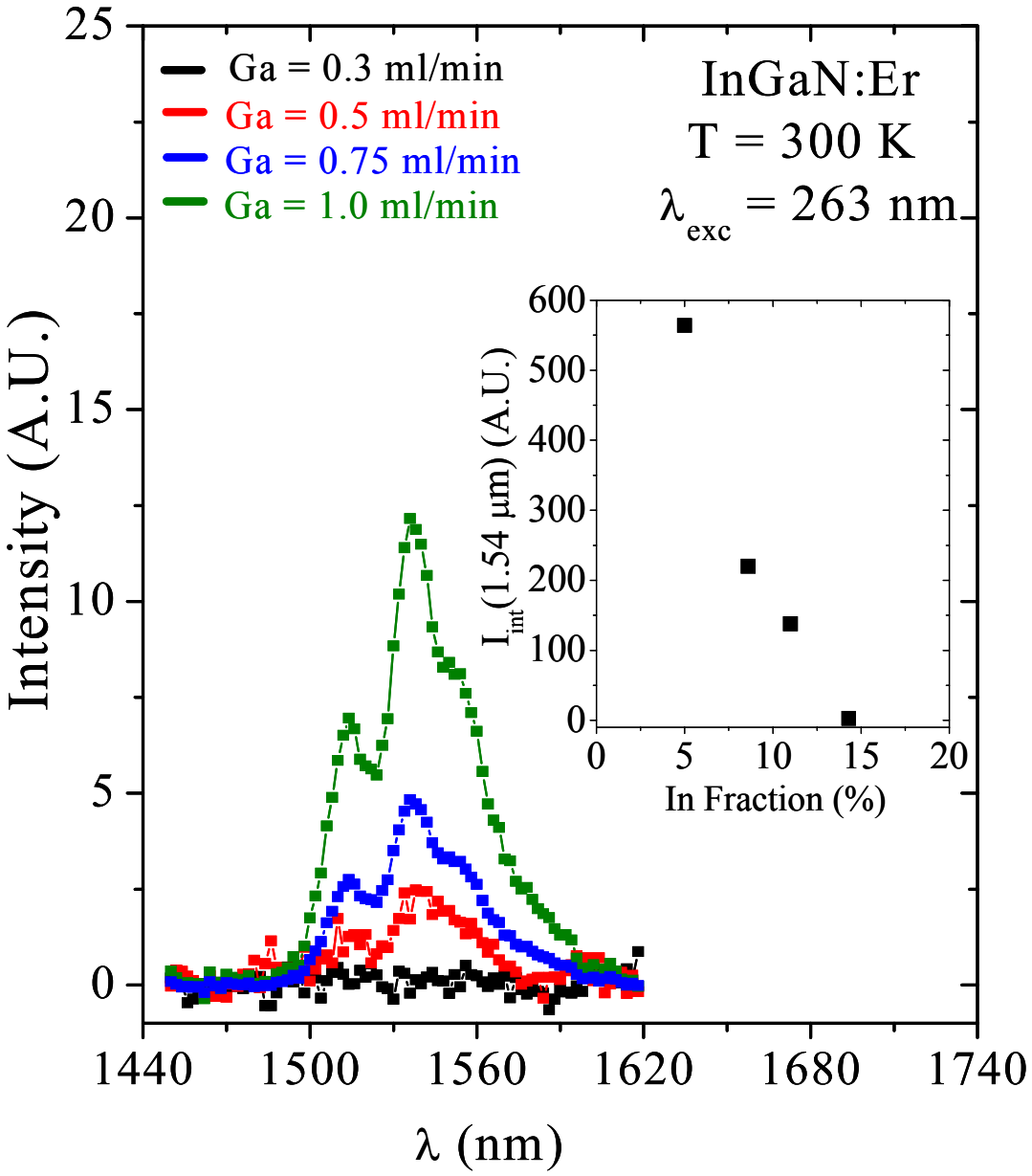

Figure 3-26 PL spectra measured at 300 K of Er-doped InGaN for λ_{exc} = 263 nm for Ga flow rates of 0.3, 0.5, 0.75, and 1.0 ml/min. The insert is the integrated intensity of the 1.54 μm PL emission vs. In fraction.

3.3 Er-doped p-i-n and MQW devices

Successful synthesis and EL emission from Er-doped InGaN/GaN p-i-n diodes was accomplished in this work. As mentioned earlier, EDFA's to date have played a huge role in boosting the telecommunication industries efficiency and capability. EDFAs are a mature technology that utilize the unique optical properties of the 4f shell of Er for high gain applications. However, these systems cannot be used for on-chip integration for next generation networks, operating at faster speeds in a more robust setting, due to inherent physical limitations. The low Er solubility in Silica fibers ($10^{18} – 10^{19}$ cm^{-3}) require that the fibers be meters long in order to attain reasonable gain values (30 dB) [30]. Excitation efficiency of the Er centers is also subpar, requiring high power lasers for sufficient population inversion. Although breakthroughs have been made in making these laser systems more compact, the EDFA's still require elaborate optical components making these devices inapplicable for chip-scale systems. Also, the mechanism of population inversion in EDFA's is optical excitation, thus requiring large laser systems that add to the bulky nature of the final EDFA device size. However, there are no reports of devices that utilize current injection (an excitation method used in semiconductors at chip-scale dimensions) to create population inversion or light emission in Er based devices in an efficient manner. Thus, it is the goal of this section to investigate the optical properties of Er-doped InGaN devices utilizing current-injection excitation. To provide insight to our analysis, detailed below is the theory of optical amplification and spontaneous emission from atomic systems, taken from Yariv's book on Optical Electronics [76].

Although the 4f shell of Er has many different levels, the amplifying or spontaneously emitting system of interest for telecommunication applications can be considered to be a three level system. In this case, the $^4I_{15/2}$ state is the grounds state, the $^4I_{13/2}$ state is the amplifying or spontaneously emitting state, and all other levels are considered pump states. A relevant energy diagram of the 4f shell is depicted in Fig 1-3.

In atomic systems, there are two types of emission that can occur, spontaneous and stimulated. In the case of spontaneous emission (not useful for amplification since the emission is not coherent), electrons are excited from the ground state ($^4I_{15/2}$) into the first excited state ($^4I_{13/2}$) by an external mechanism, and then fall back to the ground state at a rate of $A_{1,2} = 1/\tau$

where τ is the lifetime of the $^4I_{13/2}$ state. The power emitted spontaneously emission from an Er-based emitter is given by equation (3-5):

$$P = N_{Er} E_{1.54\mu m} A_{1,2} \tag{3-5}$$

where N_{Er} is the total number of Er-emitting centers and $E_{1.54\ \mu m}$ is the energy of photons at 1.54 μm. Assuming an Er emitting center concentration of n_{Er}, an active cross section of area A, layer thickness t, and $A_{1,2} = 1/\tau$. The power emitted becomes (3-6):

$$P = \frac{nA}{\tau}\frac{hc}{\lambda}t \tag{3-6}$$

In the case of stimulated emission, electrons are again excited from the ground state to higher states via an external mechanism. In the event that the lifetime of the higher lying states is much shorter than the first excited state, the system approaches population inversion when sufficient excitation is applied. The incoming signal than disturbs the electrons in the first excited state and causes them to transition down to the ground state emitting a coherent photon in the process. For stimulated emission, the rate (power) at which the incoming signal is amplified depends upon both the degree of population inversion and the intensity of the incoming signal. The intensity I_z of a signal traveling along the z-direction of a gain medium is governed by equation (3-7):

$$I_z = I_0 e^{\beta z - \alpha z} \tag{3-7}$$

where β is the gain coefficient of the material, α is the loss coefficient of the material and I_0 is the initial intensity of the incoming signal. For a gain medium with homogeneous broadening (a medium with a single class of amplifying atoms), the gain coefficient for the medium is that of equation (3-8),

$$\beta = \frac{(n_2 - n_1)\lambda^4}{8\pi n^2 \tau_{sp} c \Delta\lambda} \tag{3-8}$$

where n_2 is the concentration of Er atoms in first excited state, n_1 is the concentration of Er atoms in the ground state, λ is the wavelength of the incoming signal, n is the refractive index of the material for the signal wavelength, c is the seed of light, $\Delta\lambda$ is the FWHM of the gain spectrum, and τ_{sp} is the spontaneous lifetime of the first excited state. For Er-doped GaN, n = 2.335, $\Delta\lambda$ ~10 nm, τ_{sp} is on the order of 1 ms [29] , and λ = 1550 nm. Assuming complete population inversion, that all Er atoms determined from the SIMS analysis are active Er-emitting centers, the difference in Er concentration between Er-doped InGaN and Er-doped GaN according to Boltzmann statistics, and 0 waveguide loss (i.e. $\alpha = 0$) ($n_2 - n_1 = n_{Er} = 1.3 \times 10^{19}$ cm^{-3}), the β value

of our cavity is ~ 1.8 cm^{-1}. In order to attain a 30 dB signal enhancement, a cavity length of 3.9 cm would suffice. Although this cavity length is determined using the best case scenario, this first order calculation shows the possibilities for Er-doped GaN as a next-generation gain medium for the c-band of the telecommunication spectrum.

Although the β value determines the possible gain achievable inside the gain medium, in order for the Er-doped InGaN system to be an efficient amplifier medium, it must be able to achieve population inversion at reasonable pump powers. The signal and amplified light must also remain in the medium, so the cavity must be shaped into a waveguide. For materials such as Er-doped GaN, the most fitting waveguide is a two dimensional waveguide (cladding layer and core layer) with the core layer also being the gain medium. In order for the signal to pass through the waveguide without reasonable losses, the dimensions of the waveguide must be on the order of the signal wavelength. Otherwise, huge scattering losses occur severely limiting the amplified signal output. In our case, since the incoming signal is around 1.5 μm, the core layer must be of the order of 1.5 μm as well. The rate of stimulated emission also depends upon the cavity size through the dependence upon the signal intensity. Since the rate of stimulated emission depend upon the incoming signal intensity, waveguides with incorrect dimensions will reduce the signal intensity and decrease the stimulated emission.

The previous chapters have outlined that Er-doped GaN and InGaN may have the appropriate properties to be effective amplifier mediums. It was also shown above that properties of these materials matched with amplifier theory predicts that these materials may be exciting alternatives for new-age telecommunication platforms. And although the final goal is to produce chip-scale amplifiers based upon Er-doped InGaN materials, achieving and characterizing the spontaneous emission from Er-doped InGaN devices is an important intermediate step before reaching the final product. As will be shown below, we have successfully synthesized Er-doped p-i-n diodes that show a strong 1.54 μm spontaneous emission under forwards bias. Our results also show that the dominant EL emission from these diodes is at 1.54 μm, making these materials even more attractive for telecommunication applications.

The device structures used for this work were p-i-n diodes for which the i-layer was doped with Er. The device structures are depicted in Fig. 3-27, and the possible excitation mechanisms for these devices are also depicted in Fig. 3-27. The p-i-n diodes were grown on the same (0001) sapphire substrates used for the Er-doped GaN and InGaN epilayer study, and they were

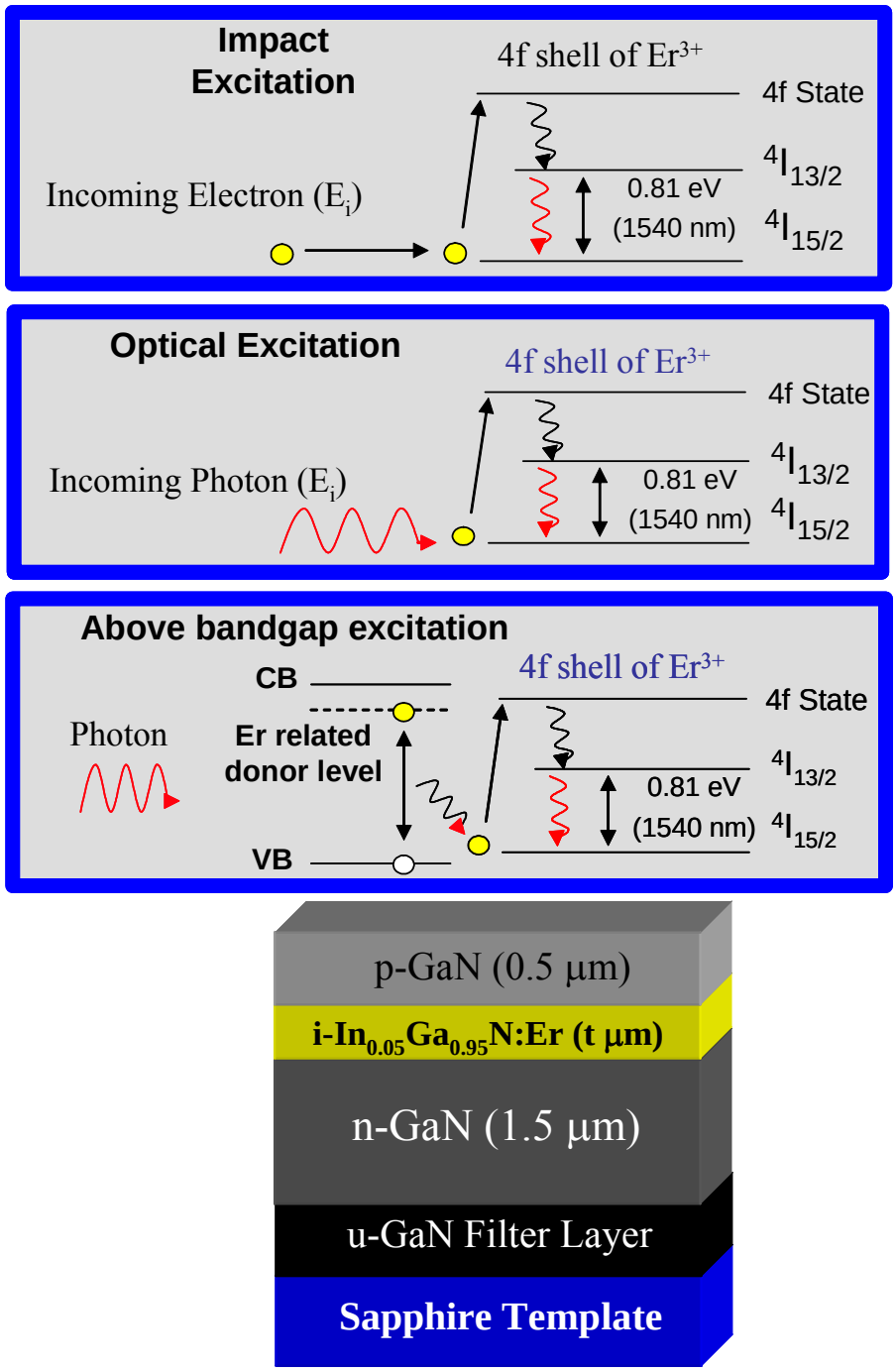

Figure 3-27 (Top) Possible excitation mechanisms in Er-doped InGaN/GaN p-i-n diode devices. (Bottom) Block representation of the layers of Er-doped InGaN/GaN p-i-n diode devices used for this work.

prepared for growth in the same manner. Growth of the p-i-n diodes began with a thin GaN buffer layer, followed by a 0.6 μm undoped GaN filter layer grown at 1040 C. A 1.5 μm thick Si doped GaN layer was then deposited ($n = 5 \times 10^{18}$ cm^{-3} and $\mu = 250$ cm^2 / V s), followed by a variable thickness Er-doped $In_{0.05}Ga_{0.95}N$ layer and a 0.5 μm Mg-doped GaN layer ($p = 3 \times 10^{17}$ cm^{-3} and $\mu = 10$ cm^2 / V s). The Er concentration in the i-layer is ~ 1.3×10^{19} cm^{-3}. To activate the acceptors in the p-layer, the structures were annealed in a N_2 ambient at 950 C for 14 seconds. XRD θ-2θ scans of the (002) peak were utilized to probe the In fraction and crystalline ordering of the structure, while AFM images profiled the surface morphology. In metal was soldered to the n- and p-layer to create ohmic contacts.

Figure 3-28 is the XRD θ-2θ scan for an Er based p-i-n diode structure, while the inset is the rocking curve of the (002) peak for the Er-doped InGaN i-layer. Fig. 3-28 also shows (10 x 10 μm) AFM images of Er-doped $In_{0.05}Ga_{0.95}N$ and an Er based p-i-n diode. The peaks in Fig. 3-28 at 34.39 ^{o} and 34.59 ^{o} degrees corresponds to the (002) peak of Er-doped $In_{0.05}Ga_{0.95}N$ and GaN, respectively. The full width at half maximum (FWHM) of the (002) rocking curve of the $In_{0.05}Ga_{0.95}N$ layer is 472 arcsec, indicating its high degree of crystalline quality. Fig. 3-28 also shows that the surface of the p-i-n diodes is much rougher than the epilayer, as the RMS deviation of the z-profile is 26 nm for the p-i-n diode compared to 4 nm for the epilayer. The rough surface originates at the interface of the i-layer and the p-layer, and is caused by the drastically different growth environments between the two layers.

Figure 3-29 is the VIS and IR EL spectrum at 300 K of the p-i-n diode under a forward bias of 15 V and 20 mA. In contrast to the PL spectra, emission peaks besides those at 1.0 and 1.54 μm are observed at wavelengths of 418, 536, 557, and 667 nm. These peaks are attributed to the following intra-4f Er transitions; 418 nm ($^2H_{9/2}$), 536 nm ($^2H_{3/2}$ to the $^4I_{15/2}$) , 557 nm ($^2S_{3/2}$ to the $^4I_{15/2}$), 667 nm ($^2S_{3/2}$ to the $^4I_{15/2}$). The appearance of these new emissions peaks imply that the excitation method for the p-i-n diode is different from the PL mechanism. In conjunction with this result, the absence of any bandedge emission implies that the excitation mechanism is due to impact of energetic electrons. These new peaks are also undesirable for telecommunication devices since they reduce possible transitions at 1.54 μm.

Fig. 3-30 is a plot of the 1.54 μm EL emission for p-i-n diodes with i-layer thickness of 50, 100, and 200 nm at a fixed current of 20 mA. The inset to Fig. 3-30 is the I-V curve for the

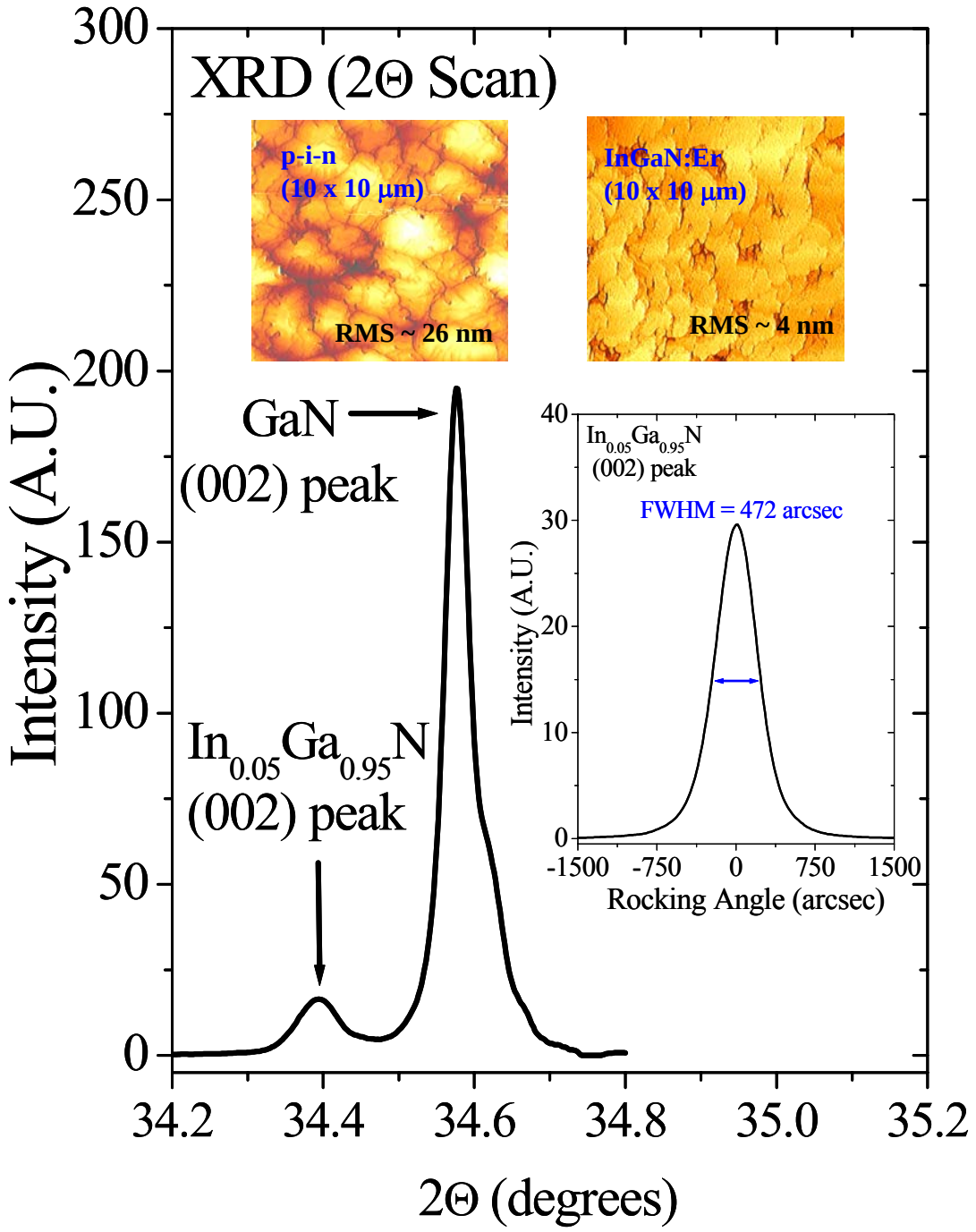

Figure 3-28 XRD θ-2θ diffraction intensity for an Er-doped p-i-n diode. The lower right inset is the rocking curve of the i-layer for the p-i-n diode. The colored images are AFM (10 x 10 μm) images for Er-doped $In_{0.05}Ga_{0.95}N$ and the p-i-n diode.

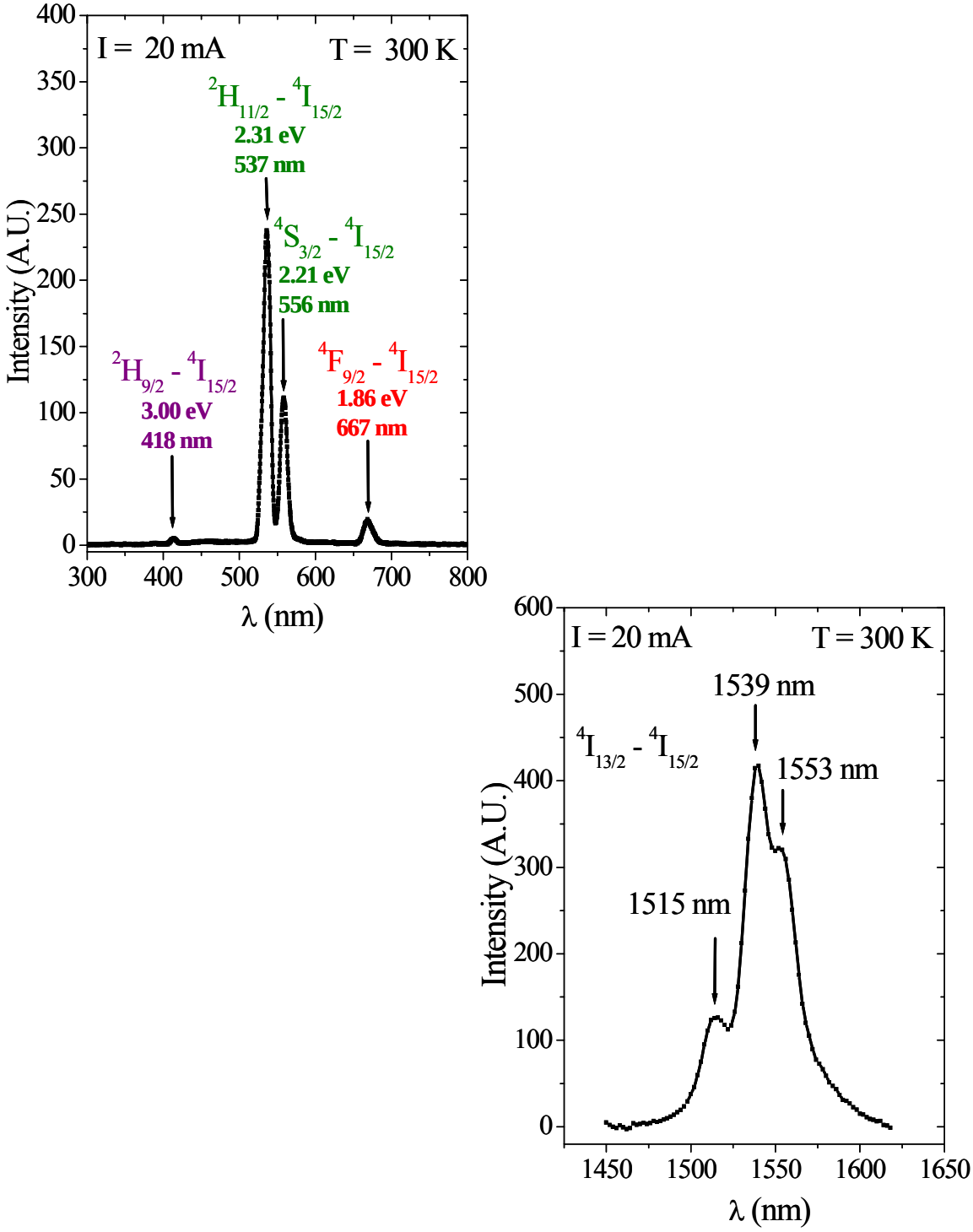

Figure 3-29 (upper left) EL spectra of an Er-doped p-i-n diode in the VIS region measured at 300 K and a current of 20 mA. (lower right) EL spectra of an Er-doped p-i-n diode in the IR region at 300 K and a current of 20 mA.

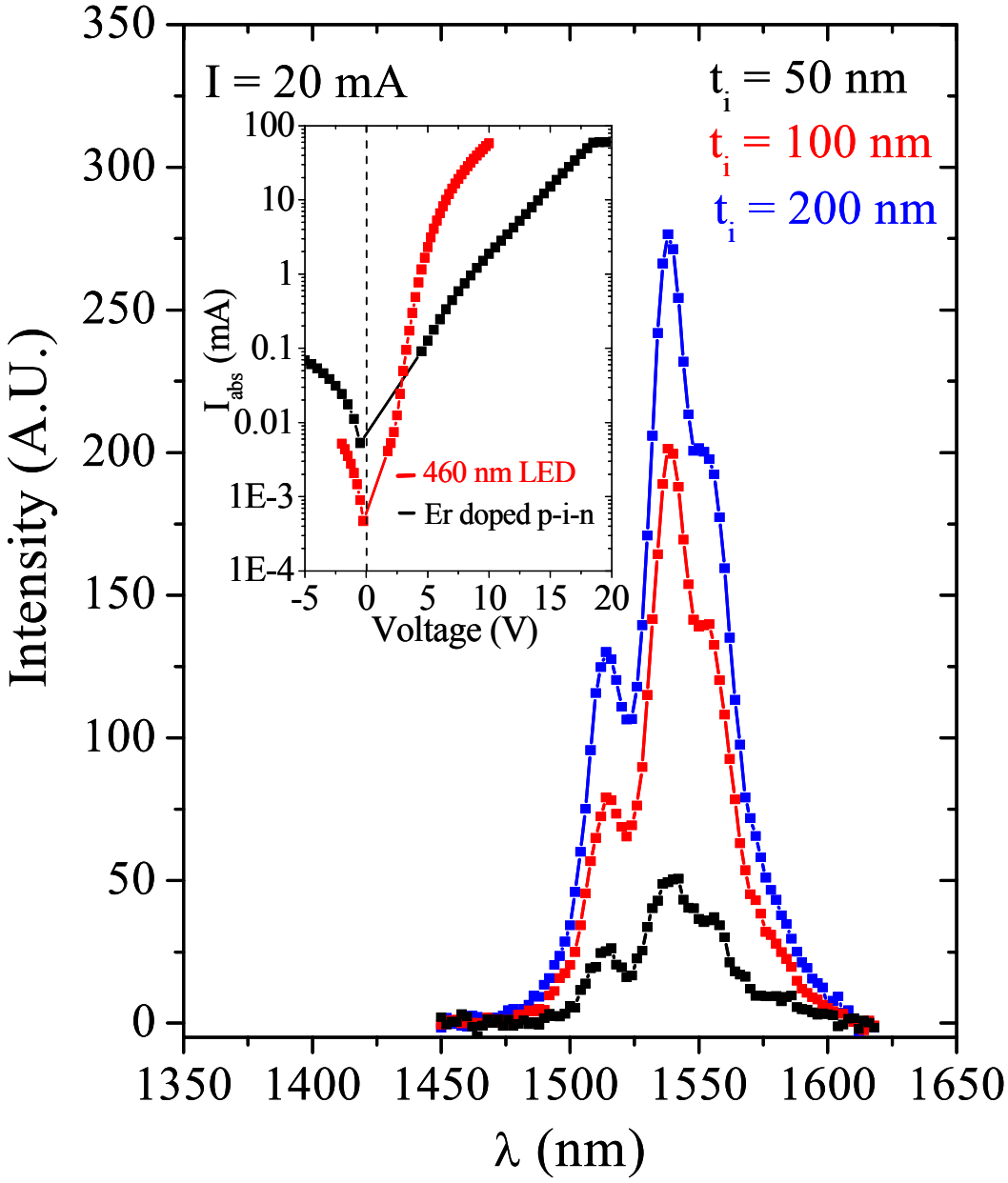

Figure 3-30 EL spectra for Er-doped p-i-n diodes for i-layer thickness of 50, 100, and 200 nm. The inset is a semi-log plot of the I-V curves for an Er-doped p-i-n diode with i-layer thickness of 50 nm compared to a reasonable 460 nm LED grown on the same MOCVD machine.

same samples in a semi-log format in comparison to a p-n junction without any i-layer. It is clearly seen that the EL emission increases linearly with i-layer thickness. Er concentration increases linearly with the i-layer thickness, and thus the EL intensity varies accordingly. However, we also see that the I-V curve changes dramatically for the different thickness of the i - layer. As the i-layer thickness increases, the voltage required to produce 20 mA increases as well. This result implies that the i-layer is highly resistive in nature, and an increase in i-layer thickness will increase the net resistance of the device thus increasing the required bias.

Fig. 3-31 is the L-I curve for the p-i-n diode with 200 nm i-layer thickness for the VIS and IR range. Fig. 3-31 also contains the L-I curve for the total power (VIS plus IR) for the p-i-n diode in comparison to a reasonable blue LED. The power for the combined IR emission is higher than that of the VIS emissions. This is a positive result since it implies that a majority of the emission occurs at the desired 1.54 μm wavelength. Assuming $n_{Er} = 1.3 \times 10^{19}$ cm^{-3} , the maximum power emitted from the diode with an i-layer thickness of 200 nm according to equation (3-6) would be 17 μW. At 20 mA, the internal quantum efficiency is 13.9 %, assuming 100 % of the light generated leaves the diode.

Since we expect the high voltage required for the p-i-n diodes is due to the highly resistive nature of the i-layer, several p-i-n diodes with Si codoping in the i-layer were grown in hopes to reduce the bias of the diode. Fig. 3-32 is a plot of the total power emitted in the VIS region for diodes with different Si flow rates in the i-layer. The inset to Fig. 3-32 is the I-V curve for the same diodes. As the Si flux increases, the bias required for 20 mA decreases, implying that the i-layer becomes more conductive. But, as the Si flux increases, we also see that the total power emitted from the Er layer decreases as well. The smaller voltage produces a smaller electric field in the depletion region, thus leading to fewer carriers with sufficient energy to excite the Er centers. This result is further evidence that the excitation mechanism in the p-i-n diode is caused by impact excitation of energetic carriers with 4f electrons.

Fig. 3-33 is a comparison of the optical microscope images (100 x magnification) of Er based p-i-n diodes of variable i-layer thickness. As can be seen from the figure, the surface of the diode without an i-layer is device grade, whereas the surface with an i-layer thickness of 200 nm has a very rough surface. The roughening of the surface stems from the fact that the interface between the i-layer and p-layer is strained due to the drastically different growth conditions used for these respective layers. In order for this strain to be relieved, more structures

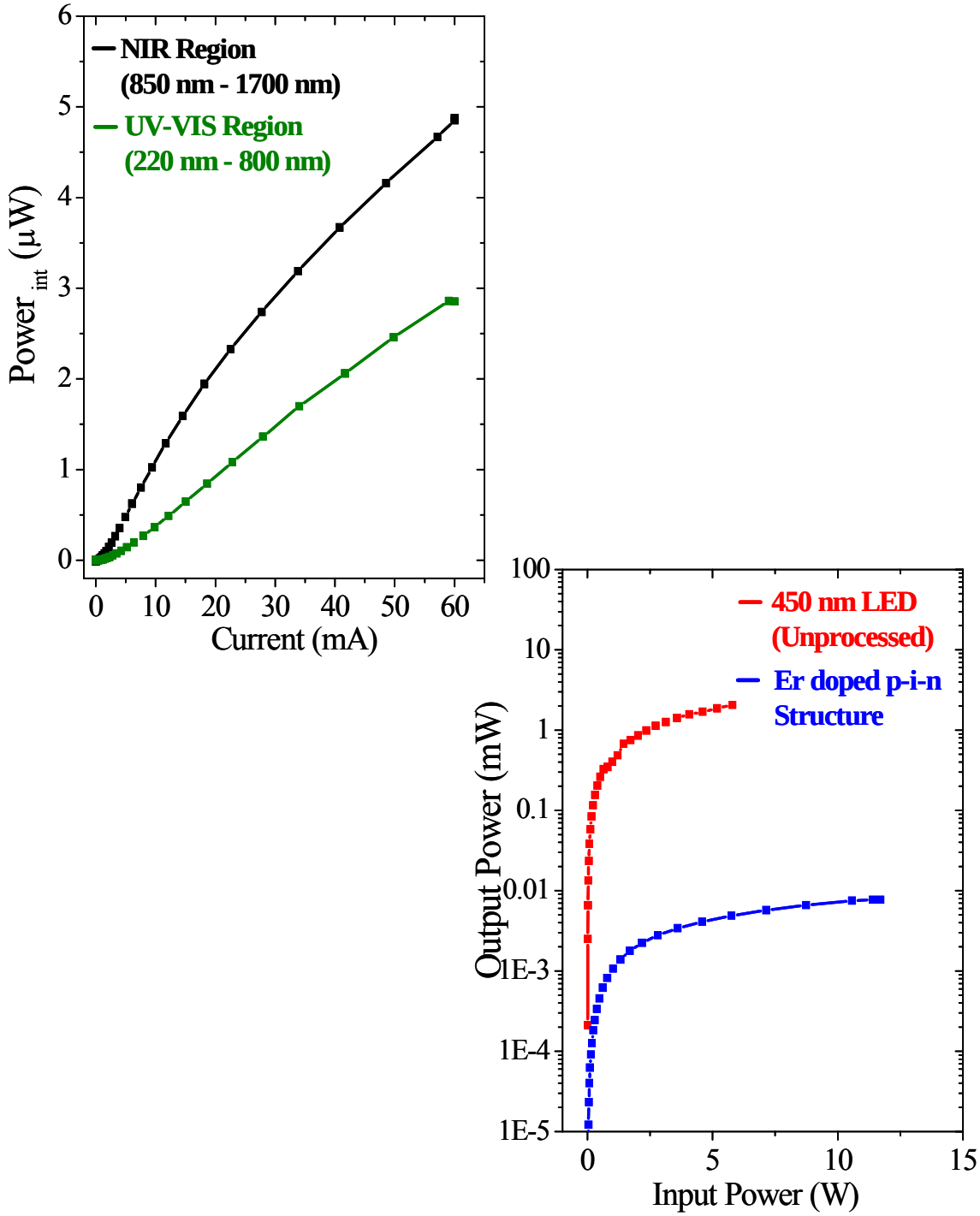

Figure 3-31 (upper left) L-I plot for an Er-doped p-i-n diode for both the VIS (220 – 800 nm) and NIR region (850 – 1700 nm). (lower right) Efficiency plot of p-i-n diode compared to 460 nm LED grown on the same machine.

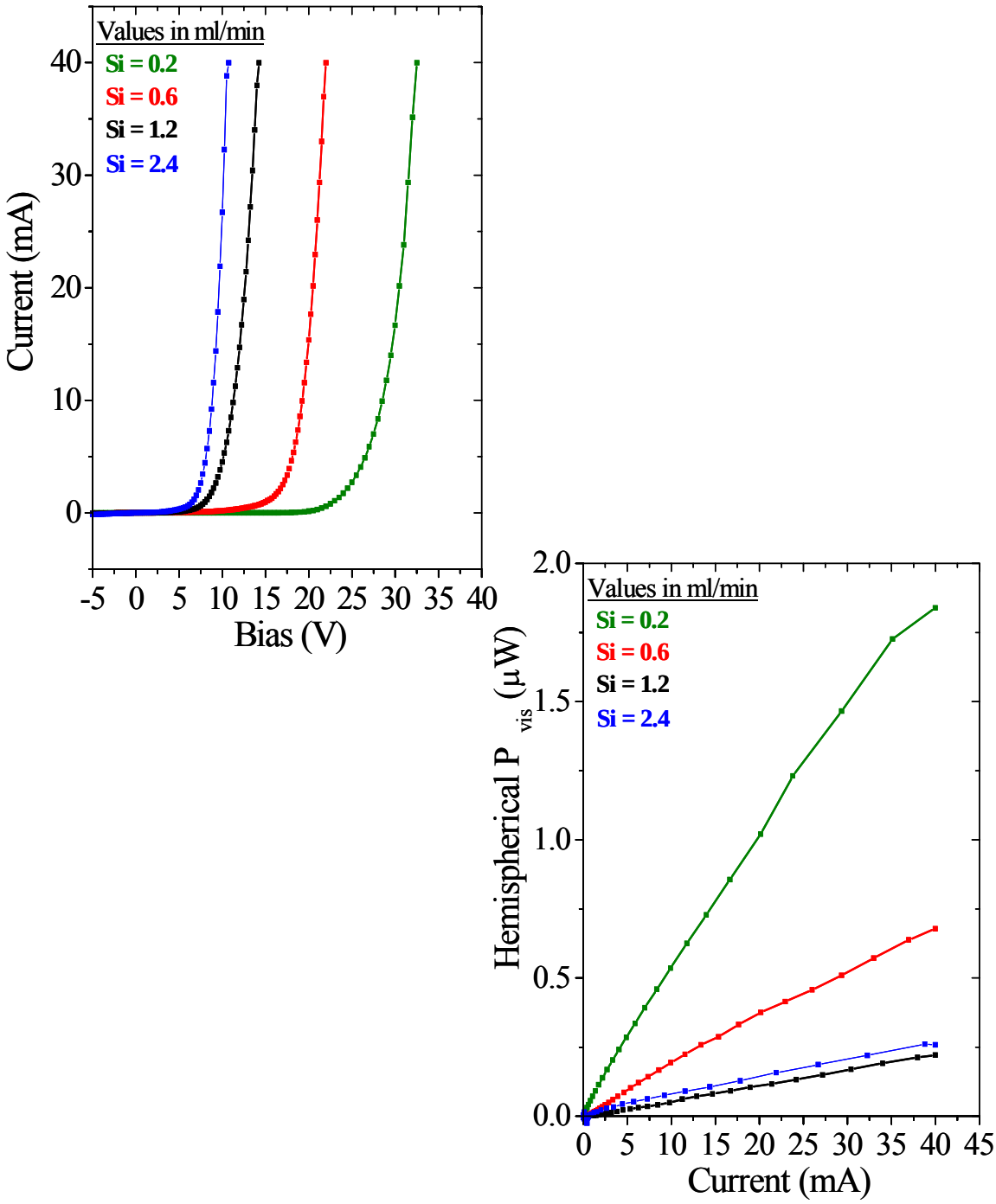

Figure 3-32 (upper left) I-V curve for Er-doped p-i-n diodes codoped with Si for flow rates of 0.2, 0.6, 1.2, and 2.4 ml/min. (lower right) L-I curve for Er-doped p-i-n diodes codoped with Si with flow rates of 0.2, 0.6, 1.2, and 2.4 ml/min. The power in the figure is from the visible region only.

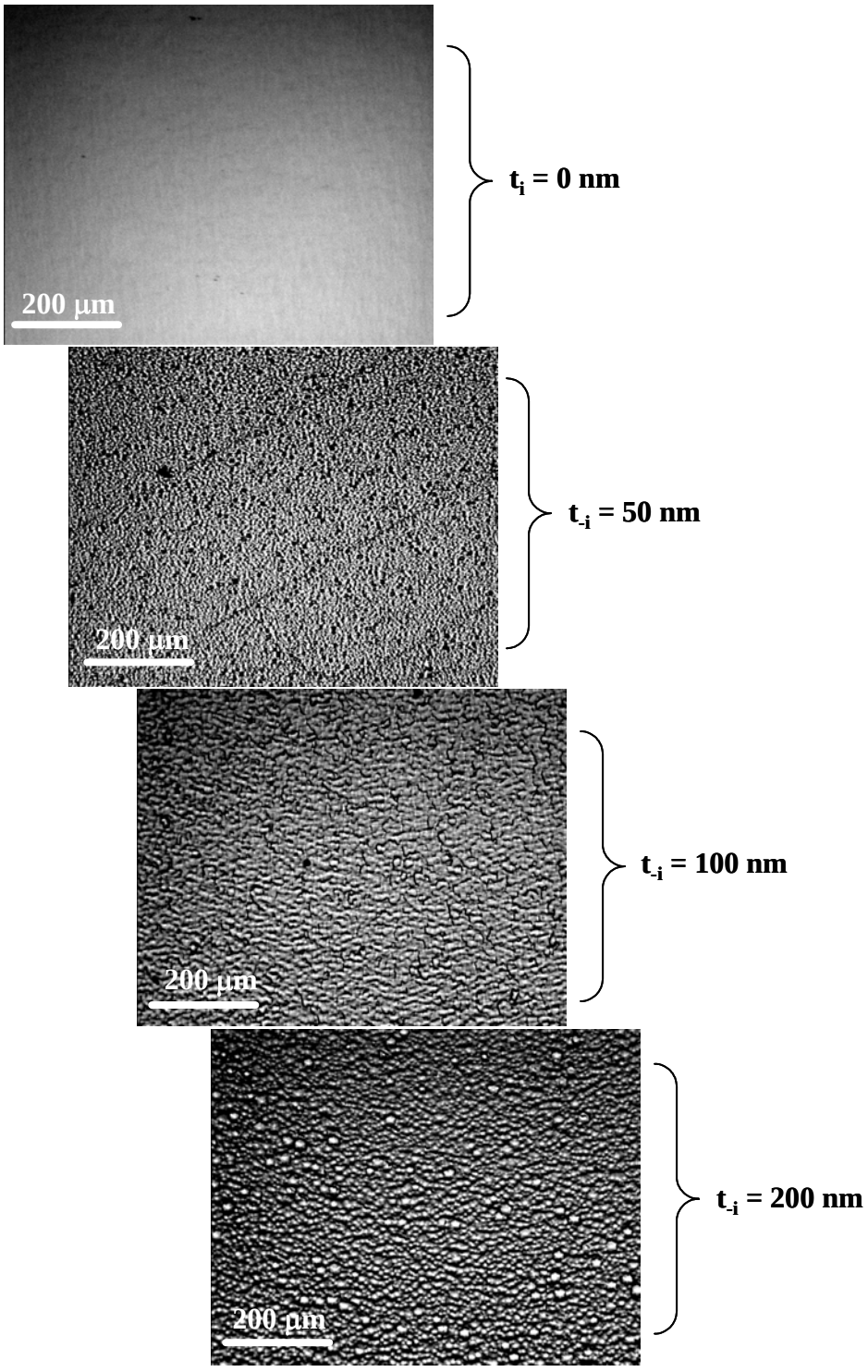

Figure 3-33 Optical microscope images (magnification = 100 x) of Er-doped p-i-n diodes with i-layer thickness of t = 0, 50, 100, and 200 nm.

with graded interface layers must be employed. The fact that the surface roughens so dramatically for such a small thickness is the main limiting factor for the i-layer thickness. Without a flat surface, device processing (methods such as lithography and metal evaporation) is extremely difficult. In conjunction with this problem, p-type conductivity drops dramatically with increasing surface roughness due to compensation of the acceptors via surface defects.

3.4 Limitations with the Er based III-N materials via MOCVD

In this chapter, I will summarize the problems facing the successful, repeatable synthesis of efficient Er based, current injected devices operating at 1.54 μm. As detailed many times throughout this work, MOCVD growth is a multi-variable process. III-nitride materials made via MOCVD often have many different layers (see Fig. 3-1) in order to alleviate stress/strain induced by the growth substrate, or reduce defects/impurities, etc. The MOCVD system also takes great lengths in precursor/transport gas purity and vacuum control (see list in section 3.1) in order to eliminate unwanted elements from entering the epilayer and achieve repeatability of the epilayer. For MOCVD scientists, the common practice in creating materials with highly optimized electrical/optical/structural properties is to vary one growth parameter (NH3 flux, PG, TG, etc.) at a time, layer by layer. Then, after careful analysis of many different runs with variable growth parameters, a trend is observed. The trend is then further investigated, and used as a guideline for future materials growth. These trends can only be determined if the measurement portion is done with a high precision, and the MOCVD can consistently produce the same environment during the epilayer growth. For our lab, the analysis methods are very precise, thus allowing us the ability to accurately profile the as-grown materials.

However, as mentioned in the experimental methods section, drastic modifications to the MOCVD doping method were necessary for this work in order to accommodate the lack-luster Er precursor. Although these modification resulted in the successful synthesis of Er-doped GaN with $n_{Er} = 2 \times 10^{21}$ cm^{-3}, to date, the adaptations resulted in Er-doped epilayers with drastically different growth properties despite the seemingly unchanging growth environment. Thus, optimizing the important properties of the material like the Er PL signature or surface roughness was very difficult since day-to-day growth resulted in different Er doping profiles. It was also noted in the section on Er-doped InGaN, that the PL signal dropped for higher In fraction epilayers independent of the crystalline quality or TG. In an attempt to forecast why these problems occurred, written below is a segmented detail of the possible mechanisms responsible for the aforementioned obstacles and/or misleading results.

3.4.2 Er precursor condensation and contamination

Since the Er precursor vapor pressure at room temperature was far too low for the Er concentrations desired, the Er bubbler was placed in a high temperature bath up to 100 C. Thus,

in order to prevent condensation of that precursor in the 2 m long transport line or the pneumatic valves, a specialized heater tape was attached. However, it was later observed that upon opening the system for maintenance, large deposits of the Er precursor were found at the bubbler output. Fig. 3-34 is a picture of the out valve of the Er bubbler after 1 year of use. The orange and yellow film seen in Fig. 3-34 is the condensation of the Er precursor on the bubbler tubing. This implies that condensation occurred despite the heated doping line. Similar deposits are found along the doping line nearer the reactor, as well as buildup inside the pneumatic valves controlling the gas transport. Over time, this buildup could lead to drastically different doping profiles, and subsequently, much different PL emission.

It is also speculated that over a duration of time, a contamination of the Er precursor occurs due to the formation of Fe adducts inside the precursor bubbler. Fig. 3-35 contains a SIMS analysis of Er-doped GaN grown at different times of the Er bubbler lifetime. Sample 2386 and 2513 are grown under the same conditions and have the same epilayer structure. The SIMS data shows that the Er concentrations for the samples are identical, yet the Fe concentration in sample 2513 is nearly 15 times higher. XRD diffraction data and the surface morphology for each sample are identical as well (not pictured). Fig. 3-36 is the PL spectra of samples 2386 and 2513 at 300 K for λ_{exc} = 263 nm. The PL intensity for 2386 is ~ 15 times larger than 2513. Thus, since all accountable aspects of the two samples remains identical except the Fe concentration, it is tentatively concluded that increased Fe concentration results in a decrease in PL intensity. The mechanism for this decrease in PL intensity is not yet understood.

It is believed that the larger Fe incorporation occurs over time inside the Er bubbler due to the high storage temperatures. At the elevated temperatures, the thermal energy is sufficient to allow the Fe from the stainless steel wall to exchange with the Er in the metalorganic precursor and produce small amounts of Fe MO precursor. Ordering smaller amounts of Er precursor and growing over a short time have been attempted in hopes of limiting the Fe contamination thus increasing the doping and PL repeatability. But, to date, this has not resulted in a time effective solution. It is highly recommended that a bubbler and transport system be coated with a material that is both inert to the Er precursor and has the ability to handle temperatures between 100 – 140 C. This may completely eliminate the formation of Fe inside the bubbler while still allowing for a high vapor pressure.

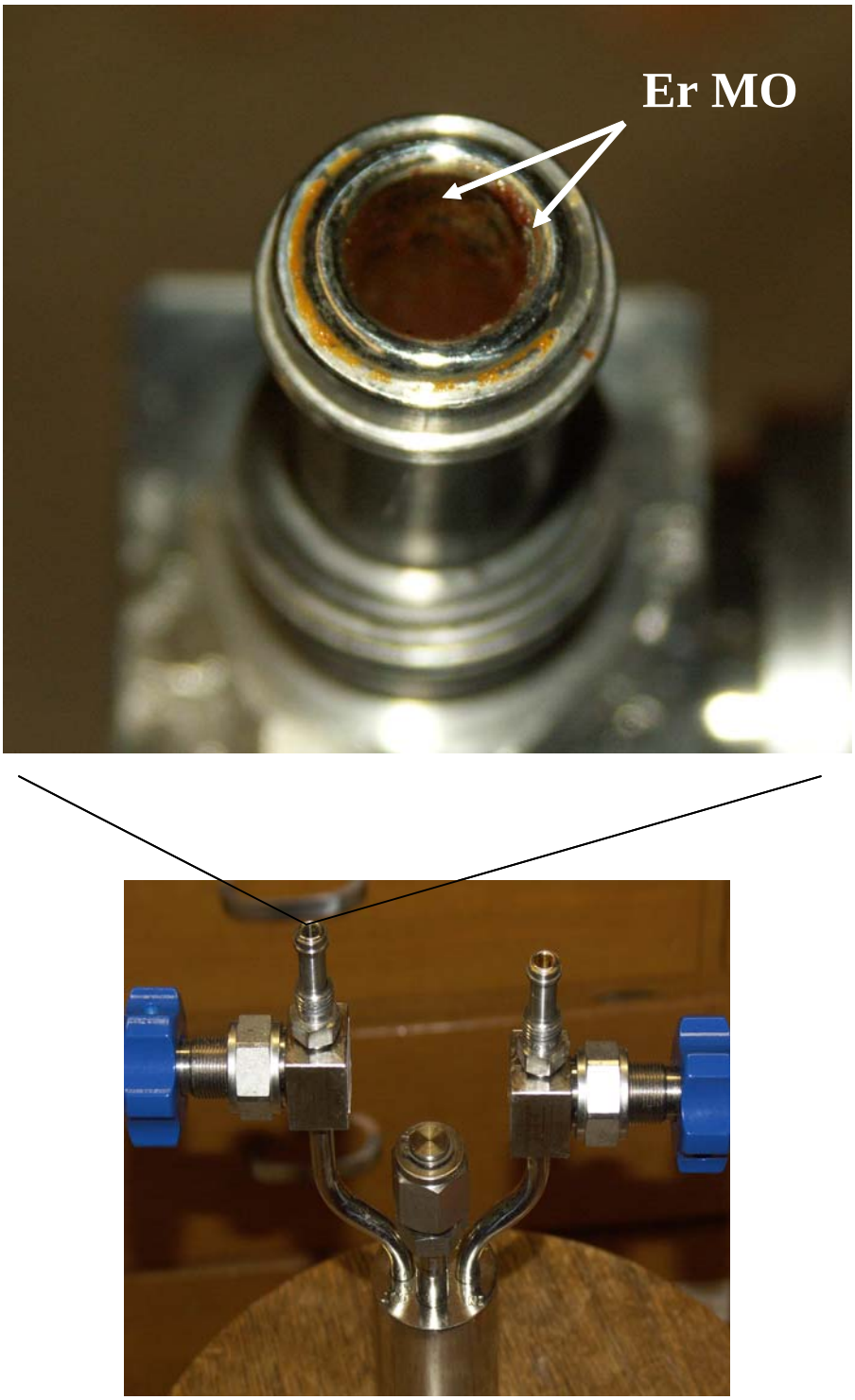

Figure 3-34 Close up of output valve showing the condensation of Er precursor

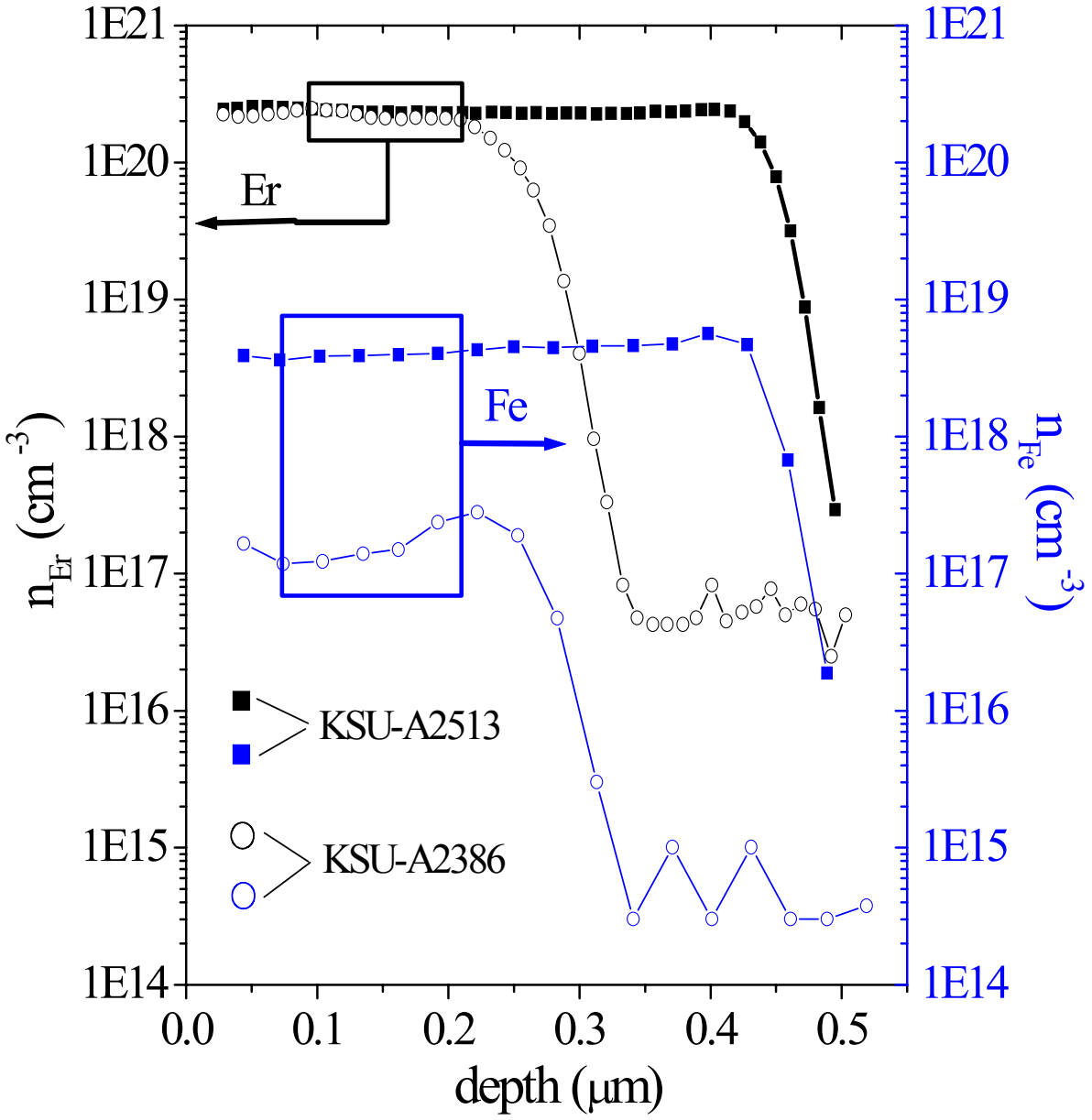

Figure 3-35 SIMS analysis of Er-doped GaN epilayers KSU-A2513 and KSU-A2386. The samples have identical structure and are grown in the same growth conditions. The samples are grown one year apart.

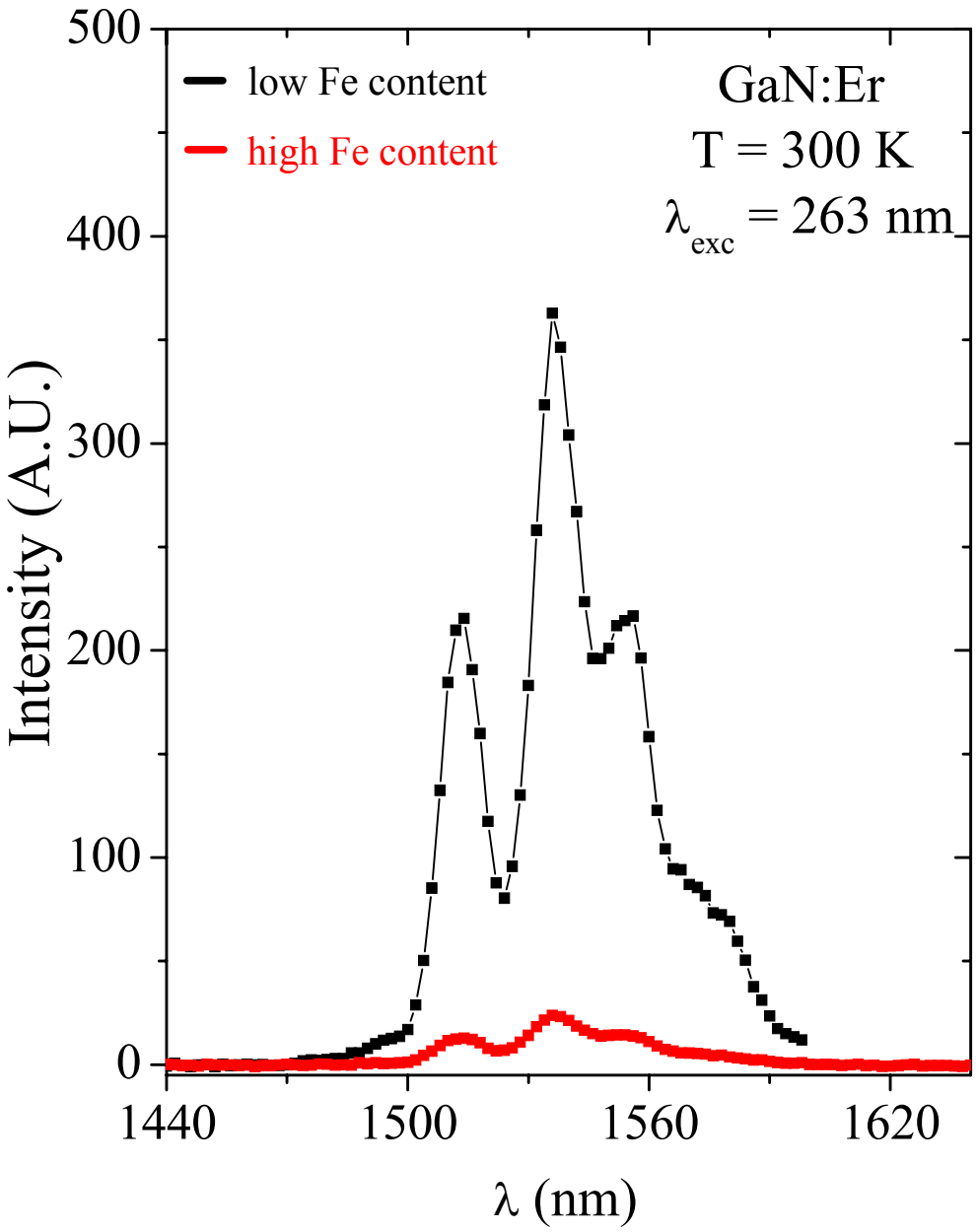

Figure 3-36 PL spectra of Er-doped GaN epilayers KSU-A2513 and KSU-A2386 measured at 300 K for λ_{exc} = 263 nm.

3.4.2 More modifications to the MOCVD process

It was also determined in the case of Er-doped GaN (besides the doping inconsistencies), that the interaction of the Er precursor with NH_3 is a very important process for both Er PL emission and surface morphology. Currently, our MOCVD uses an NH_3 jet to separate the gaseous interaction of NH_3 and the MO precursor before the reaction zone. But, as obvious from the OM microscope images in section 3.1.2, the interaction of NH_3 with the Er precursor leads to surfaces with large diameter surface clusters. It was also shown that drastically reducing the NH_3 flux leads to much improved surface morphologies. Thus, it is further hypothesized that implementing more elaborate methods of reducing the interaction of NH_3 and Er precursor may help to improve the surface further.

In the case of Er-doped InGaN (besides the doping inconsistencies), the decrease in PL intensity is attributed to both the high formation energy of the Er emitting centers and to another mechanism not fully understood as outlined in the work above. It is the researchers opinion, that the need for growth of high Er concentrations at low pressures (< 20 torrs) severely limits the growth temperature. If higher growth pressures were possible, the In fraction could be scaled so as to allow for a higher growth temperature. Thus, it is highly recommended that the MFC be placed downstream of the bubbler and be outfitted for high temp growth. Then, it would be possible to achieve higher growth temperatures with reasonable In fractions, and thus attempt to determine the other mechanism for the lower PL intensity in Er-doped InGaN than in Er-doped GaN.

CHAPTER 4 - General Conclusions

Er-doped GaN/InGaN materials and devices were synthesized by metal organic chemical vapor deposition (MOCVD) for the first time. The optical and structural properties of these materials were investigated using a custom UV photoluminescence (PL) spectroscopy system, a custom UV electroluminescence (EL) spectroscopy system, atomic force microscopy (AFM), X-ray diffraction (XRD), secondary ion mass spectroscopy (SIMS), and optical microscopy (OM).

Er-doped GaN via MOCVD emits a strong PL emission at 1.54 μm. In contrast to other growth methods, MOCVD grown Er-doped GaN epilayers exhibit virtually no visible emission lines. A small thermal quenching effect, with only a 20% decrease in the integrated intensity of the 1.54 μm PL emission, occurred between 10 and 300 K. The dominant bandedge emission of Er-doped GaN at 3.23 eV was observed at room temperature, which is red-shifted by 0.19 eV from the bandedge emission of undoped GaN. An activation energy of 191 meV was obtained from the thermal quenching of the integrated intensity of the 1.54 μm emission line. This energy was assigned to the Er_{Ga}–V_N complex, where Er_{Ga} represents the Er on Ga sublattice and V_N represents the nitrogen vacancy. It was determined that this complex represents the dominant class of Er emitting centers in Er-doped GaN via MOCVD.

It was observed that surface morphology and 1.54 μm PL emission intensity was strongly dependent upon the Er/NH_3 flux ratio and the growth temperature (T_G). XRD measurements showed that the crystalline ordering of the (002) plane was relatively unperturbed for the changing growth environment. Least squared fitting of 1.54 μm PL measurements from Er-doped GaN of different T_G was utilized to determine a formation energy of 1.82 ± 0.1 eV for the Er emitting centers. Higher T_G resulted in a more degraded surface morphology due to the increase strain caused by the larger concentration of Er emitting centers. For certain fluxes of NH_3 and Er precursor, surface cluster formation occurred. For larger NH_3 fluxes, an increase of cluster density was observed, whereas an increase in Er flux increased the cluster diameter.

The crystalline quality and surface morphology of Er-doped $In_{0.05}Ga_{0.95}N$ was nearly identical to that of Er-doped GaN, yet the PL intensity of the 1.54 μm emission from Er-doped $In_{0.05}Ga_{0.95}N$ was 16 x smaller than that of Er-doped GaN. The drop in PL intensity is attributed

to the much lower growth temperature in conjunction with the high formation energy of the Er emitting centers. Er-doped InGaN grown at fixed growth temperature with different growth pressures, NH3 fluxes, and Ga fluxes was also investigated, and showed that increased In fractions also resulted in a smaller 1.54 μm PL intensity.

Er-doped InGaN p-i-n diodes were synthesized and tested. The EL spectra under forward bias shows strong Er based emission for the infrared and visible region. The diodes also exhibit no bandedge emission, which implies the mechanism of Er excitation to be that of impact excitation. I-V curves for the Er based diodes were much higher than their LED counterparts, implying a severe degradation in the p-layer conductivity due to surface roughening. Si codoping of the i-layer resulted in a more reasonable I-V dependency, but only at the expense of the Er based emission power.

Several obstacles remain for the consistency of Er doping by MOCVD. First, a more elaborate heating system must be applied to the doping line to prevent precursor condensation. Second, the possible contamination of Fe with the Er precursor as a function of bubbler temperature and time must be solved. Thirdly, a more elaborate method of eliminating the exposure time of the NH_3 and Er precursor must be implemented in order to optimize the surface morphology to device grade. Lastly, higher growth pressures must be obtained in order to produce InGaN with a reasonable In fraction and Er based PL emission intensity.

References

[1] M. Riordan and L. Hoddeson, "The origins of the pn junction", IEEE Spectrum, June 1997, pp. 46-51.

[2] S. M. Sze, Kwok K. NG, *Physics of Semiconductor Devices*, John Wiley and Sons, Inc.; New Jersey; (2007)

[3] S. Nakamura, IEEE, Circuits and Devices, May, 19 (1995).

[4] T. Matsuoka, H. Okamoto, M. Nakao, H. Hiama, and E. Kurimoto, Appl. Phys. Lett. **81**, 1246 (2002).

[5] J. Edgar, *Properties of Group-III-Nitrides,* Institution of Electrical Engineers, (1994)

[6] see LED products from CREE inc., www.cree.com

[7] see LED products from Phillips LumiLEDs, www.philipslumileds.com

[8] W. C. Johnson, J. Parsons, and M. C. Crew, J. Phys. Chem. **36**, 2561 (1932).

[9] R. Juza and H. Hahn, Z. Anorg. Allgem. Chem. **234**, 282 (1938).

[10] R. Juza and H. Hahn, Z. Anorg. Allgem. Chem. **244**, 133 (1940).

[11] H. P. Maruska and J. J. Tietjen, Appl. Phys. Lett. **15**, 327 (1969).

[12] M. Ilegems and R. Dingle, J. Appl. Phys. **44**, 4234 (1973).

[13] J. I. Pankove, M. T. Duffy, E. A. Miller, and Berkeyhelser, J. Lumin. **8**, 89 (1973).

[14] O. Lagerstedt and B. Monemar, J. Appl. Phys. **45**, 2266 (1974).

[15] B. Monemar, O. Lagerstedt, and H. P. Gislason, J. Appl. Phys. **51**, 625 (1980).

[16] J. I. Pankove and J. A. Hutchby, J. Appl. Phys. **47**, 5387 (1976).

[17] J. I. Pankove, E. A. Miller, and J. E. Berkeyheiser, J. Lumin. **5**, 84 (1972).

[18] H. Amano, I. Akasaki, K. Hiramatsu, and N. Koide, Thin Solid Films **163**, 415 (1988).

[19] I. Akasaki, H. Amano, Y. Koide, K. Hiramatsu, and N. Sawaki, J. Cryst. Growth **98**, 209 (1989).

[20] S. Nakamura, Jpn. J. Appl. Phys., Part 2 **30**, L1705 (1991).

[21] S. Nakamura, M. Senoh, and T. Mukai, Jpn. J. Appl. Phys., Part 2 **30**, L1708 (1991).

[22] H. Amano, M. Kito, K. Hiramatsu, and I. Akasaki, Jpn. J. Appl. Phys., Part 2 **28**, L2112 (1989)

[23] S. Nakamura, T. Mukai, M. Senoh, and N. Iwasa, Jpn. J. Appl. Phys., Part 2 **31**, L139 (1992).

[24] S. Nakamura, T. Mukai, M. Senoh, and N. Iwasa, Appl. Phys. Lett. **64**, 1687 (1994).

[25] J. M. Zavada and Dahua Zhang, Solid-State Electronics 38, 1285 (1995).

[26] C.K. Jorgensen, *J.Inorg.Nuclear Chem*.,**1**,301 (1955).

[27] Wybourne, *Spectroscopic Properties of Rare Earths*, Interscience Publishers; New York, (1965).

[28] S. Hufner, *Optical Spectra of Transparent Rare Earth Compounds*, Academic Press; New York, (1978).

[29] R. Reisfeld, C. K. Jorgensen, *Lasers and Excited States of Rare-Earths*, Springer-Verlag Berlin ; New York ; (1977)

[30] see EDFA products from OEQuest, http://www.oequest.com/

[31] After http://www.fiber-optics.info/articles/op-amp.htm

[32] http://www.em4inc.com/product_semiconductor_optical_amplifiers.htm

[33] G. Blasse and B. C. Grabmaier, Luminescent Materials, Springer; Berlin (1994).

[34] R. Birkhahn et al., J. Vac. Sci. Technol. 1999, B 17 (3), p. 1195

[35] P. N. Favennec, H. L'Haridon, M. Salvi, D. Moutonnet, and Y. LeGuillou, Electron. Lett. **25**, 718 (1989).

[36] M. R. Brown, A. F. J. Cox, W. A. Shand, and J. M. Williams; Advances in Quantum Electronics **2**, 69, (1974).

[37] H. Ennen, J. Schneider, G. Pomrenke, and A. Axmann ,Appl. Phys. Lett. **43**, 943 (1983).

[38] P. S. Whitney, K. Uwai, H. Nakagome, and K. Takahei, Electron. Lett. **24**, 740 (1988)

[39] A. Rolland, A. Le Corre, P. N. Favennec, M. Gaunneau, B. Lambert, D. Lecrosnier, H. L'Haridon, D. Moutonnet, and C. Rochaix, Electron. Lett. **24**, 956 (1988)

[40] P. Galtier, J. P. Pocholle, M. N. Charasse, B. De Cremoux, J. P. Hirtz, B. Groussin, T. Benyattou, and G. Guillot, Appl.Phys. Lett. **55**, 2105 (1989)

[41] H. Isshiki, H. Kobayashi, S. Yugo, T. Kimura, and T. Ikoma, Appl. Phys. Lett. **58**, 484 (1991)

[42] S. J. Chang and K. Takahei, Appl.Phys. Lett. **65**, 433 (1994)

[43] X. Z. Wang and B. W. Wessels, Appl. Phys. Lett. **65**, 584 (1994)

[44] G. M. Ford and B. W. Wessels, Appl. Phys. Lett. **68**, 1126 (1996)

[45] A. Koizumi, Y. Fujiwara, A. Urakami, K. Inoue, T. Yoshikane, and Y. Takeda, Appl.Phys. Lett. **83**, 4521 (2003)

[46] R. G. Wilson, R. N. Schwartz, C. R. Abernathy, S. J. Pearton, N. Newman, M. Rubin, T. Fu, and J. M. Zavada, Appl. Phys. Lett. **65**, 992 (1994).

[47] J. T. Torvik, R. J. Feuerstein, J. I. Pankove, C. H. Qiu, and F. Namavar, Appl. Phys.Lett. **69**, 2098 (1996).

[48] S. Kim, S. J. Rhee, D. A. Turnbull, E. E. Reuter, X. Li, J. J. Coleman, and S. G. Bishop, Appl. Phys. Lett. **71**, 231 (1997).

[49] D. M. Hansen,R. Zhang, N. R. Perkins, S. Safvi, L. Zhang, K. L. Bray, and T. F. Kuech, Appl. Phys. Lett. **72**, 1244 (1998).

[50] J. D. MacKenzie, C. R. Abernathy, S. J. Pearton, U. Hömmerich, J. T. Seo, R. G. Wilson, and J. M. Zavada, Appl. Phys. Lett. **72**, 2710 (1998).

[51] A. J. Steckl , M. Garter, R. Birkhahn and J. Scofield, Appl. Phys. Lett. **73**, 2450 (1998).

[52] M. Garter, J. Scofield, R. Birkhahn, and A. J. Steckl, Appl. Phys. Lett. **74**, 182 (1999).

[53] R. H. Birkhahn, R. Hudgins, D. S. Lee, B.K. Lee and A. J. Steckl, A. Saleh, R. G. Wilson, J. M. Zavada, MRS Internet J. Nitride Semicond. Res. 4S1, G3.80 (1999).

[54] A. J. Steckl , J. Heikenfeld, M. Garter, R. Birkhahn, and D. S. Lee, Compound Semiconductor, 6(1), January/February, 2000.

[55] J. M. Zavada, S. X. Jin, N. Nepal, H. X. Jiang, J. Y. Lin, P. Chow, and B. Hertog, Appl. Phys. Lett. **84,** 1061 (2004).

[56] C. S. Son, S. Kim, Y. H. Kim, I. K. Han and Y. T. Kim, A. Wakahara, I. H. Choi, H. C. Lopez, Journal of the Korean Physical Society **45**, 955 (2004).

[57] X. Wu, U. Hommerich, J.D. MacKenzie, C.R. Abernathy, S.J. Pearton, R. Schwartz, R.G. Wilson, and J.M. Zavada, Appl. Phys. Lett. **70**, 2126 (1997).

[58] C. Ugolini, N. Nepal, J. Y. Lin, H. X. Jiang, and J. M. Zavada, Appl. Phys. Lett. **89**, 151903 (2006).

[59] Shuji Nakamura, Gerhard Fasol, *The blue laser diode : GaN based light emitters and lasers,* Springer; Berlin; New York (1997)

[60] see companies like Crystal IS or KYMA, www.crystal-is.com or www.kymatech.com

[61] G. B. Stringfellow, Organometallic Vapor-Phase Epitaxy: Theory and Practice (Academic Press, Inc., San Diego, 1989).

[62] data taken from MSDS for TMGa, TMAl, and Cp_2Mg provided by *SAFC hitech*

[63] Yu.B. Zverev, S.G. Chesnokova, Vysokochistye veschestva (High-purity materials),**Volume 1**, 1996, p.75-78

[64] P. F. Fewster, X-ray Scattering from Semiconductors, 2nd ed. (Imperial Colleg Press, London, 2003).

[65] http://www.ioffe.ru/SVA/NSM/Semicond/index.html

[66] M. Smith, G. D. Chen, J. Y. Lin, H. X. Jiang, A. Salvador, B. N. Sverdlov, A. Botchkarev, and H. Morkoc, Appl. Phys. Lett. **66**, 25 (1995).

[67] K. Makarova, M. Stachowicz, V. Glukhanyuk, A. Kozanecki, C. Ugolini, J.Y. Lin, H.X. Jiang, J. Zavada, Materials Science and Engineering B **146** (2008) 193–195.

[68] J. S. Fihol, R. Jones, M. J. Shaw, P. R. Briddon, Appl. Phys. Lett. **84**, 2841 (2004).

[69] S. F. Song, W. D. Chen, C. Zhang, L. Bian, C. C. Hsu, L. W. Lu, Y. H. Zhang, and J. Zhu, Appl. Phys. Lett. **86**, 152111 (2005).

[70] M. Smith, G. D. Chen, J. Y. Lin, H. X. Jiang, A. Salvador, B. N. Sverdlov, A. Botchkarev, H. Morkoc, and B. Goldenberg, Appl. Phys. Lett. **68**, 14 (1996).

[71] B. A. Andreev, Z. F. Krasilnik, D. I. Kryzhkov, V. P. Kuznetsov, T. Gregorkiewicz, W. Jantsch, Appl. Phys. Lett. **88**, 201101 (2006).

[72] S. C. Jain, M. Willander, J. Narayan, R. Van Overstraeten, J. Appl. Phys. **87**, 965 (2000).

[73] C. Ugolini, N. Nepal, J. Y. Lin, H. X. Jiang, and J. M. Zavada, Appl. Phys. Lett. **90**, 051110 (2007).

[74] C. A. Larsen, N. J. Buchanan, S.H. Li and G.B. Stringfellow, Journal of Crystal Growth **102**, 103 (1990).

[75] A. Thon and T. F. Kuech, Appl. Phys. Lett. **69**, 55 (1996).

[76] Amnon Yariv, *Optical Electronics,* CBS College Publishing; New York, pg. 130 (1985)

[77] Y. H. Xie, E. A. Fitzgerald, and Y. J. Mii, J. Appl. Phys. **70**, 3223 (1991).

Appendix A- Publications

1. "Current-injected 1.54 μm light emitting diodes based on erbium-doped GaN", R. Dahal, **C. Ugolini**, J. Y. Lin, H. X. Jiang,, and J. M. Zavada, Appl. Phys. Lett. **93**, 033502 (2008).
2. "Spectroscopic study of Er-centers in MOCVD grown GaN layers highly doped with Er", K. Makarova, M. Stachowicz, V. Glukhanyuk, A. Kozanecki, **C. Ugolini**, J.Y. Lin, H.X. Jiang, J. Zavada, Materials Science and Engineering B **146**, 193–195 (2008).
3. "Optical and magnetic behavior of erbium-doped GaN epilayers grown by metal-organic chemical vapor deposition", J. M. Zavada, N. Nepal, **C. Ugolini**, J. Y. Lin, H. X. Jiang, R. Davies, J. Hite, C. R. Abernathy, S. J. Pearton, E. E. Brown and U. Hömmerich, Appl. Phys. Lett. **91**, 054106 (2007).
4. "Er-doped GaN epilayers synthesized by metal organic chemical vapor deposition" , **C. Ugolini**, N. Nepal, J. Y. Lin, H. X. Jiang, J. M.. Zavada, in Advances inI-V Nitride Semiconductor Materials and Devices, edited by C.R. Abernathy, H. Jiang, J.M. Zavada (Mater. Res. Soc. Symp. Proc. 955E, Warrendale, PA, 2007), 0955-I10-05
5. "Excitation dynamics of the 1.54 μm emission in Er-doped GaN synthesized by metal organic chemical vapor deposition", **C. Ugolini**, N. Nepal, J. Y. Lin, H. X. Jiang, and J. M. Zavada, Appl. Phys. Lett. **90**, 051110 (2007).
6. "Correlation between optical and electrical properties of Mg-doped AlN epilayers", M. L. Nakarmi, N. Nepal, **C. Ugolini**, T. M. Altahtamouni, J. Y. Lin, and H. X. Jiang, Appl. Phys. Lett. **89**, 152120 (2006).
7. "Erbium-doped GaN epilayers synthesized by metal-organic chemical vapor deposition", **C. Ugolini**, N. Nepal, J. Y. Lin, H. X. Jiang, and J. M. Zavada, Appl. Phys. Lett. **89**, 151903 (2006).